2015

Novel applications in nonlinear crystals based on second-order nonlinear optical interactions

Da Li
Lehigh University

Novel applications in nonlinear crystals based on second-order nonlinear optical interactions

by

Da Li

Presented to the Graduate and Research Committee

of Lehigh University

in Candidacy for the Degree of

Doctor of Philosophy

in

Electrical Engineering

Lehigh University

May 2015

Approved and recommended for acceptance as a dissertation in partial fulfillment of the requirements for the degree of Doctor of Philosophy

_____

Date

_____

Yujie J. Ding
(Dissertation Advisor)

_____

Accepted Date

Committee Members:

_____

Yujie J. Ding
(Committee Chair)

_____

Filbert. J. Bartoli

_____

Nelson Tansu

_____

Sushil Kumar

_____

Dimitrios Vavylonis
(Physics Department)

Acknowledgements

"I know that I know nothing."

-Socrates

It was what I said to myself when I stepped into Rm. 225 of Packard Lab on my first day arriving at Lehigh University to start pursuit of a Ph.D. degree in Electrical and Computer Engineering; and it is what I say to myself now when I am sitting in front of my laptop drafting my Ph.D. dissertation six years later. Undoubtedly, knowledge and skills obtained during the years have been proven useful. Nevertheless, I believe the true meaning of a Ph.D. degree lies in the multiple capabilities she has granted me: for example, the capability of approaching a problem, the capability of collaborating with co-workers, and the capability of overcoming a challenge. She equipped me with a strong mind and made me not fearful of anything on my life path hereafter.

It was not easy going through the years. There are so many great people I would like to acknowledge, without whom I would never be able to complete my degree. I am doing my best to address them in the following paragraphs.

First and foremost, I owe a tremendous debt to Prof. Yujie J. Ding, who is my research advisor and guided me through all my research during the years. Prof. Ding has extremely solid knowledge in the field of laser physics and nonlinear optics. I always benefit from our discussion, for he is a fast thinker and always has plethora of novel ideas. He granted me ample freedom during the research, and whenever unexpected results

came up, he and I would work together to figure out the reasons. He is not only my advisor in scientific research, but also my advisor in my life.

I would also like to thank Prof. Sushil Kumar, Prof. Filbert J. bartoli, Prof. Nelson Tansu, and Prof. Dimitrios Vavylonis, for their precious time being my committee members and reading my dissertation. Their support is definitely indispensible in the completion of my Ph.D. degree. Prof. Kumar and Prof. Bartoli were so helpful and responsive for the administrative issues I would need to process upon the receipt of a job offer; Prof. Tansu gave excellent courses in Applied Quantum Physics, which in the early years I had the honor to attend and benefited a lot in his lecture; Also, Prof. Bartoli and Prof. Tansu have been on my research committee from qualification exam (1^{st} year), general exam (4^{th} year), to dissertation defense now. Prof. Vavylonis has been on my research committee from general exam as well. I am so grateful to every piece of advice they suggested, which always improves my dissertation and benefits my research.

Dr. Yi Jiang and Dr. Guibao Xu were the two post doctoral fellows as I joined Dr. Ding's research group and they were both helpful in introducing the field and developing experimental skills. Dr. Yi Jiang taught me most of the experimental tricks I needed to know in the single photon detection project, such as fiber to waveguide coupling and crystal oven fabrication. Yi and Guibao were always available for inspiring discussions.

As visiting scholars from Shandong University, China, Dr. Lei Wang and Dr. Zhaojun Liu have been astoundingly handy and knowledgeable in optical waveguide and solid state laser setups. They instructed me on these areas during their visit and the knowledge

they passed down to me has been proved to be essential either in my Ph.D. research work or in the projects I have been working on in the company now.

Post doctoral researchers Dr. Srinivasa Ragam and Dr. Xinquan Zou worked on optical benches adjacent to mine. Whenever I got a chance I would sneak into their territory and ask them to explain their experiment. They were always patient to me and never had one time had me kept away from their bench. Srini's expertise in terahertz generation through IR DFG and Xinquan's expertise in image correction through phase-conjugation broadened my field of research and widened my horizon.

I would also like to offer my sincere thanks to Dr. Pu Zhao, Dr. Guan Sun, Roulin Chen, Xiaomu Lin, Ran Wang, and Pengda Hong, who were or still are Ph.D. student like I am now. Pu and Guan possess extensive knowledge base in solid state lasers, nonlinear optics, and semiconductors. Our conversation has always been enlightening and joyful. As senior students, they offered me various help, both technical and nontechnical. I really appreciate it.

I would like to thank the administrative team of the ECE department. Diane Hubinsky and Ruby Scott are always there ready to handle any of the administrative questions I threw at them, kindly and patiently. Also, I appreciate help from Hermann Baader and Eli Towne, the mechanist buddies in the machine shop. They helped fabricate PPLN crystal ovens and laser crystal clamps.

To my family, I would say the word "acknowledgement" is definitely too light to express my gratitude. To mom and dad, who have supported me since I was born, I wish

you would be proud of me upon conferral of the Ph.D. degree (and I am sure you will). And to Cihang Xu, my beloved fiancée, for all these years you have been sharing joys and sorrows with me. Your encouragement when I was down, and your heartful smile when I reached a milestone, are the most beautiful words and image that I would never ever forget. We have been going through so many things together and I guess nothing can make us apart. You are the only girl who I love with the rest of my life.

To all, I thank you again for everything you have offered me. You are the most precious wealth in my life and I *love you all*.

Da Li

1:15 AM, PST

03/06/2015

Table of Contents

List of Tables

List of Figures

Abstract

Second order nonlinear mediums, like lithium niobate and KTP, have been extensively studied for various applications, such as single photon detection and terahertz generation. In this dissertation, several novel applications in second order nonlinear crystals have been studied in depth, as follows:

1) Highly efficient single-photon level detection at 1.57μm. There exists an absorption peak for carbon dioxide at 1.57 μm, which is extremely desirable for NASA ASCENDS program, due to the fact that it can monitor CO_2 concentration in the outer space. Commercially available detectors at IR wavelengths suffer from high dark counts up to 10^5/s, as well as low quantum detection efficiencies, usually with values between 10% and 15%. In contrast, single-photon counting in near-IR (600-800nm) can be performed efficiently with silicon APDs. Single photon counting modules with dark counts lower than 25/s and detection efficiency in the range 50% to 70% are commercially available. We took advantage of silicon APDs, implemented efficient conversion from 1.57μm to visible with more than 60% of internal quantum conversion efficiency and demonstrated almost noise-free measurement. As a result, our detection system has reached an ultralow noise level of 25 s^{-1} and a detectable photon rate of 81 s^{-1} for communication band.

2) Non-destructive method for evaluating domain errors in PPLN waveguide using surface-emitting geometry (SHG). Periodically-poled lithium niobate (PPLN) waveguide is an efficient nonlinear structure for generation of tunable coherent radiation based on optical parametric oscillators and single-photon detection based on frequency up-conversion. In order to achieve efficient conversion, quasi-phase-matching (QPM) must be satisfied. However, imperfections of periodic domains due to fabrication errors such as linear taper of domain period, duty cycle error, and randomness of domain period significantly affect the performance of the PPLN waveguide. We developed a fast and non-destructive method to statistically evaluate the domain quality of PPLN. The resolution can reach 0.5nm.

3) Anti-Stokes enhancement observation in lithium niobate waveguide. Anti-Stokes signals are much weaker than Stokes counterparts due to significantly reduced phonon occupation numbers. We now measure the forward- and backward- propagating anti-stokes photons from waveguide and observed enhancement factor at least one order of magnitude higher than in the bulk. The required pump power was reduced five orders of magnitude to only a few microwatts. Under two propagation configuration, we observed different layouts of anti-stokes peaks for lithium niobate.

4) Terahertz generation through difference frequency generation of two close wavelength IR beam in Gallium Phosphide (GaP) stacks. By stacking alternatively rotated GaP plates, we reached maximum terahertz photon conversion efficiency of 40%. The corresponding peak power generated inside the four GaP plates approaches 4kW. As the number of plates is increased from four to five, the THz output power is significantly decreased, due to back parametric conversion.

Chapter 1

Introduction

1.1 Introduction of wave interactions in second-order nonlinear mediums

Looking back at the observation of second-harmonic generation by Franken and coworkers [1] in 1961, the field of nonlinear optics is now more than fifty years old. Nonlinear optics is the study of the phenomena that happen as a consequence of the modification of optical properties of a material at the presence of intense light [2]. The response of the material is nonlinear to the applied optical field in a nonlinear optical process. Examples and their potential applications of nonlinear interactions are:

1) Second-harmonic generation

Fig. 1.1 Geometry of second-harmonic generation

A optical beam with fundamental frequency ω illustrate on a material with sufficiently large second-order nonlinear susceptibility $\chi^{(2)}$, or second-order nonlinear coefficient $d^{(2)}$. At the output

facet of the material, beam with doubled frequency 2ω can be observed. The conversion efficiency could reach up to 100% under optimum condition. Almost all commercialized green lasers at wavelength of 532 nm are built via second-harmonic generation of 1064nm emission from Nd:YAG laser crystals.

2) Sum- and Difference- Frequency Generation

Fig. 1.2 Geometry of Sum-frequency generation (SFG)

Fig. 1.3 Geometry of Difference-frequency generation (DFG)

If we have two optical beams with distinct frequency components incident on the same material, sum- and difference frequency generation can occur at the same time (assuming $\omega_1 > \omega_2$), being competitive processes depending on phase-matching conditions

favor. The generation of a new frequency is governed by the coupled-mode equations, which will be introduced in the following chapters. Sum- and Difference- generations are effective and flexible method to build optical sources with various laser-like outputs, whose wavelength is not at the emission lines of any existing laser gain mediums. These techniques are the main focus of this dissertation, as most of our work is based on SFG or DFG.

1.2 Overview of the dissertation

The dissertation is organized as follows.

Chapter 2 demonstrates a single photon detection system based on sum-frequency generation in periodically poled lithium niobate waveguide. We employ plane wave approximation with incorporated waveguide transverse mode profile to describe the three-wave interaction in the nonlinear waveguide for pump beam at 980nm, signal beam at communication band, around 1550nm, and the sum-frequency generation at ~600nm. In order to achieve efficient frequency conversion, a periodically poled structure is employed here to enable the utility of the largest nonlinear coefficient d_{33} of lithium niobate. We then give an overview of the relevant achievements obtained in the field. Upon illustrating our experimental setup, we show corresponding experimental results that support the achievement of single photon detection of communication band photons. As the noise photons generated in the frequency conversion process are the main factor that limits the sensitivity of the single photon detector, we analyze parametric noise generation on perfect and imperfect lithium niobate gratings and deduce that the noise generation from our waveguide is almost negligible and therefore, we can achieve single photon detection of extremely high sensitivity. Before ending this chapter, we also propose a novel method for potentially achieving single photon detection in GaP-based devices with internal total reflection. A sub-conclusion is presented at the end of this chapter.

Since we mention waveguide imperfection in the previous chapter, we study a non-destructive method to evaluate the periodically poled domain errors in Chapter 3. We

utilize two identical beams counter-propagating in a periodically poled lithium niobate waveguide and analyze the far-field surface-emitting second harmonic generation. Any domain errors deviating from perfect grating structure configuration will be reflected on changes of the far-field patterns. By simulation, we are able to fit some of the imperfection parameters to our waveguide and obtain domain period information in a statistical means.

Also in lithium niobate waveguide, we study anti-Stokes photon enhancement in Chapter 4. By detecting the forward- and backward- propagating anti-Stokes photons from the waveguide, we observe different peaks and identify obvious enhancement than from the bulk, which is also measured. We are able to reduce the pump power to several micro watts and that is five orders of magnitude lower than previous record. Therefore, it is feasible for us to eventually develop a compact and portable Raman probe.

In Chapter 5, we switch our focus from lithium niobate waveguide to GaP stacks, where two close-wavelength infrared beams combine and generate terahertz beam via difference frequency generation (DFG). By alternatively stacking GaP plates, the DFG process meets quasi-phase-matching condition and the terahertz output increases quadratically with the total length of the stack. As we increase the number of GaP stack from four to five, we even observe back parametric conversion, i.e. terahertz beam and one of the infrared beam with lower frequency begins to implement sum-frequency process and convert back to the other IR beam. An overall quantum conversion frequency of 40% has been achieved, with terahertz peak power obtained as high as 4kW.

Chapter 6 concludes the work and contribution mentioned in previous chapters and suggests future works.

Chapter 2

Single photon counting based on frequency upconversion in PPLN waveguide

2.1 Historical Overview

Single-photon detectors [3] play important roles in fiber-based telecommunications, quantum information and computing [4,5], data encryption, imaging [6,7], light detection and ranging, sensing, DNA sequencing, astrophysics, and materials science. For example, the wavelengths in the proximity of 1.55 μm can be used to remotely measure trace levels of CO_2 in the atmosphere, which is considered as an indicator to monitor primary changes in terrestrial ecosystems that are connected with large-scale weather and climate modes. This is extremely important to NASA, especially ASCENDS mission [8].

A perfect single-photon detector is expected to have a detection efficiency of 100%, i.e. the probability for a photon to be successfully detected every time when it hits the detector reaches 100%. In addition, it must have a zero dark count rate. Moreover, it must have a zero reset or dead time. Finally, it must have a zero timing jitter, i.e. zero uncertainty in specifying the instance when a photon arrives. However, for the single-

photon detectors being investigated so far, their performance significantly deviate from the ideal specifications given above. This is especially true at room temperature, which is required to realize certain applications. Therefore, detections of photons at the single-photon levels remain to be challenging. Perhaps, one of the low-cost single-photon detectors is based on a Si-based avalanche photodiode (APD) being operated at room temperature. The detection efficiency, dark count rate, timing jitter, and dead time of the APDs are capable of reaching 70%, 25 s^{-1}, ps, and 32 ns at room temperature, respectively. However, the detection wavelength range for these detectors is limited to 400-1060 nm with the detection efficiency peaking at 600 nm.

In the communication band around 1550 nm, however, InGaAs/InP APDs, commercially available, suffer from large dark count rates (i.e. 10^4-10^5 s^{-1}) and low detection efficiencies ($\leq$ 10%). In this wavelength range, the best single-photon detectors are perhaps made from superconducting nanowires. Indeed, it was demonstrated that such detectors were capable of reaching the detection efficiency of 93% and dark count rate of < 10 s^{-1} at the temperatures up to 2 K [9]. By incorporating a bandpass filter consisting of SiO_2/Si bilayers being deposited onto the backside of a thermally oxidized Si substrate, the lowest noise equivalent power was determined to be 2.0×10^{-19} $W/Hz^{1/2}$ [10]. Although these detectors perform extraordinarily, the operating temperatures of up to 2 K may limit their applications.

Besides the detectors based on the superconducting nanowires, frequency upconversion in a nonlinear medium is a viable approach for single-photon detections

[11-13]. This approach builds upon the great performance of the Si-based single-photon detector at the wavelengths of around 600 nm, stated above. By mixing the pump beam at the wavelength of 980 nm from a diode laser with the input signal at 1550 nm in a nonlinear medium, for instance, the output radiation at the wavelength of 600 nm is converted from 1550 nm to 600 nm based on frequency upconversion (i.e. sum-frequency generation) in a nonlinear medium. By measuring the output at 600 nm via a Si-based single-photon detector, one can determine the input signal at 1550 nm, approaching the single-photon levels [14-16]. Besides the classical regime for the upconversion, non-classical intensity correlations between the up-converted photons and pump photons were demonstrated in a quantum frequency-conversion experiment [17].

When a pump beam at the wavelength of 980 nm was used, it can generate the photons at the wavelengths of around 1.55 μm and 2.66 μm through spontaneous parametric down-conversion (SPDC) process in a nonlinear medium. The photons generated around 1.55 μm by SPDC can be up-converted to the photons at 600 nm in the same nonlinear medium. These output photons at 600 nm had dramatically raised the dark count rates of the detection system. Indeed, in the past, it was claimed that the dark counts, typically in the range of 10^4-10^5 s^{-1} originated from SPDC [14-16, 18, 19]. They are still too high for the single-photon detections. To reduce these elevated dark count rates, a pump beam with its wavelength being longer than that for the input signal was used such that SPDC did not generate any photons at the input signal wavelength [20]. As a result, the dark count rates were reduced to 10^3 s^{-1} only due to anti-Stokes Raman scattering. These rates are still much higher than those from the detectors made from the superconducting

nanowires. For short pump wavelengths, the upconversion of SPDC photons contribute most to the noise photons, while for long pump wavelengths, the upconversion of the anti-Stokes photons is the main noise generation mechanism. Recently, P. Kuo *et al* [21] achieved dark count rates of 600cps by using 1.56μm pump for upconversion at 1.3μm. G. Shentu *et al* [22] implemented ultralow noise up-conversion detector and spectrometer for telecom band with noise equivalent power (NEP) as low as -142 dBm $Hz^{-1/2}$, almost close to the intrinsic dark count rates of commercial Silicon avalanche photodiode.

2.2 Theory of three-wave mixing: sum-frequency generation in periodically poled lithium niobate waveguide

2.2.1 Physical Properties of Lithium Niobate

Lithium niobate ($LiNbO_3$) is centrally important in integrated and guided-wave optics [23]. It is a human-made dielectric material that does not exist in nature. It was first discovered to be ferroelectric in 1949. It is now one of the most widely used electro-optic materials. This ferroelectric material has a trigonal crystal structure as shown in Fig. 2.1 and is characterized by large pyroelectric, piezoelectric, electro-optic and photo-elastic coefficients. Lithium niobate is naturally birefringent. It has useful acoustic wave properties and a relatively large acousto-optic merit. In addition, it exhibits very strong bulk photovoltaic effect. This effect causes efficient charge migration within the material and in combination with the material's linear electro-optic effect, can produce a significant photorefractive effect (optically induced refractive index changes). It is transparent for wavelengths between 350 and 5200 nanometers.

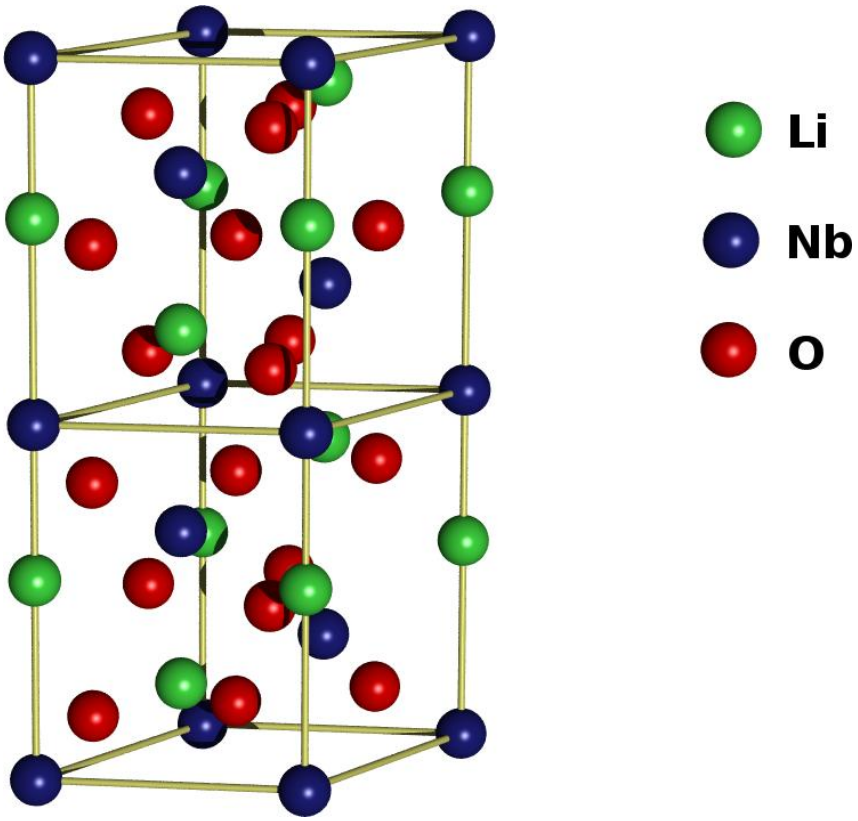

Fig.2.1 Hexagonal unit cell of lithium niobate ($LiNbO_3$) [24]

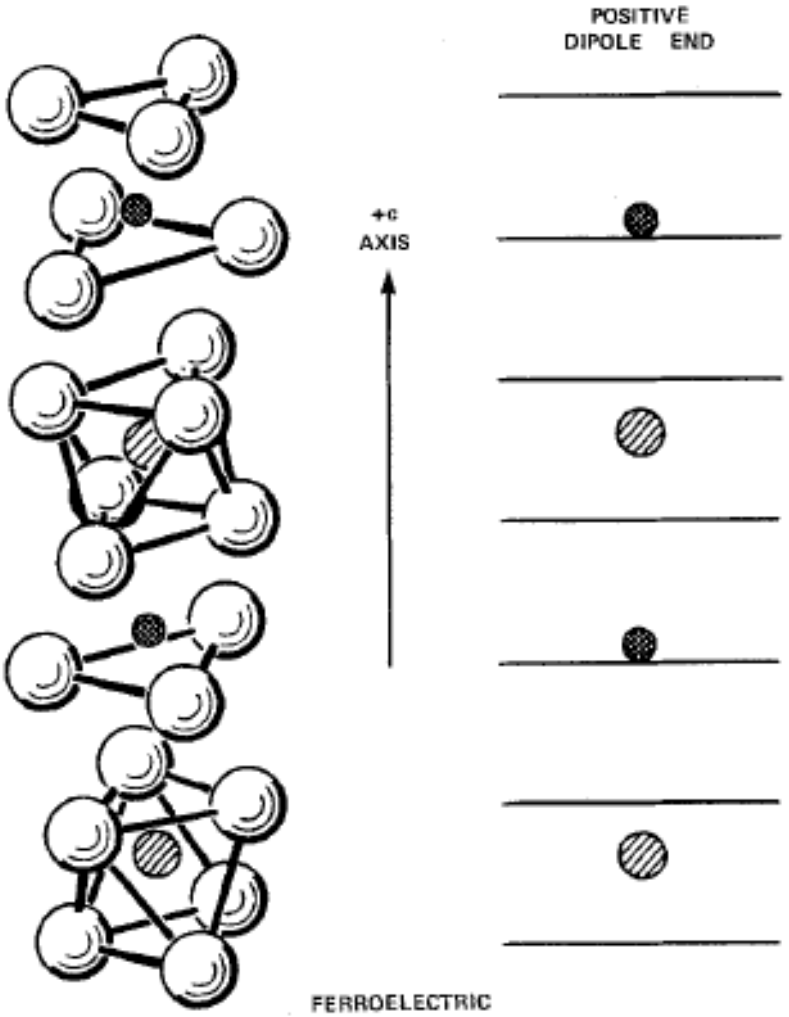

Fig.2.2 Positions of lithium atoms (double cross-hatched circles) and niobium atoms (single cross-hatched circles) with respect to the oxygen octahedral in the ferroelectric phase (T<Tc) of lithium niobate [23]

Lithium niobate's structures at temperatures below its ferroelectric Curie temperature (approximately 1210 degrees centigrade) consists of planar sheets of oxygen atoms in a distorted hexagonal close-packed configuration (See Fig. 2.2). The octahedral interstices formed in this structure are one-third filled by lithium atoms, one third by niobium atoms, and one-third vacant. In the +c direction, the atoms occur in the interstices in the following order: …, Nb, vacancy, Li,

Nb, vacancy, Li … In the paraelectric phase above the Curie temperature, the Li atoms lie in an oxygen layer that is c/4 away from the Nb atom, and the Nb atoms are centered between oxygen layers. These positions make the paraelectric phase non-polar. As the temperature decreases from the Curie temperature, the elastic forces of the crystal become dominant and force the lithium and niobium atoms into new positions. The charge separation resulting from this shift of ions relative to the oxygen octahedral causes $LiNbO_3$ to exhibit spontaneous polarization at temperatures below 1210 degrees centigrade. What is more, the shift of Li atoms will be completely consistent, and so do Nb atoms, travelling towards the opposite direction. The displacement of Li atoms and Nb atoms will generate a very strong internal electric field in the crystal. This is a very important property for $LiNbO_3$ to be periodically poled. By applying a series of periodically aligned electrodes on the lithium niobate crystal along the c axis, the domain of lithium niobate can be inversely polarized if the external electric field exceeds its internal electric field. Thus, the periodically poled lithium niobate (See Fig. 2.3) can be used to realize sum-frequency generation by adjusting the phase difference of the three waves if the poling period is properly chosen [23].

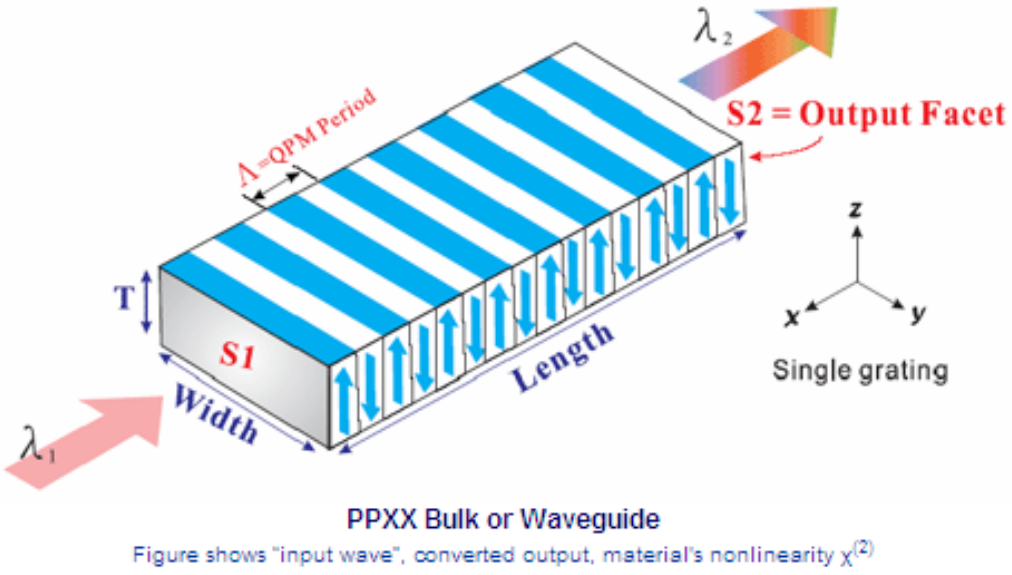

Fig.2.3 PPXX Bulk or Waveguide [25]

The key to producing PPLN is the poling process. The application of an intense electric field can invert the crystal structure, rearranging the crystal at an atomic level. The electric field needed to invert the crystal is very large (~22kV/mm), and is applied for only a few milliseconds to prevent damage to the crystal, after which the periodically reversed structure is permanently imprinted into the crystal structure. The poling voltage must be very carefully controlled so that the poled regions are created with the desired shape.

2.2.2 Frequency Up-conversion

To achieve high efficiency frequency up-conversion, we may utilize an intense pump laser, a very weak input laser, and a bulk crystal periodically poled lithium niobate, quasi-phase-matched to the frequencies of the initial and pump photons [26]. The resulting system up-converts one photon from the input beam and one photon from the pump beam into a single output photon. Due to energy conservation, the output frequency ω_0 is the sum of the input frequency ω_i and the pump frequency ω_p. The nonlinear interactions in a waveguide should always obey the following Maxwell's equations [2]:

$$\nabla^2 E_n - \frac{\varepsilon_n^{(1)}}{c^2}\frac{\partial^2 E_n}{\partial t^2} = \frac{1}{\varepsilon_0 c^2}\frac{\partial^2 P_n^{NL}}{\partial t^2} \tag{2.1}$$

where E_n ($n = p, i, s$)is the scalar electric field of the pump/signal/idler waves, $\varepsilon_n^{(1)}$ is the linear permittivity of the nonlinear material for pump/signal/idler waves, c is the speed of light in vacuum, ε_0 is the vacuum permittivity, and P_n^{NL} is the nonlinear polarization. E_n can be expressed as the product of the slowly varying amplitudes in space (A_n) and the normalized waveguide modes [$\varphi_n(x,y)$]:

$$\begin{aligned} E_n(z,t) &= A_n(z)\varphi_n(x,y)\exp(ik_n z - i\omega_n t) + c.c. \\ P_{i,s}^{NL}(z,t) &= 4\varepsilon_0 d_{eff} E_p E_{s,i}^* \exp(ik_p z - i\omega_p t) + c.c. \end{aligned} \tag{2.2}$$

where

$$k_n = \frac{n_n \omega_n}{c}, n_n^2 = \varepsilon_n^{(1)}$$

Since the fields depend only on the longitudinal coordinate z, we can then replace the Laplace operator ∇^2 by d^2/dz^2. Note that $\iint_{WG}|\varphi_n(x,y)|^2 dS = 1$, and $|d^2A_n/dz^2| << |k_n dA_n/dz|$, we therefore come to the following equation sets that govern the sum-frequency generation process in a periodically poled lithium niobate waveguide, known as the coupled-mode theory [2]:

$$\frac{dE_i}{dz} = i\frac{\omega_i d_Q}{n_i c} E_o E_p^* \exp(i\Delta k_Q z) \tag{2.3}$$

$$\frac{dE_p}{dz} = i\frac{\omega_e d_Q}{n_e c} E_o E_i^* \exp(i\Delta k_Q z) \tag{2.4}$$

$$\frac{dE_o}{dz} = i\frac{\omega_o d_Q}{n_o c} E_i E_p \exp(-i\Delta k_Q z) \tag{2.5}$$

where E_i, E_p, E_o are the electric field strengths of the input, pump, and output beams, respectively. n_i, n_p, n_o are the indices of refraction at the three frequencies; d_Q is the effective nonlinear coefficient; and z is the longitudinal position within the crystal. Δk_Q describes the phase mismatch. Here we assume Δk_Q =0, i.e. perfect phase match.

Assume that we will operate in the non-depletion regime ($E_i \ll E_p$), where the pump beam is not significantly depleted from up-conversion of the input beam, we can approximate $dE_p / dz = 0$. Eqs. (2.3)- (2.5) are then reduce to two coupled first-order differential equations. Solving for E_o under the initial condition $E_o\big|_{z=0} = 0$, we find a sinusoidal oscillation for the output field amplitude, which we then can convert to an efficiency of up-conversion $P_o(z)$:

$$P_o(z) \propto \sin^2(A\sqrt{I_e}\, z) \tag{2.6}$$

where A is a constant. The critical spatial period L_c for this process is given by:

$$L_c = \sqrt{\frac{\pi^2 n_i n_o c^2}{\omega_i \omega_o d_Q^2 \left| E_p^2 \right|}} \tag{2.7}$$

For a crystal of length L_c, where L_c implicitly depends on the pump intensity, the input light will be completely up-converted to the output frequency, and then down-converted back to the original input frequency before leaving the crystal. For a given crystal length L, by choosing $L = 0.5L_c$, we can achieve very high conversion efficiency from ω_i to ω_o.

2.2.3 Phase Match and Quasi-Phase-Match for Three Wave Interactions

2.2.3.1 Phase Matching Techniques for Three-wave Interactions

Giordmaine (1962) and Maker *et al*. (1962) [27] independently showed that one method of phase matching the fundamental and harmonic waves for a second harmonic generation experiment in potassium dihydrogen phosphate (K.D.P) was to utilize the birefringent and dispersive properties of the crystal.

In a particular cone of directions about the optic axis, the ordinary refractive index of the harmonic wave (f_2) is exactly the same as the extraordinary refractive index of the fundamental wave (f_1). In these directions the two waves travel through the crystal with exactly the same speed. Figure 2.4 shows the wave surface of the *e* and *o* waves at the fundamental frequency f_1 and at the second harmonic f_2, two of the surfaces intersecting at the phase matching angle θ_1 measured from the optics axis of the crystal.

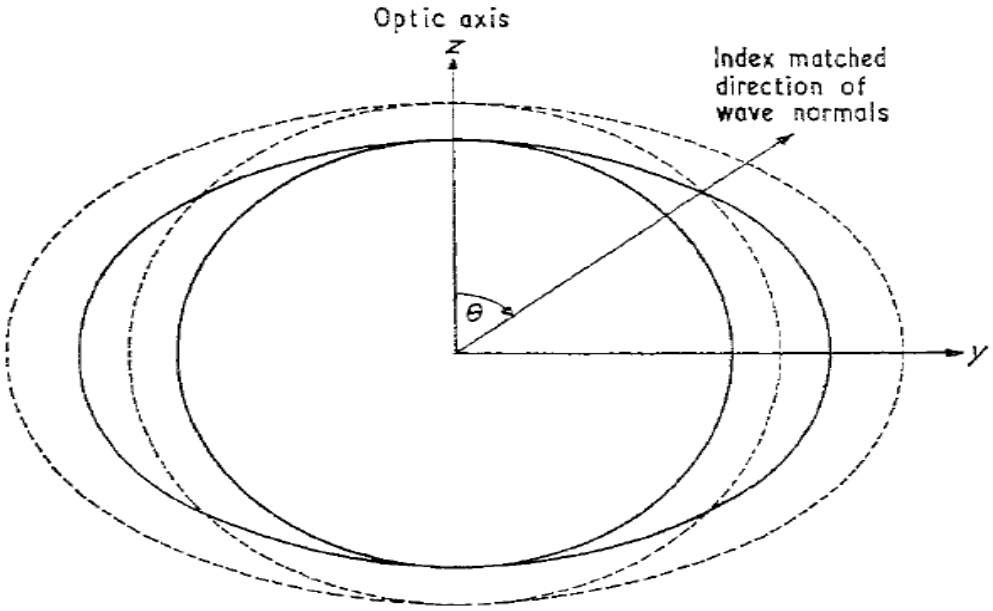

Fig.2.4 Wave surfaces of a negative (n_e<n_o) uniaxial crystal: full lines, wave surfaces at second harmonic frequency; broken lines, wave surfaces at fundamental frequency; θ, phase matching angle [27]

This technique of phase matching may be extended to the more general case of three-coupled wave interactions in the following way. The frequencies and wave vectors of the three waves are governed by the following equations:

$$f_3 = f_1 + f_2 \tag{2.8}$$

$$\mathrm{k}_3 = \mathrm{k}_1 + \mathrm{k}_2 - \Delta\mathrm{k} \tag{2.9}$$

Phase matching is achieved whenever $\Delta\mathrm{k} = 0$.

Now we have

$$\mathrm{k} = \frac{2\pi f n}{c}\mathrm{i} \tag{2.10}$$

where i is the unit vector parallel to k, n the refractive index and c the velocity of light

in vacuum. Using this relationship Eq. (2.7) may be rewritten, under phase matched condition as

$$f_3 n_3 i_3 = f_1 n_1 i_1 + f_2 n_2 i_2 \tag{2.11}$$

It is experimentally convenient if the three waves are propagated with parallel normals, i.e. $i_1=i_2=i_3$. This condition reduces Eq. (10) to the form

$$n_3 = \frac{f_1}{f_1 + f_2} n_1 + \frac{f_2}{f_1 + f_2} n_2 \tag{2.12}$$

Two types of phase matching in birefringent crystals are possible in principle.

Type I. f_1 and f_2 are of the same polarization.

Type II. f_1 and f_2 are of orthogonal polarization.

Possible interaction pairs are listed in Table 1.

Table 1

Positive uniaxial	Negative uniaxial
Phase matching condition	
Type I	Type I
$f_1 \equiv$ e ray, $f_2 \equiv$ e ray, $f_3 \equiv$ o ray	$f_1 \equiv$ o ray, $f_2 \equiv$ o ray, $f_3 \equiv$ e ray
$P(\omega_3) = F_1(\theta, \phi, \mathbf{d})\, E(\omega_1)\, E(\omega_2)$	$P(\omega_3) = F_2(\theta, \phi, \mathbf{d})\, E(\omega_1)\, E(\omega_2)$
$n_3^{\text{ord}} = \frac{f_1}{f_3} n_1^{\text{ext}} + \frac{f_2}{f_3} n_2^{\text{ext}}$	$n_3^{\text{ext}} = \frac{f_1}{f_3} n_1^{\text{ord}} + \frac{f_2}{f_3} n_2^{\text{ord}}$
Type II	Type II
$f_1 \equiv$ o ray, $f_2 \equiv$ e ray, $f_3 \equiv$ o ray	$f_1 \equiv$ e ray, $f_2 \equiv$ o ray, $f_3 \equiv$ e ray
$P(\omega_3) = F_2(\theta, \phi, \mathbf{d})\, E(\omega_1)\, E(\omega_2)$	$P(\omega_3) = F_1(\theta, \phi, \mathbf{d})\, E(\omega_1)\, E(\omega_2)$
$n_3^{\text{ord}} = \frac{f_1}{f_3} n_1^{\text{ord}} + \frac{f_2}{f_3} n_2^{\text{ext}}$	$n_3^{\text{ext}} = \frac{f_1}{f_3} n_1^{\text{ext}} + \frac{f_2}{f_3} n_2^{\text{ord}}$

$f_3 = f_2 + f_1$ and $f_3 > f_2 \geqslant f_1$. We assume that $dn/d\lambda \leqslant 0$ throughout the range from f_1 to f_3.

Table 1 Possible Three-Wave interaction pairs [27]

More generally, if we apply the second-order polarizability tensor d_{ij} on the electric field of incoming waves, we get:

$$\begin{bmatrix} d_{11} & d_{12} & d_{13} & d_{14} & d_{15} & d_{16} \\ d_{21} & d_{22} & d_{23} & d_{24} & d_{25} & d_{26} \\ d_{31} & d_{32} & d_{33} & d_{34} & d_{35} & d_{36} \end{bmatrix} \begin{bmatrix} E_{x_1}E_{x_2} \\ E_{y_1}E_{y_2} \\ E_{z_1}E_{z_2} \\ E_{y_1}E_{z_2} + E_{y_2}E_{z_1} \\ E_{z_1}E_{x_2} + E_{z_2}E_{x_1} \\ E_{x_1}E_{y_2} + E_{x_2}E_{y_1} \end{bmatrix} = \begin{bmatrix} P_x \\ P_y \\ P_z \end{bmatrix}$$

(2.13)

For lithium niobate, since it belongs to the 3*m* point group, its polarizability tensor has the form of:

$$\begin{bmatrix} 0 & 0 & 0 & 0 & d_{15} & -d_{22} \\ -d_{22} & d_{22} & 0 & d_{15} & 0 & 0 \\ d_{15} & d_{15} & d_{33} & 0 & 0 & 0 \end{bmatrix}$$

2.2.3.2 Quasi-Phase-Match for Three Wave Interactions

In the polarizability tensor of lithium niobate, we should pay special attention to the d_{33} term, which is observably greater than other terms. d_{33} in lithium niobate can be as large as -27pm/V, while d_{31} (d_{15}) is only -4.64pm/V, almost an order of magnitude smaller than d_{33}. No doubt we should take advantage of d_{33} to achieve more efficient photon conversion. Since the length of crystal required to achieve conversion is inversely proportional to the nonlinear coefficient, larger d values mean that people can achieve more conversion in a fixed length of crystals, thus enhancing the conversion efficiency.

However, d_{33} is only related to the z part of the polarization of the two source waves and results in the z-direction polarization of the output photon. That is to say we would better use two z-polarized waves to get a z-polarized output wave. Because all nonlinear crystals are also dispersive (i,e. $n = n(\omega)$), it is impossible to satisfy Eq. (2.10) if all three beams are polarized in the same direction, as in Table 1 there is no such interaction pairs as $o + o \to o$ or $e + e \to e$. In order to take advantage of the d_{33} we must have a way to satisfy momentum conservation when all the interacting fields are identically polarized. This can be understood by noting that in Eqs. (2.3)~(2.5), where Δk_Q is taken to be the parameter which describes the regular phase-matching condition, the sign of dE_o / dz changes every time z changes by $\pi / \Delta k_Q$. Consequently, any increase of E_o in the first $\pi / \Delta k_Q$ length of crystal is immediately canceled out by the second $\pi / \Delta k_Q$ length of crystal. In quasi-phase-matching, the crystal is poled to create periodic ferroelectric domains, which contributes to the momentum, thus compensating the mismatched

momentum part. The alternating poled ferroelectric domains have the effect of changing the sign of the nonlinear coefficient (See Fig. 2.5). By properly selecting poling period Λ, we can create a quasi-phase matching situation which will allow us to take advantage of the larger d_{33} nonlinear coefficient.

The phase match condition is given by:

$$\Delta k_Q \equiv k_o - k_i - k_p - \frac{2\pi}{\Lambda} = 0 \tag{2.14}$$

where k_o, k_i, k_p are the wave numbers of the three beams in the crystal.

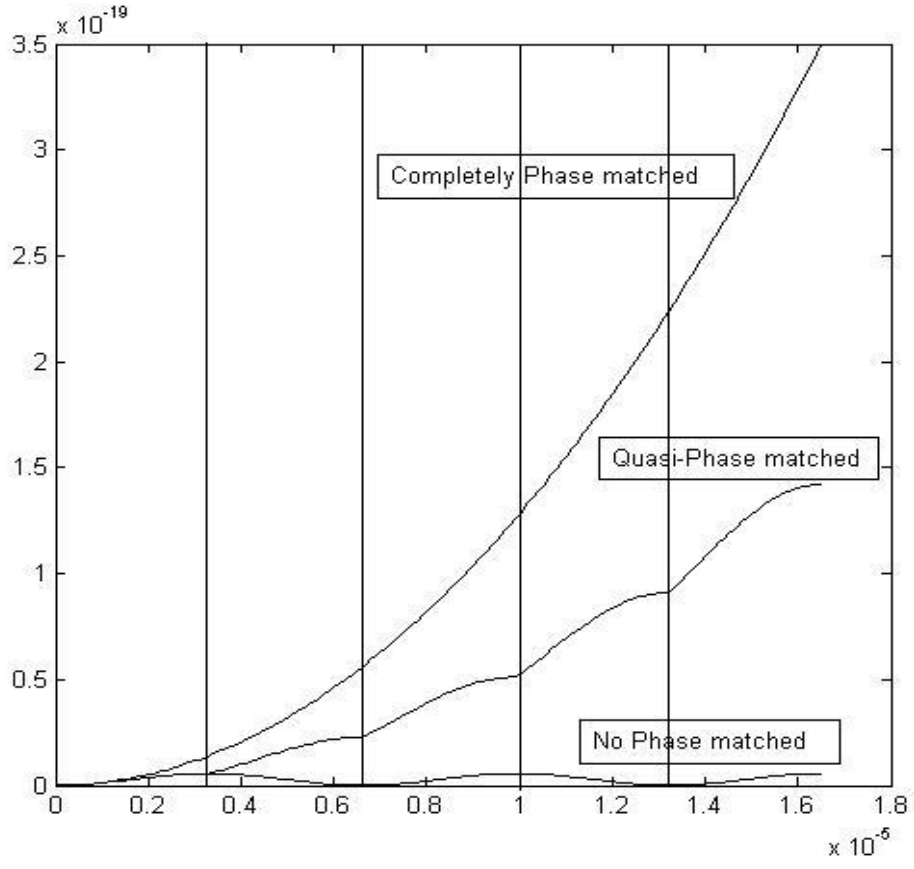

Fig. 2.5 Comparison of Completely Phase Matched condition, Quasi-phase matched condition and no phase matched condition. X-axis represents the length in crystal; Y-axis represents the output electric field strength [27]

2.2.4 Temperature-dependent Sellmeier Equation

The temperature-dependent Sellmeier equation describes the variation for refractive index n with incident wavelength λ and crystal temperature, T. It can be used to find the poling period and approximate temperature for quasi-phase matching. Jundt *et al* [28-32] give that:

$$n_e^2 = a_1 + b_1 f + \frac{a_2 + b_2 f}{\lambda^2 - (a_3 + b_3 f)^2} + \frac{a_4 + b_4 f}{\lambda^2 - a_5^2} - a_6 \lambda^2 \tag{2.15}$$

where a_1=5.35583, a_2=0.100473, a_3=0.20692, a_4=100, a_5=11.34927, a_6=1.5334×10^{-2}, b_1=4.629×10^{-7}, b_2=3.826×10^{-8}, b_3=-0.89×10^{-8}, b_4=2.657×10^{-5}, and $f = (T - 24.5)\times(T + 570.82)$ for PPLN crystals. T is the crystal temperature in Celsius Degree.

Sellmeier Equation shows that we can adjust the temperature of PPLN to reach the best quasi-phase match condition. In other words, tuning operation temperature would allow us to tune the working signal wavelength.

2.3 Experimental Setup

In this Section, we demonstrate our experimental setup on the single-photon detections based on frequency up-conversion at the pump wavelength of 980/1920 nm [33,34]. Fig. 2.6 is the experimental setup for the single-photon detections. As shown in Fig. 2.6, a CW tunable signal beam in the communication band (tunable from 1.46μm to 1.58μm) could be attenuated by up to ten orders of magnitude with two fixed fiber attenuators and one variable attenuator. It was combined with a strong CW pump beam at 980/1920 nm by a wavelength division multiplexer (WDM) before being coupled into the 3-cm-long PPLN waveguide, mounted inside a temperature-controlled oven with the temperature accuracy being 0.1°C. The poling period Λ_G is 10.16μm. A 40× microscope objective was used to collect the up-converted output beam in the visible or near-infrared range. A set of filters were used to remove the two input beams and their second-harmonic outputs. The up-converted photons generated at 600/803 nm were subsequently coupled into a single-mode fiber using a free-space coupling system, and then coupled into a single-photon counting module (SPCM). The key optical component of the free-space coupling system was an aspherical lens, which was used to focus the up-converted beam and coupled into a single-mode fiber with reduced optical aberrations. The free-space coupling system was capable of blocking the unwanted photons from entering the counting module, such as second harmonic beam generated by the pump wave. The actual setup layout is shown in Fig. 2.7 and Fig. 2.8.

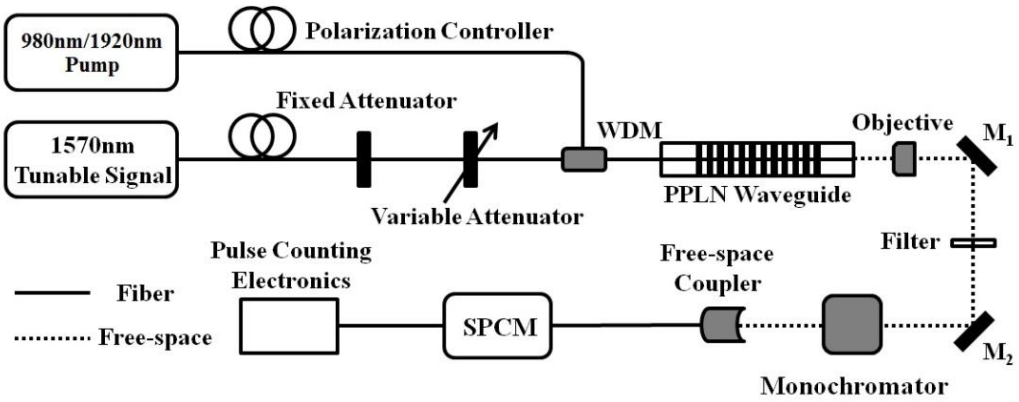

Fig. 2.6. Illustration of experimental setup for single-photon detections based on frequency up-conversion.

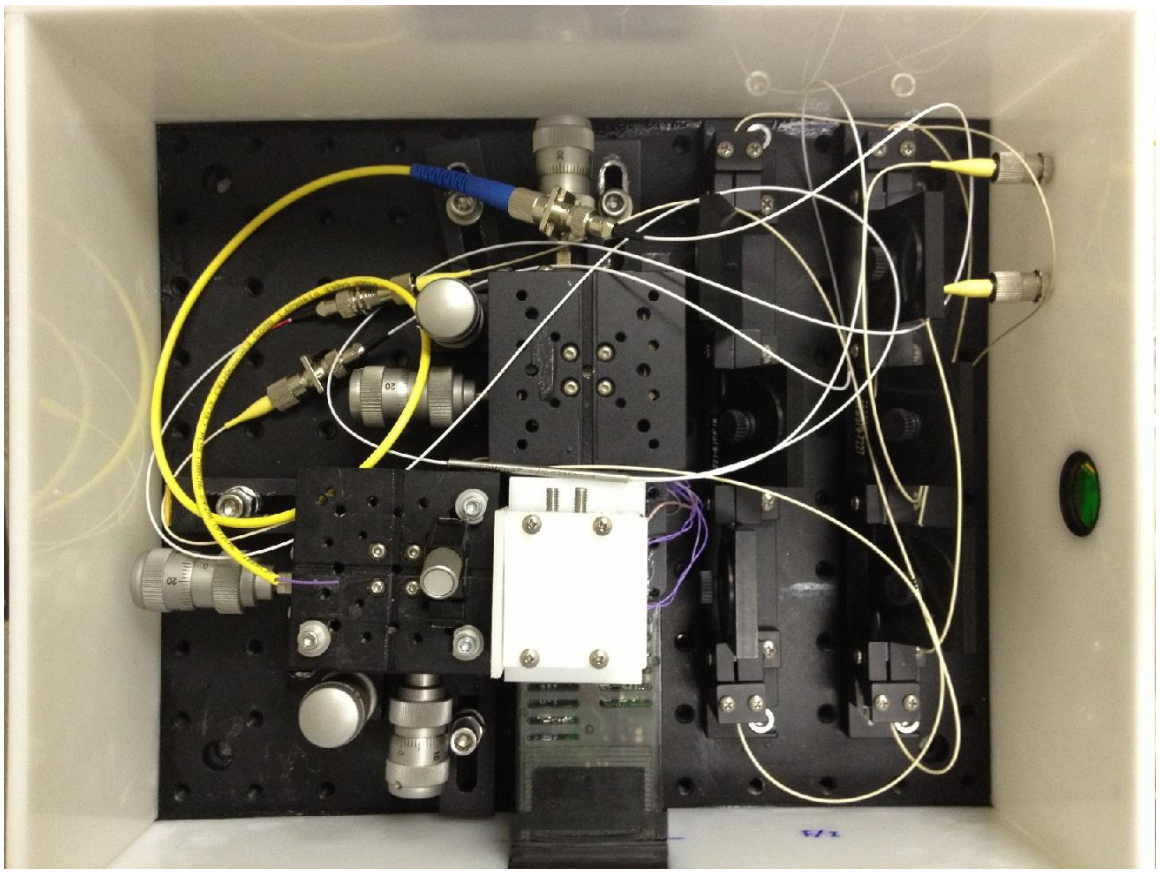

Fig. 2.7 Demonstration of actual setup

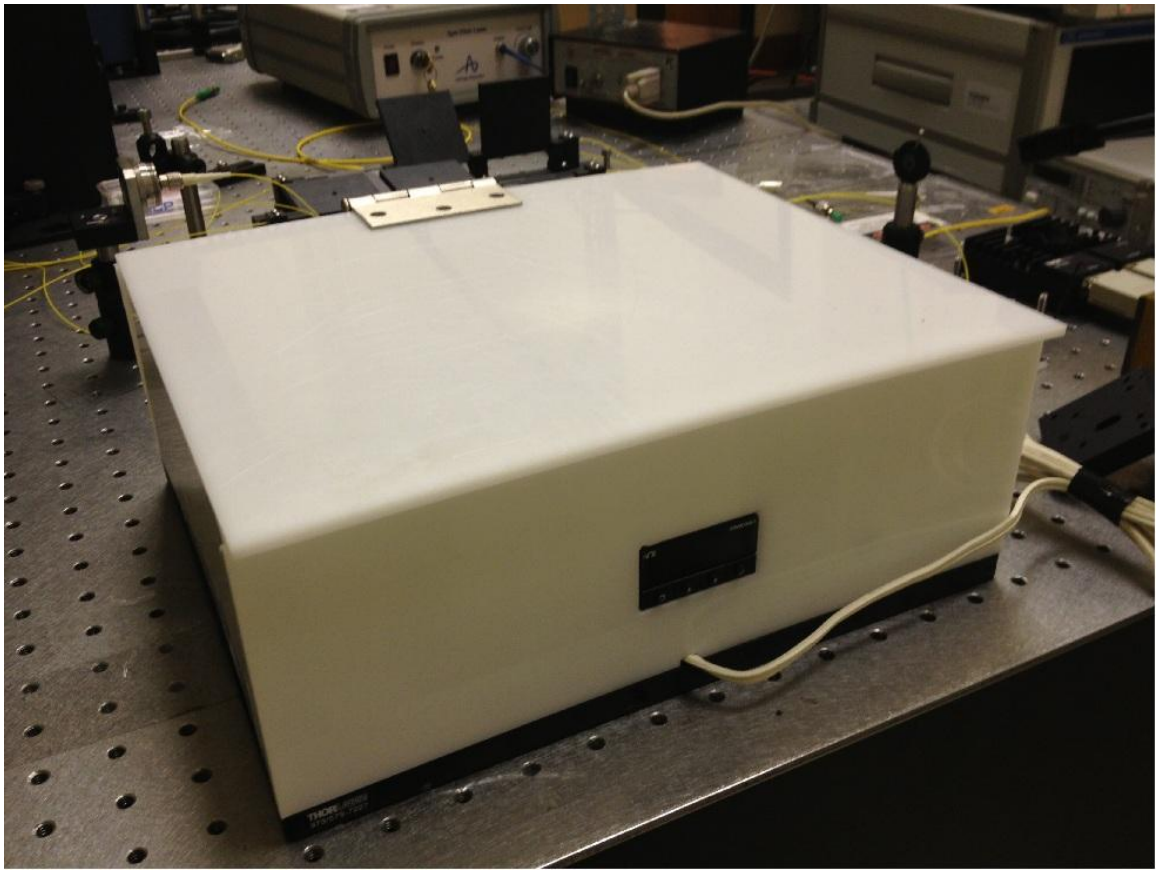

Fig. 2.8 Overall look of the whole detection system

2.4 Results and Discussion

2.4.1 Waveguide Characteristics

1) Waveguide for interaction 980 nm + 1550 nm -> 600 nm

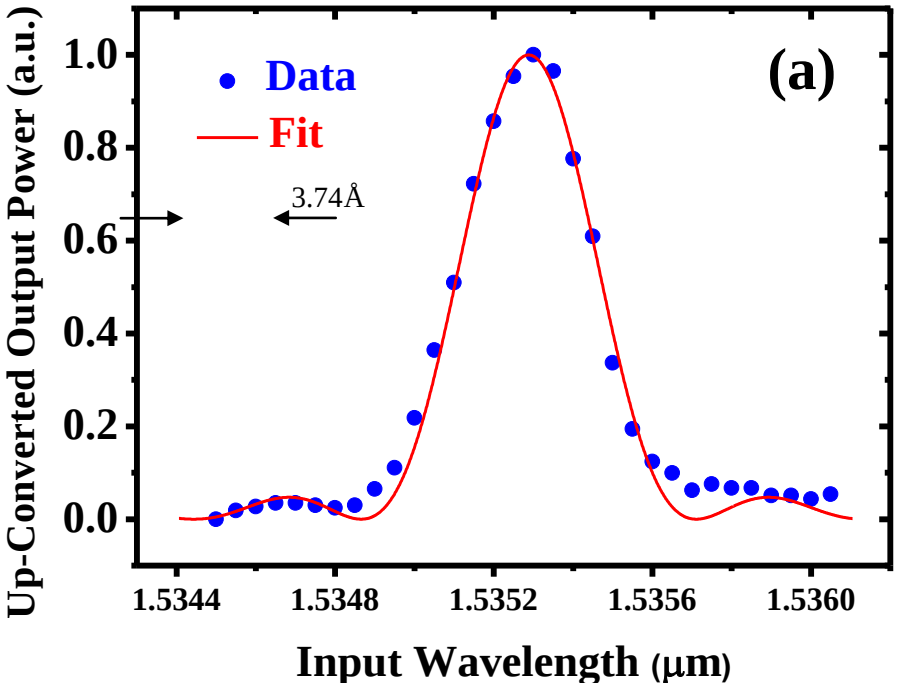

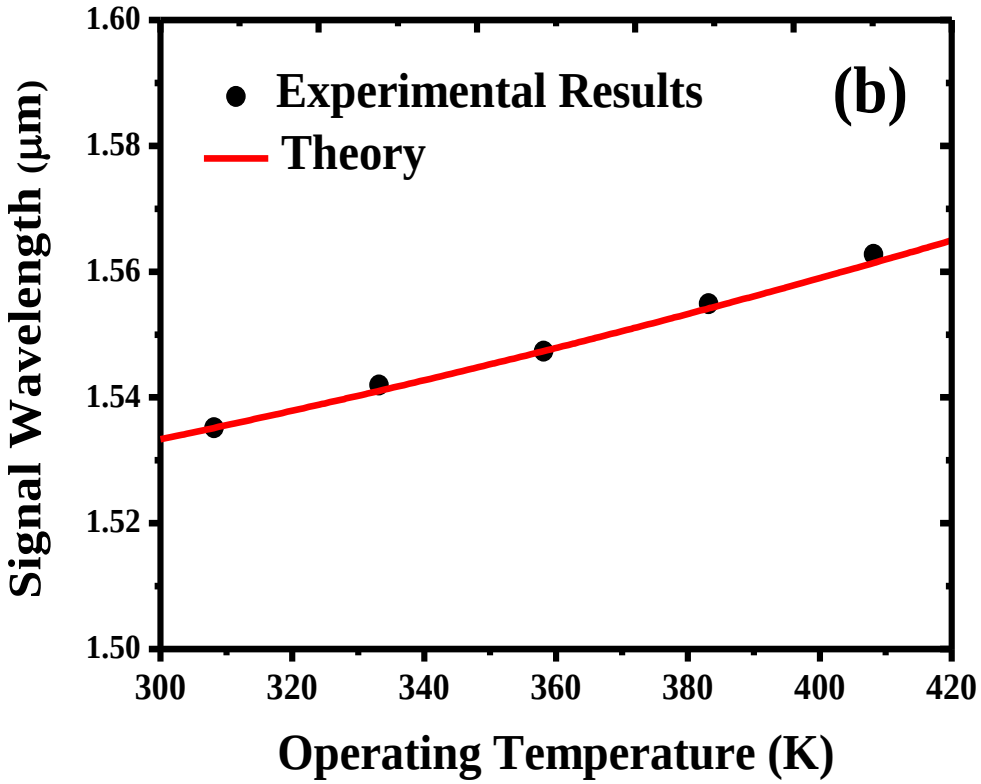

Fig.2.9 (a) Phase-matching tuning curve for PPLN waveguide, data (dots) & least square fitting (solid line). FWHM=3.74Å. (b) Temperature tuning curve, data (dots) and theoretically calculated curve (solid line).

2) Waveguide for 1920 nm + 1550 nm -> 803 nm

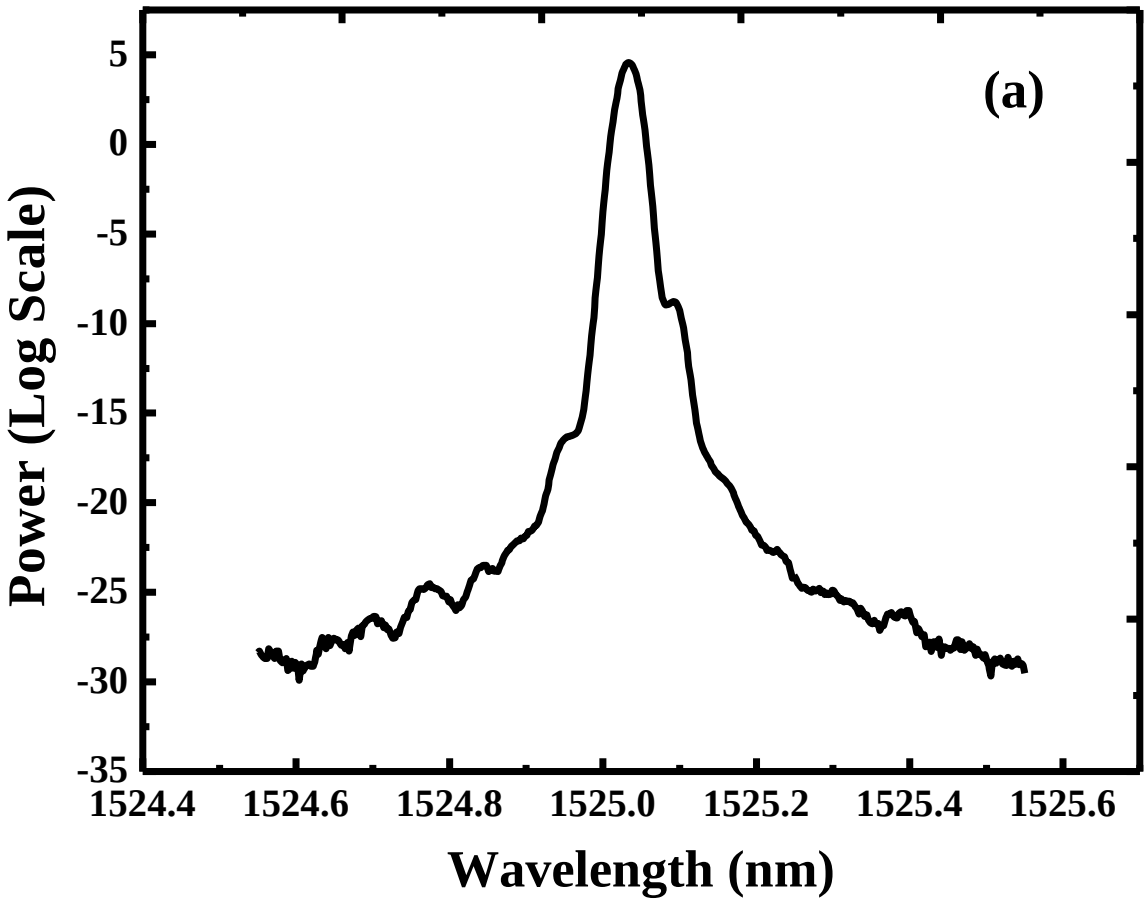

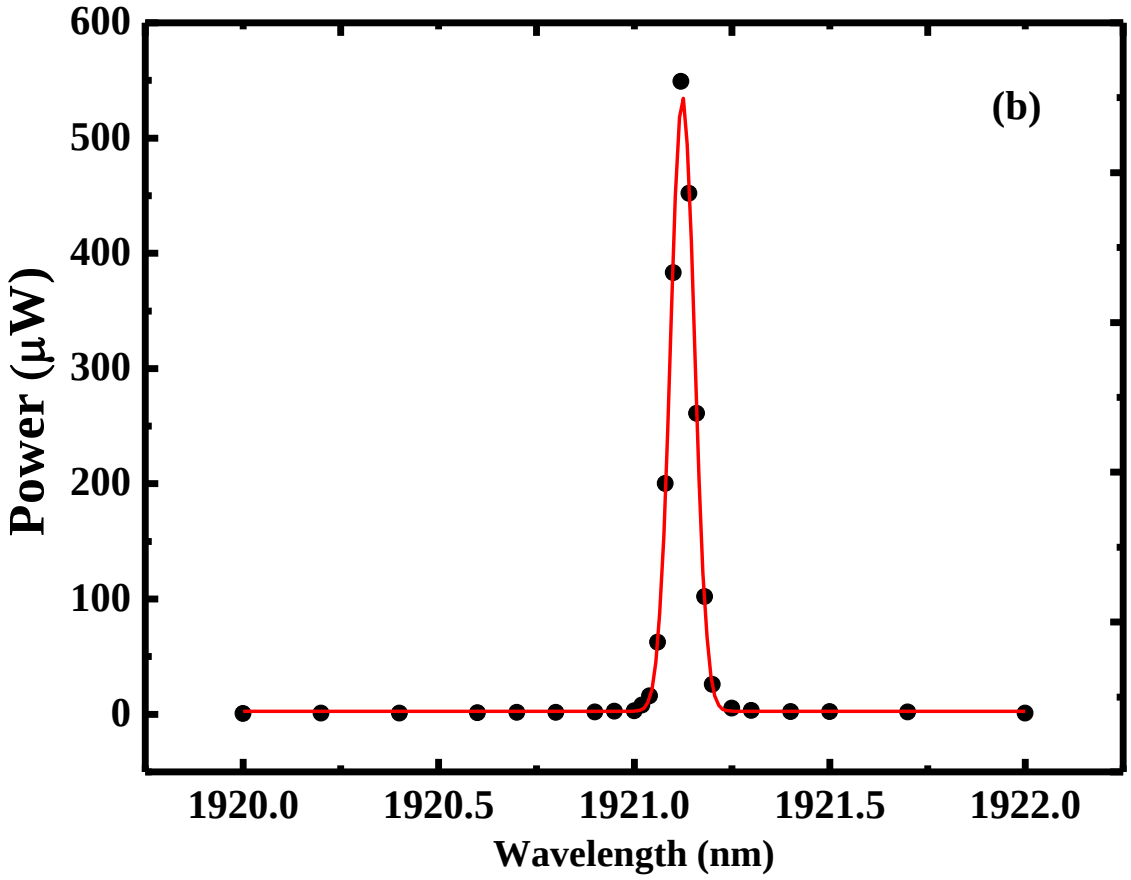
(b)
Power (μW)
600
500
400
300
200
100
0
1920.0
1920.5
1921.0
1921.5
1922.0
Wavelength (nm)

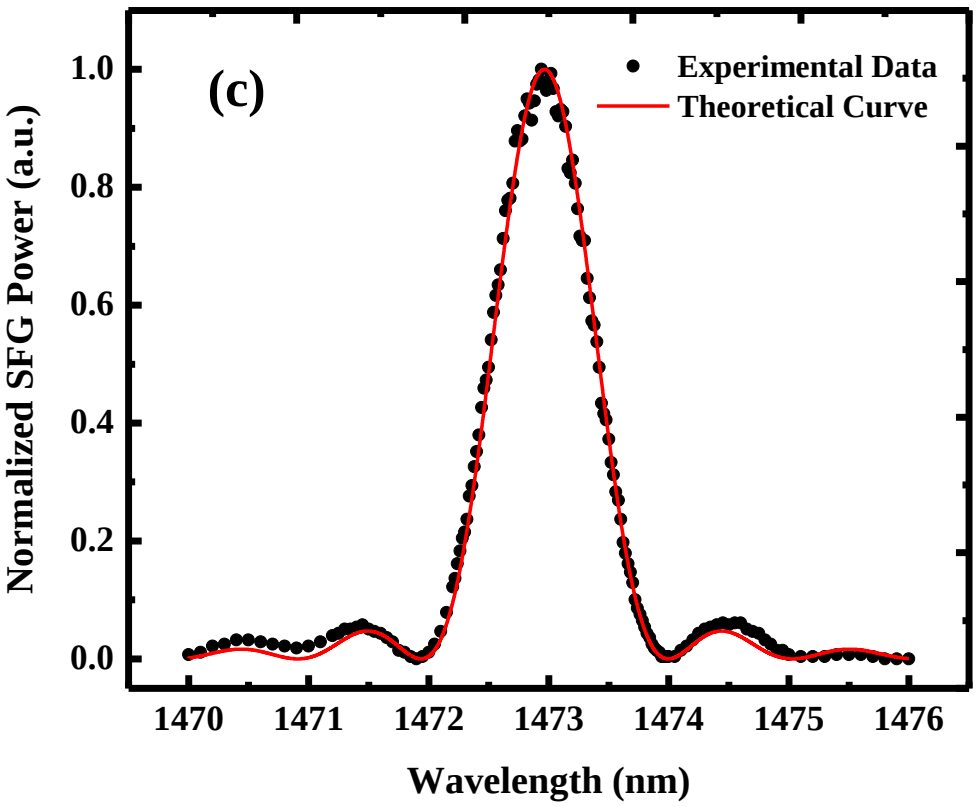
(c)
Experimental Data
Theoretical Curve
Normalized SFG Power (a.u.)
1.0
0.8
0.6
0.4
0.2
0.0
1470
1471
1472
1473
1474
1475
1476
Wavelength (nm)

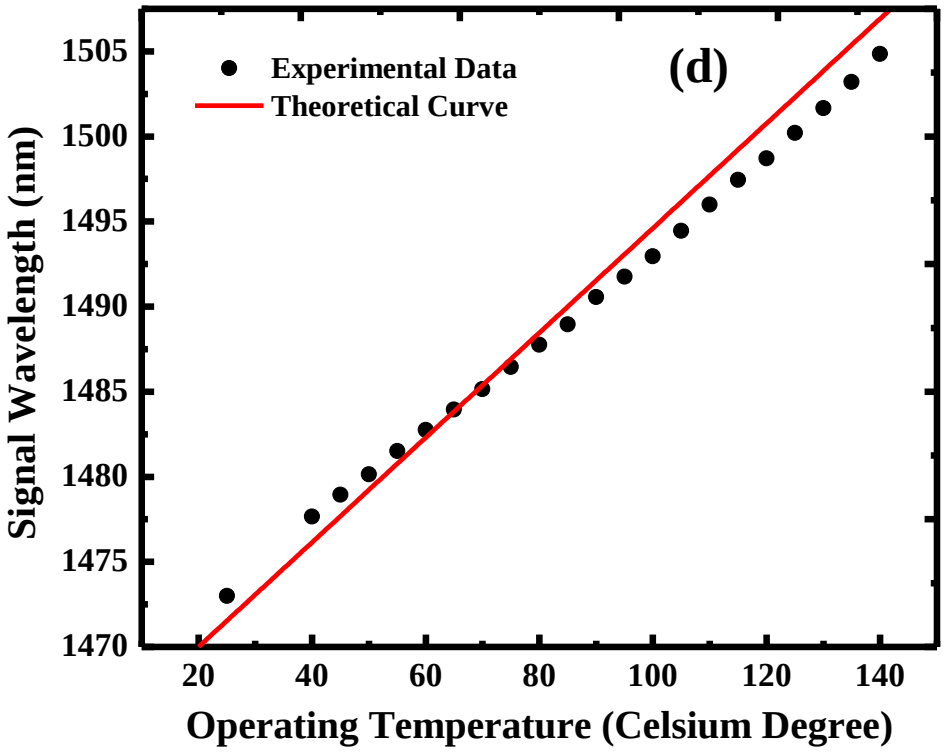

Fig. 2.10 (a) C-band laser spectrum, bandwidth < 0.1 nm (b) 1920 nm laser spectrum, bandwidth = 0.06 nm (c) phase matching curve, and (d) optimum working wavelength at given temperatures

We first measured the phase-matching tuning curve for the periodically poled lithium niobate waveguide by fixing the pump wavelength at 980nm while scanning the signal wavelength from 1535.5nm to 1536.2nm, and fixing pump wavelength at 1920 nm while scanning the signal wavelength from 1470 nm to 1476 nm, as shown in Fig.2.9 (a) and Fig. 2.10 (c), respectively. Theoretically, one can fit a normalized phase-matching tuning curve by:

$$P(\lambda_{sig}) = \mathrm{sinc}^2\left(\frac{\Delta k(\lambda_{sig}) L_{eff}}{2}\right) \tag{2.16}$$

Here, Δk is the wave vector mismatch among the three interaction waves defined as $\Delta k = k_{\mathrm{SFG}} - k_{\mathrm{Pump}} - k_{\mathrm{Signal}} - \frac{2\pi}{\Lambda}$, where Λ denotes the poling period and L_{eff} stands for the effective interaction length. Lease square fitting deduces the effective interaction length to be 29 mm, corresponding to a FWHM bandwidth of 3.74Å, as illustrated in Fig.2.9 (a) and Fig. 2.10 (c). The actual bandwidth is broader than the theoretical value of 3.95 Å deducted from the entire crystal length, 30mm. For pump wavelength of 1920nm, the effective interaction length is almost the same as the waveguide length. Deviation may originate from domain imperfection of the PPLN chip [35].

We also measured the operating temperature tuning data and compared them with theoretically calculated curve based on temperature-dependent Sellmeier equation for $LiNbO_3$ [32]. The results are shown in Fig. 2.9 (b) and Fig. 2.10 (d). The data and the curve coincide well, giving a temperature tuning rate of 0.259 nm/˚C at pump wavelength λ_p=980nm, and 0.273 nm/˚C at pump wavelength of λ_p=1920nm.

2.4.2 Single Photon Detection

We measured the power of up-converted output photons for signal wavelengths from 1535nm to 1556nm under five discrete operating temperatures vs. pump power at 980nm, as illustrated in Fig. 2.11 (a). The injected signal power level is stabilized at 1mW. The similar power dependence curves at different operating temperatures shows good thermal stability of the oven. At operating temperature of 60℃, we observed a maximum internal conversion efficiency of 62.1% with input pump power of 84.02mW. Subsequently, we varied the input signal photon injection rate and recorded the detected SFG photon rates at three different pump power levels, see Fig. 2.11 (b). Linear dependence was expected since the probe signal power levels were extremely low. The slope of each fitted line represents conversion efficiencies, which equal to 3.2%, 12.8% and 62.1%. These values have good agreement with those demonstrated in Fig. 2.11 (a). Generally, the detected photon counts should not exceed 10 Million counts per second, for which might induce detection response nonlinearity in the Si APD. We performed averages for multiple times at which SFG counts are comparable to or even less than the APD noise level. The lowest SFG photon count rates we observed from the SPCM were $14.7s^{-1}$. By using typical detection efficiency of SPCM at 600nm of 65%, measured filter transmission of 60%, maximum internal conversion of 62.1%, and free-space coupling efficiency of 75%, we deduced minimum detectable signal photons at C-band of $81s^{-1}$ in the waveguide. This is a record-low detectable photon rate ever achieved.

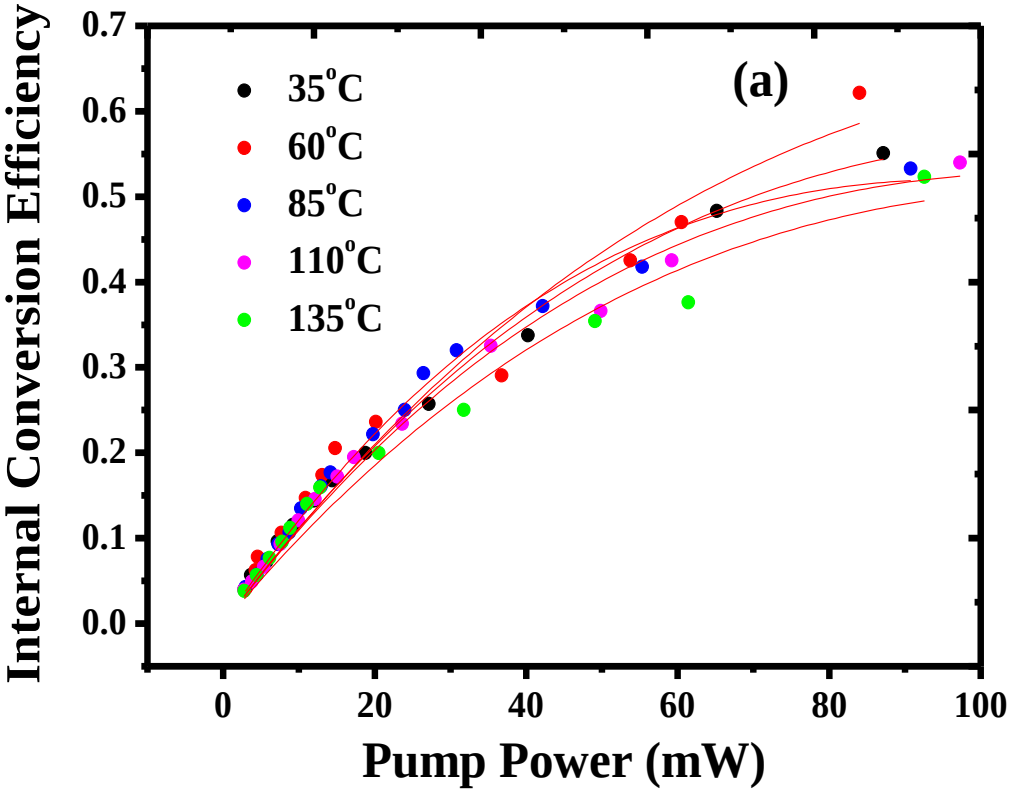
Internal Conversion Efficiency
0.7
0.6
0.5
0.4
0.3
0.2
0.1
0.0
35°C
60°C
85°C
110°C
135°C
(a)
0
20
40
60
80
100
Pump Power (mW)

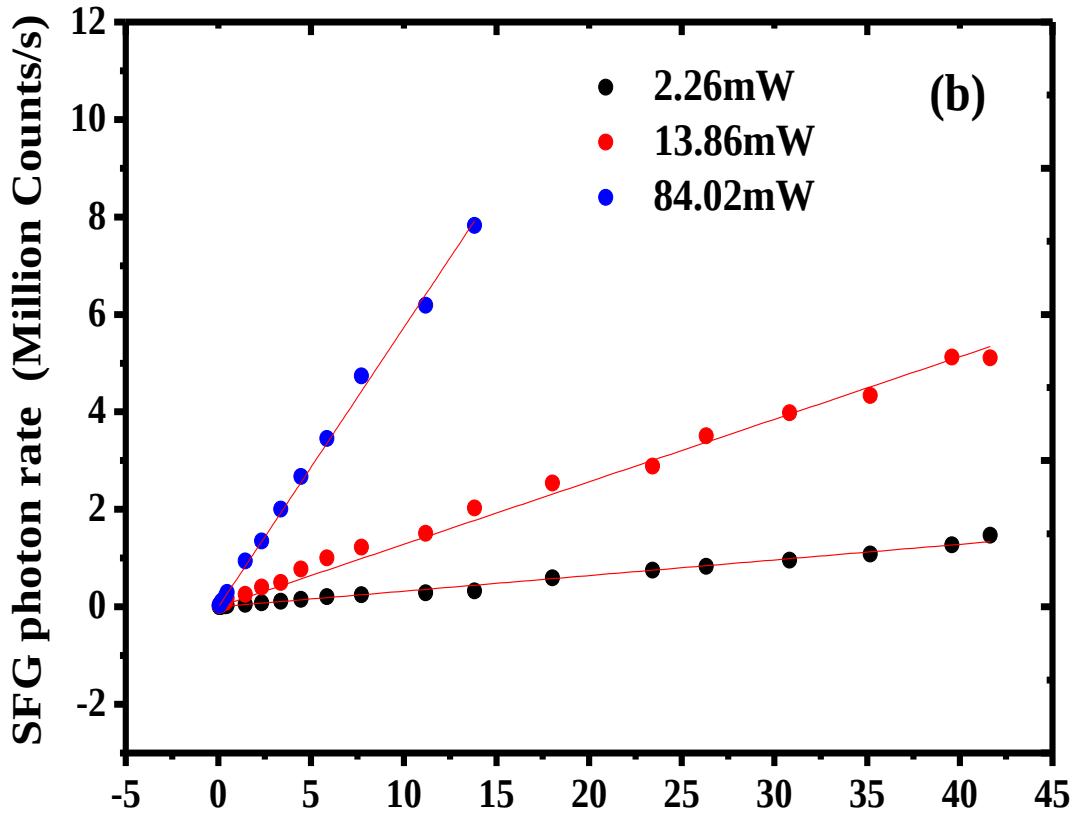

Fig.2.11 (a) (Solid dots) internal conversion efficiency vs. pump power at 980nm under different operating temperatures. (Solid curves) $\sin^2()$ theoretical fit. (b) (Solid dots) Signal photon rate vs. detected SFG photon rate at different pump levels. (Solid lines) linear least-square fit.

To determine the dark count rate affected by pump beam only, we switched off the weak signal probe, leaving only the pump on. We tuned the pump power from 2mW to 80mW, and we did not see an increase in the dark count rates, which remained steady at 45 counts per second. In order to be more convincing, we recorded the dark count rates spectrum by inserting a monochrometer in front of the free-space coupler. Fig. 2.12 demonstrated the counts spectrum at full response range for the Si APD, from 450nm to 1100nm, with or without signal beam at 1550nm band. The dark counts, when the signal was turned off, showed a nearly flat line (red line) at the level of 45 counts per second for all responsive wavelengths. This could even be further reduced since we confirmed that these dark counts were coming from 980nm photons scattered into free space coupler by surrounding objects. When the signal beam was switched on, we see only the up-converted photons at around 600nm. The figure demonstrate clearly that we have completely blocked the noise photons, including un-phase-matched SHGs of both pump and signal photons, as well as parametric fluorescence caused by spontaneous parametric down conversion (SPDC) of the pump photons.

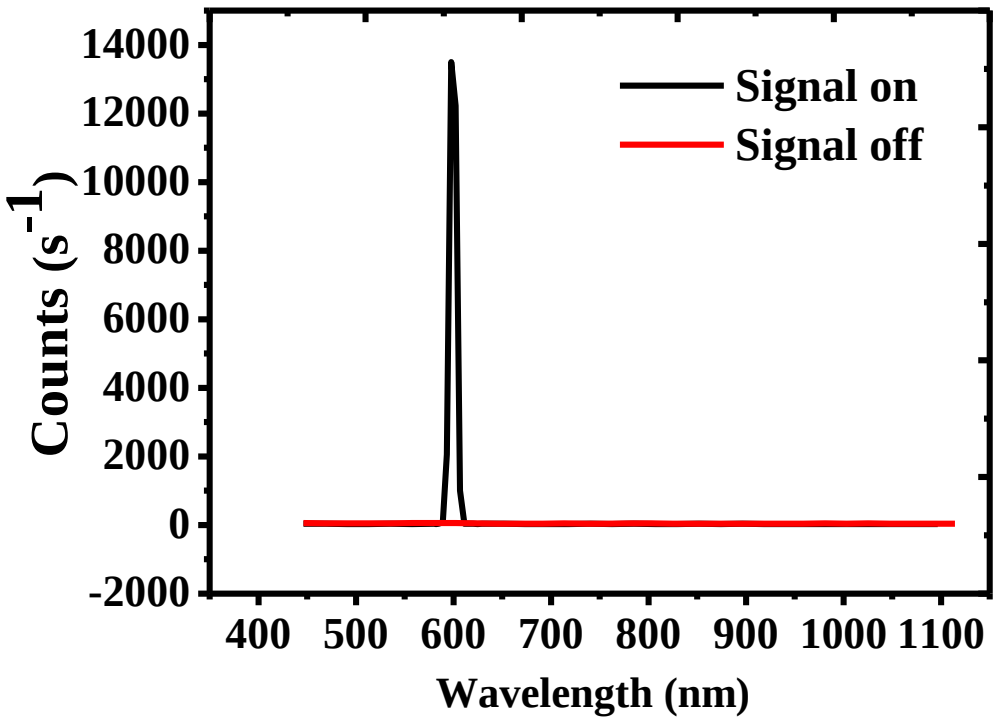

Fig.2.12 Counts spectrum. Pump is always turned on. (Red solid line) Signal is turned off. i.e. dark counts. (Black solid line) Signal is turned on. No other wavelength peaks were found.

2.5 Analysis of noise photon generation

The noise sources for sum-frequency generation based single photon detector are re-upconversion of pump-induced Raman scattering and parametric down-conversion. J. S. Pelc [36] studied the Raman scattering and discovered that for pump of 980nm, the portion shifted to 1550nm due to Raman scattering is negligible. Therefore, in this section, we only consider and investigate spontaneous parametric down-conversion and its subsequent frequency upconversion. We then calculate the dark count rates and make comparison between our theoretical results with the measured values. We investigate the generation of the signal photons by SPDC from the pump beam as well as the subsequent re-upconversion process. The theory for estimating the signal photon numbers generated by SPDC has been well developed [37,38] and observed [39]. However, there has been no theory published for the specific configuration and structure used in our experiment [33]. The commonly accepted method for calculating the SPDC photon counts is semi-classic, i.e. using the classic governing equations to describe the down-conversion process denoted as ω_3 (pump) ->ω_1 (idler) +ω_2 (signal), while finding the total power of mode with frequencies near the idler mode (ω_1) by putting one photon into each mode and use it as effective inputs for obtaining the output power of driven signal mode (ω_2) [37,38]. The pump field (E_p) is assumed to be un-depleted and thus remains constant. We therefore come to the following equation sets that govern the noise photon generation process, as developed from section 2.2:

$$\begin{cases} \dfrac{dA_i}{dz} = \dfrac{2i\omega_i^2 d_{NL}}{k_i c^2} U_1 A_p A_s^* \exp(i\Delta k_N z) \\ \dfrac{dA_s}{dz} = \dfrac{2i\omega_s^2 d_{NL}}{k_s c^2} U_1 A_p A_i^* \exp(i\Delta k_N z) + \dfrac{2i\omega_s^2 d_{NL}}{k_s c^2} U_2 A_p^* A_u \exp(-i\Delta k_S z) \\ \dfrac{dA_u}{dz} = \dfrac{2i\omega_u^2 d_{NL}}{k_u c^2} U_2 A_p A_s \exp(i\Delta k_S z) \end{cases} \tag{2.17}$$

where A_i and A_s are defined as before. A_u is the slowly varying electric field amplitude in space for the sum-frequency output, here mainly responsible for the noise. The two phase mismatch vectors, Δk_N and Δk_S, for the down-conversion and upconversion process respectively, are defined as:

$$\begin{aligned} \Delta k_N &= k_p - k_i - k_s = \frac{2\pi n_p}{\lambda_p} - \frac{2\pi n_i}{\lambda_i} - \frac{2\pi n_s}{\lambda_s} \\ \Delta k_S &= k_u - k_p - k_s = \frac{2\pi n_u}{\lambda_u} - \frac{2\pi n_p}{\lambda_p} - \frac{2\pi n_s}{\lambda_s} \end{aligned} \tag{2.18}$$

U_1 and U_2 are the mode coupling coefficients:

$$\begin{aligned} U_1 &= \iint_{WG} \varphi_i \varphi_s \varphi_p dS \Big/ \iint_{WG} dS \\ U_2 &= \iint_{WG} \varphi_u \varphi_s \varphi_p dS \Big/ \iint_{WG} dS \end{aligned} \tag{2.19}$$

The initial conditions are $A_s(0)=A_u(0)=0$, and $A_i(0)$ is derived later. In fact, the periodically inversed domain along the propagation direction caused the nonlinear coefficient to flip sign accordingly. The nonlinear coefficient d_{NL} is then a function of propagation distance, and can be expressed as:

$$d_{NL}(z)=\begin{cases} d_{33} & m\Lambda \le z \le m\Lambda+\Lambda/2 \\ -d_{33} & m\Lambda-\Lambda/2 \le z \le m\Lambda \end{cases} \tag{2.20}$$

where we assume the PPLN chip has $2m$ or $2m+1$ periods and m is an integer. Although we may expand the nonlinear space-varying coefficient into Fourier series, we should include all terms and should not neglect the cross terms since the grating periods are not designed to enhance the first SPDC process.

We use the zero-point energy of the electromagnetic modes as an effective input field with an intensity equivalent to one photon per mode, denoted here as $A_i(0)$ [37,38]. Consider a PPLN waveguide structure, where its width W and depth d are much shorter than its length L, see Fig. 2.13. In such a case, it allows us to use the one-dimentional density of states to calculate the input idler power density in the range of k_i to k_i+dk_i:

$$\begin{aligned} dI_i(0) &= \frac{dk_i}{2\pi/L}\hbar\omega_i\frac{c}{Vn_i} \\ dk_i &= d\left(\frac{n_i\omega_i}{c}\right)=\frac{2\pi n_i}{\lambda_s^2}d\lambda_s \end{aligned} \tag{2.21}$$

Since $dI_i(0)=2n_i\varepsilon_0 c|A_i(0)|^2$, we achieved an explicit expression for $|A_i(0)|^2$:

$$|A_i(0)|^2=\frac{hc}{2n_i\varepsilon_0\lambda_i\lambda_s^2 S}d\lambda_s \tag{2.22}$$

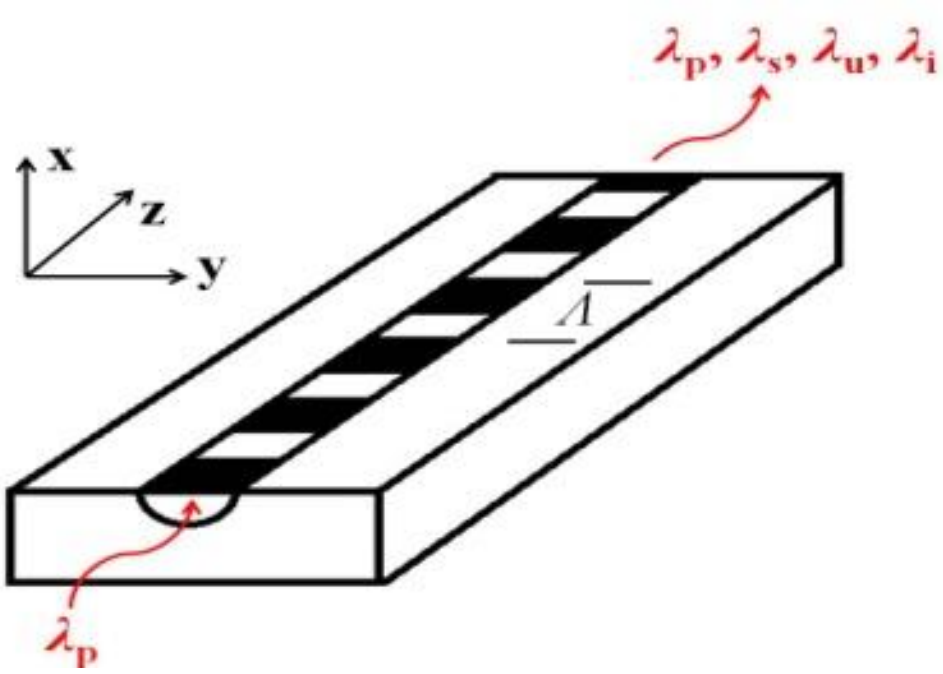

Fig. 2.13. Structure and configuration for SPDC and frequency up-conversion in a PPLN waveguide. A pump wave is coupled from the input facet. Due to nonlinear parametric processes, multiple frequencies can be generated at the output facet.

We run numerical simulations based on (2.17) and illustrate the noise power evolution against propagation distance z. A typical solution curve for the noise photon count rate is shown in Fig. 2.14. As can be seen from the figure, the noise SFG power experienced a sinusoidal oscillation with regard to the propagation distance, and reached its peak at around z = 3 cm. The numerical simulation was run by assuming that $d\lambda_s$ = 0.357 nm when calculating the value for $|A_i(0)|^2$. In fact, the total noise counts should be the summation of the SFG generation at the output facet over wavelengths adjacent to the target wavelength, i.e. 1550 nm. Here, we take the integration for λ_s from 1549.2 nm to 1550.8 nm (which is broad enough to cover the main *sinc* function peak of the phase matching curve, see Fig. 2.15, to reach total noise counts of 397 s^{-1}. Based on measured collection efficiency of 90.0%, the filter transmittance of 60.0%, the coupling efficiency of 75.0% of into the Si APD, and the detection efficiency of 65.0% for the photons around 600 nm in the Si APD, we have obtained an effective detection efficiency of 26.3% and dark count rate of 104.5 s^{-1}.

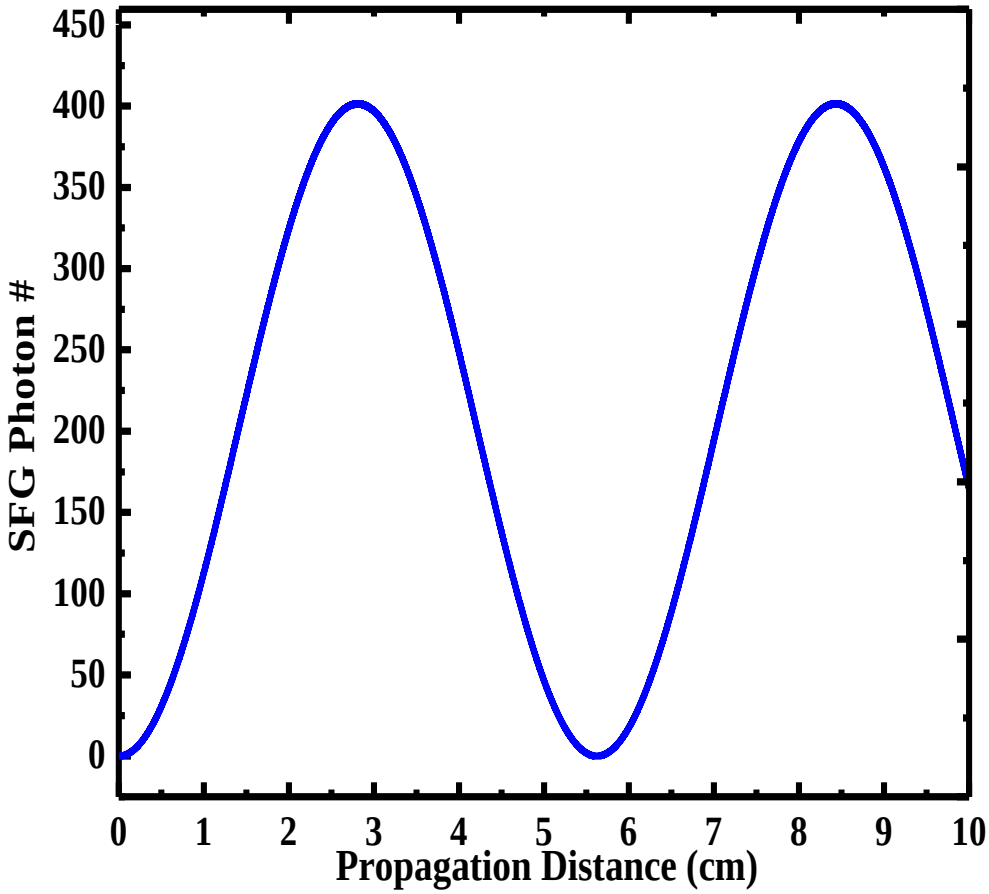

Fig. 2.14. Noise photon number at up-converted wavelength vs. propagation distance in the unit of cm.

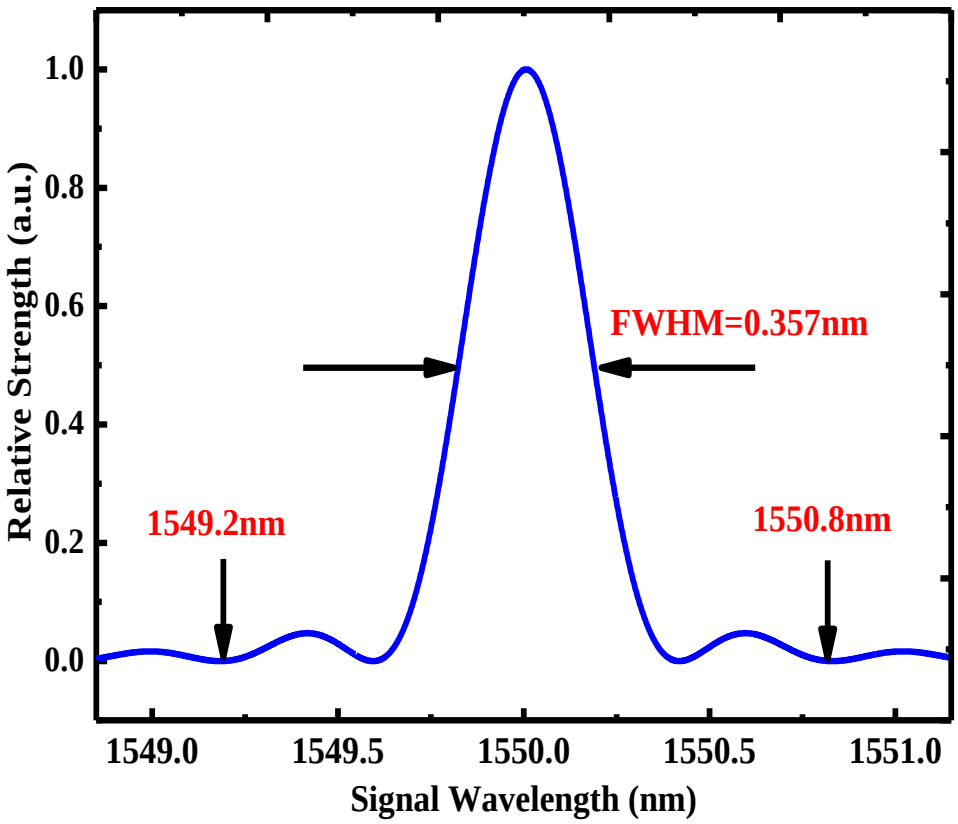

Fig. 2.15. Phase matching curve for up-conversion process

980nm+1550nm -> 598nm at room temperature (t=25˚C)

As mentioned in [35], fabrication errors of the periodically poled structure, such as random duty cycle (RDC) errors, can result in an extension up to hundreds of nanometers from the phase-matching peak. We now investigate how to deduce the average standard deviation of domain period.

The phase matching curve is a function of both the signal wavelength λ_s and domain period d:

$$Y(\lambda_s,\Lambda)=C\frac{\sin^2[\Delta k(\lambda_s,\Lambda)L/2]}{[\Delta k(\lambda_s,\Lambda)L/2]^2} \tag{2.23}$$

where:

$$\Delta k(\lambda_s,\Lambda)=\frac{2\pi n_u}{\lambda_u}-\frac{2\pi n_p}{\lambda_p}-\frac{2\pi n_s}{\lambda_s}-\frac{2\pi}{\Lambda} \tag{2.24}$$

To find out the expected phase matching curve for some certain domain period distribution $f(\Lambda)$, the following expression is used:

$$\bar{Y}(\lambda_s)=\frac{\int_{-\infty}^{+\infty} f(\Lambda)Y(\lambda_s,\Lambda)\,\mathrm{d}\Lambda}{\int_{-\infty}^{+\infty} f(\Lambda)\,\mathrm{d}\Lambda} \tag{2.25}$$

Here we assume the probability density function (*pdf*) to be a standardized Normal Distribution:

$$f(\Lambda)=\frac{1}{\sigma\sqrt{2\pi}}\exp[-\frac{(\Lambda-\mu)^2}{2\sigma^2}] \tag{2.26}$$

μ=mean value of domain period, σ=standard deviation of domain period. Since it is a standardized *pdf*, the integration in the denominator:

$$\int_{-\infty}^{+\infty} f(\Lambda)\,\mathrm{d}\Lambda=1 \tag{2.27}$$

So finally:

$$\bar{Y}(\lambda_s) = \int_{-\infty}^{+\infty} f(\Lambda) Y(\lambda_s, \Lambda) \, \mathrm{d}\Lambda \tag{2.28}$$

Simulations are shown below:

μ=10.16μm

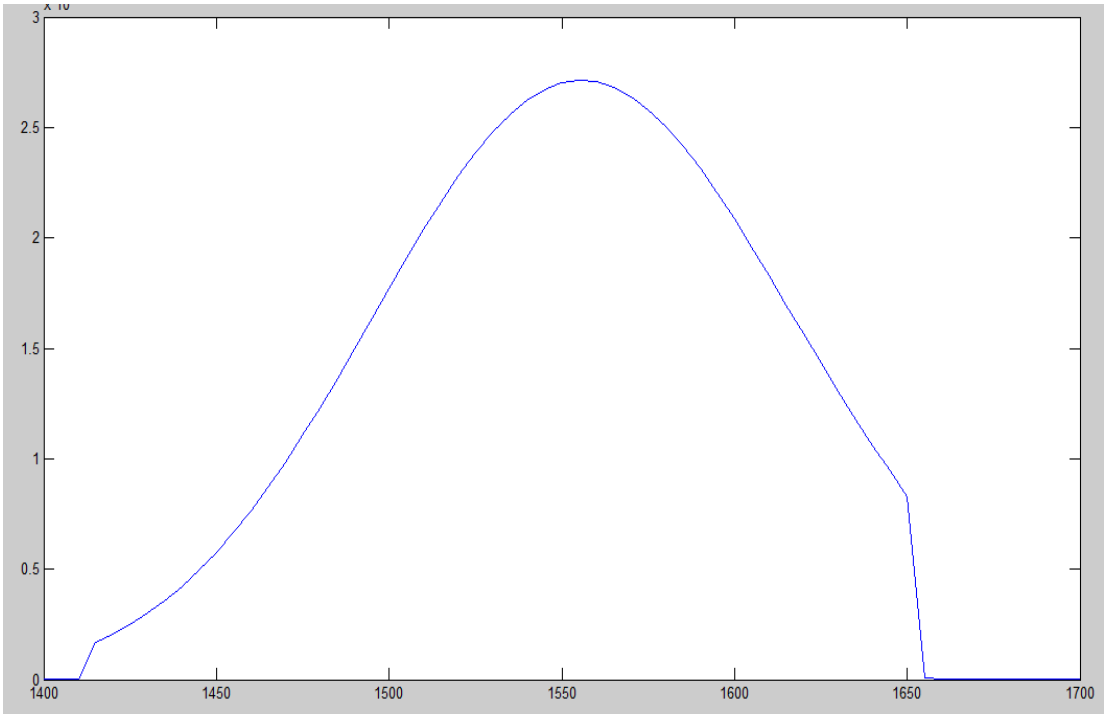

Fig. 2.16 (a) Simulation of phase-matching curve with σ=0.1* μ=1.016 μm

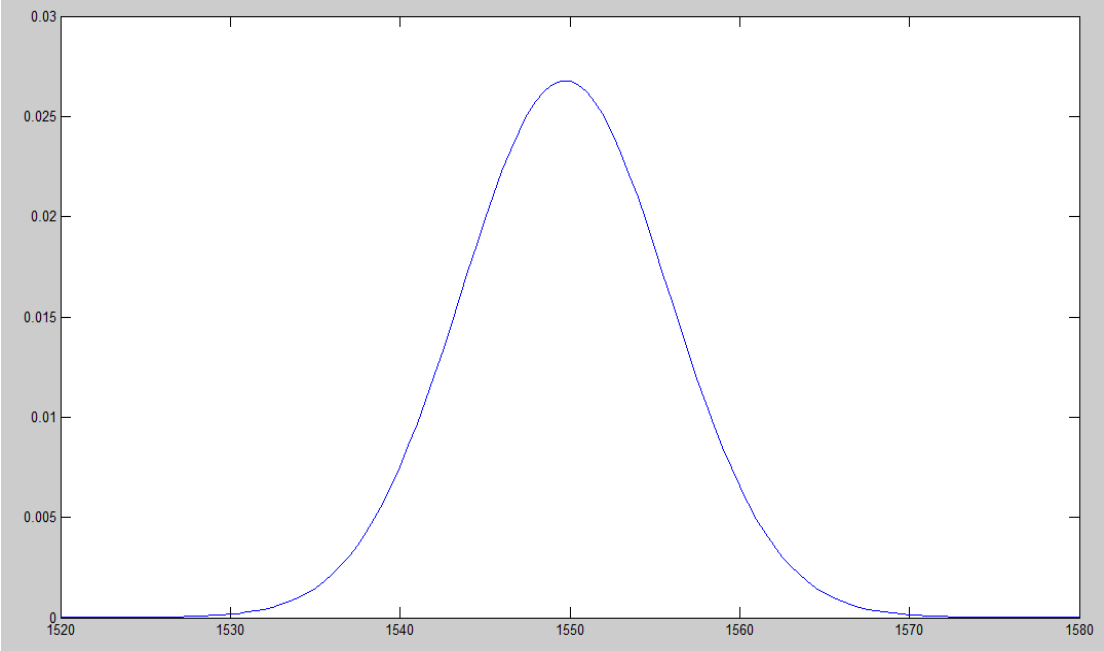

Fig. 2.16 (b) Simulation of phase-matching curve with σ=0.01* μ=0.1016 μm

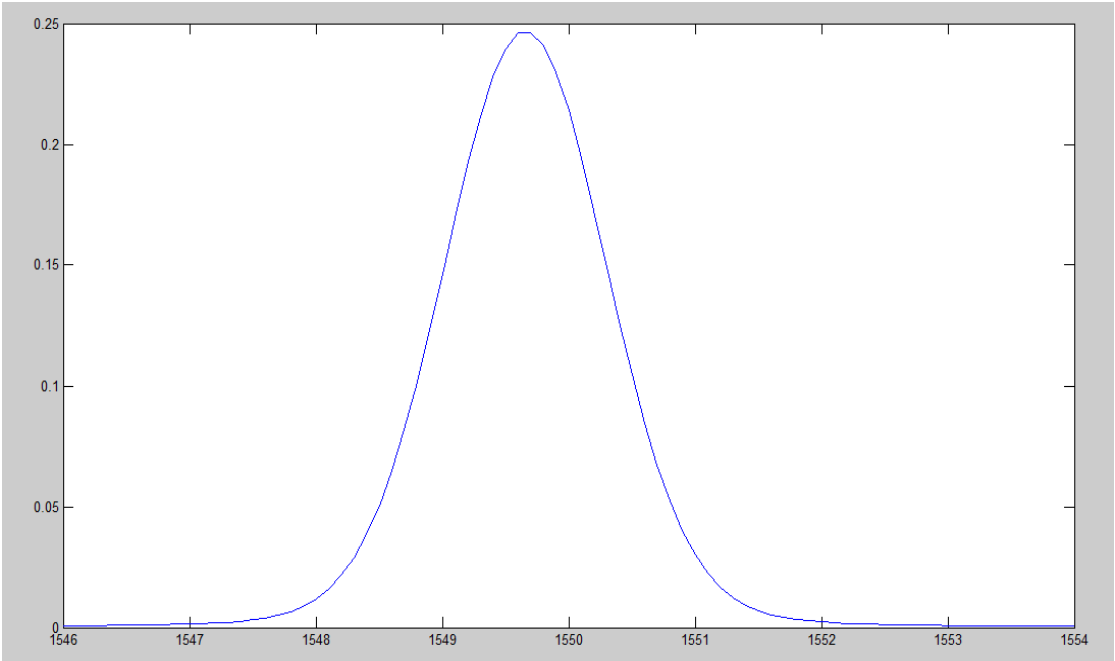

Fig. 2.16 (c) Simulation of phase-matching curve with σ=0.001* μ=10.16 nm

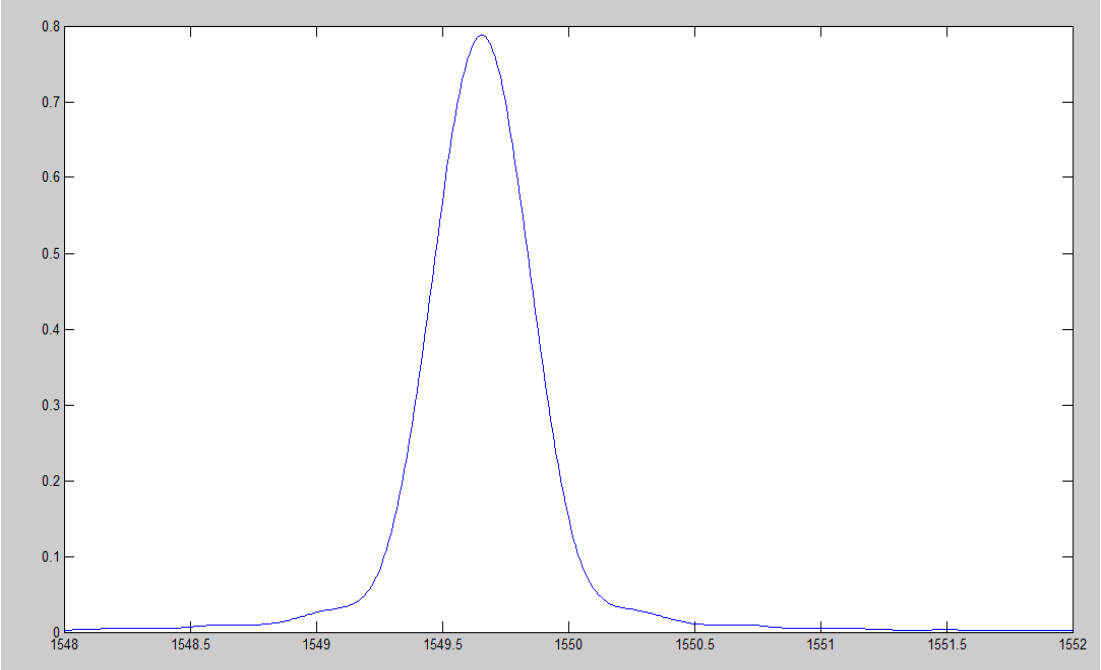

Fig. 2.16 (d) Simulation of phase-matching curve with σ=0.0001* μ=1.016 nm

Compare the bandwidth of the phase-matching curve we measured (0.357 nm) in the actual experiment with simulations in Fig. 2.16 (a)-(d), we deduced that the average standard deviation (STD) of domain period to be 0.02%, i.e. σ=0.02%l, where $l=\Lambda_G/2$=5.08μm. Such an STD value would modify the total noise photon generation rate to be 294.42cps and a detected rate to be 77.43cps. It is true that randomness of domain period will increase the photon numbers in the parametric down-conversion process. However, the random distribution of domain lengths will drastically decrease the subsequent up-conversion process and as a result, the noise SFG photons will decrease essentially. This theoretical value is quite close to our observation and therefore supports our experimental findings.

2.6 Novel method: Frequency upconversion in GaP plate

III-V semiconductors exhibit large second-order nonlinear coefficients [40]. For example, for a gallium phosphide (GaP) crystal, one of the element of the second-order nonlinear susceptibility tensor, i.e. d_{14}, can be as large as 100 pm/V [40]. This value is about three times greater than d_{33} for lithium niobate, which has been considered as one of the most widely used efficient nonlinear crystals for single photon detection at the communication band based on frequency upconversion [14, 20, 33]. The high nonlinearity and wide transparent range of GaP in infrared (0.5-11 μm) and THz regions makes it attractive for achieving efficient frequency conversion [41]. Moreover, GaP is free from photorefractive effect which can be detrimental in frequency conversion, limiting conversion efficiency and causing permanent damage [42].

However, due to the cubic symmetry of the zincblende lattice, GaP has no birefringence. Therefore, phase matching is not possible. As a result, GaP has not been considered as an efficient nonlinear material for frequency conversion in the past. By periodically inverted <111> direction of the GaP plates in a stack, efficient conversion can be achieved in the THz region based on quasi-phase-matching [41]. However, in the infrared region, such a scheme is difficult to realize since the required thickness is too thin in order to satisfy the quasi-phase-matching condition. Recently, enhanced sum-frequency generation in doubly resonant GaP photonic crystal nanocavities was demonstrated [43]. However, for practical applications an alternative scheme must be utilized. It is worth noting that total-internal-reflection quasi-phase-matching (TIR-QPM)

can be used to enhance the efficiency of frequency conversion. In such a scheme, each TIR induces a phase shift, which can be exploited to compensate the phase mismatch for nonlinear frequency conversion [44,45].

Here, we report our results of achieving frequency up-conversion in a GaP plate, i.e. up-converting the incoming photons within the communication band to those within the visible band.

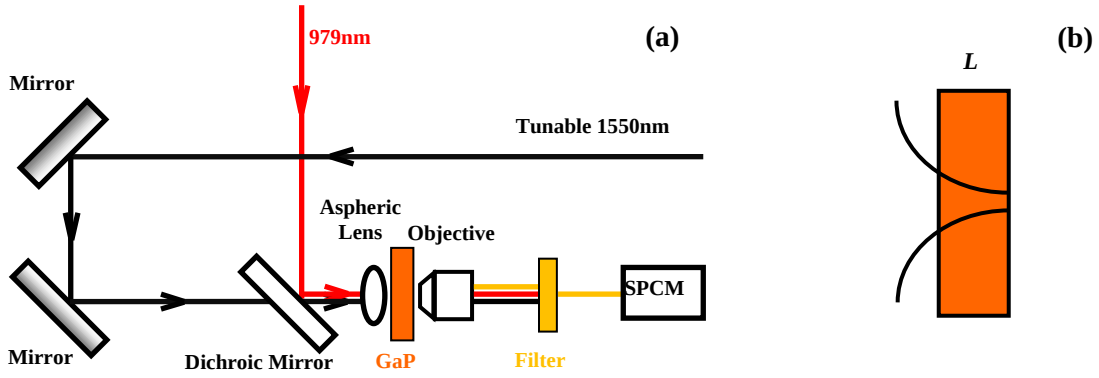

Fig. 2.17. (a) Experimental setup. (b) Input signal within the communication band and pump beam at 979 nm were focused by an aspheric lens on to a GaP plate with the beam waists being located at the exit facet of the GaP crystal with its length of $L \approx 663$ μm.

As shown in Fig. 2.17 (a), a CW C-band semiconductor laser (Agilent) with its output wavelength tunable from 1.48 μm to 1.58μm is used as the input signal. It was combined with a pump diode laser at the wavelength of 979 nm by a dichroic mirror. The two beams were focused by an aspheric lens having the focal length of 5 mm (Thorlabs). The

beam diameter measured at its waist is about 4 μm. A pinhole was placed in the beam path to ensure that both pump and signal beams saptially overlap at the focal plane which is located at the exit facet of the crystal, see Fig. 2.17 (b). The undoped GaP plate was used for achieving upconversion. The thickness of the crystal is 663 μm. The upconverted output generated via sum-frequency generation (SFG) was subsequently collected by a 40× objective. After passing through a set of optical filters, the sum-frequency was coupled into the single photon counting module (Perkin Elmer). It has a dark count rate of 25 s^{-1}.

To ensure the recorded counts originate from SFG rather than noise photons from the pump source or from ambient air, we turned off both the laser sources, turned on only the pump, and turned on only the input signal only. For these three cases, we took the average of the signal output from the single photon counting module for 200 times. The average signals from the counter were measured to be 27 s^{-1}, 29 s^{-1} and 26 s^{-1}, respectively. Since these count rates are essentially the same as the dark count rate of the counter, any count rates above these levels originate from upconversion. We subsequently measured the pump power dependence, i.e. the upconverted photon counter rate as a function of the pump power when the incident power of the C-band source was set to 2 mW. As shown in Fig. 2.18, the power dependence curve demonstrated good linearity, which is consistent with our theory. We would like to note that the coherent length of the SFG process can be calculated to be about 3 μm, which is much shorter than the crystal thickness (663 μm). Therefore, only a small portion of the GaP crystal effectively contributed to the power conversion for SFG. Since the conversion efficiency

was relatively low, depletion of the input signal is negligible. The maximum count rate we have achieved in our experiment was 10000 s^{-1} under the pump power of 250 mW. The normalized conversion efficiency is determined to be about 100%/(kW·cm^2), which is much higher than that for $LiNbO_3$. As we tuned the input signal wavelength, the upconverted output power exhibited oscillations, see Fig. 2.19. This is due to the fact that the coherence length oscillates as the input wavelength is increased, similar to the behavior in CdSe [46].

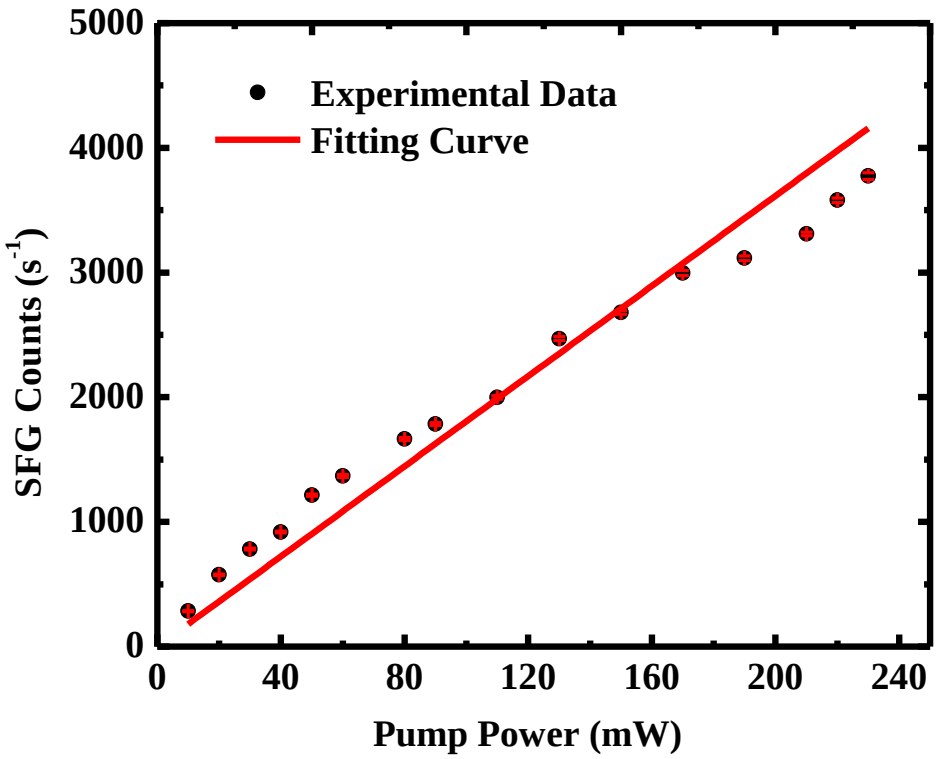

Fig. 2.18 Pump power dependence for SFG

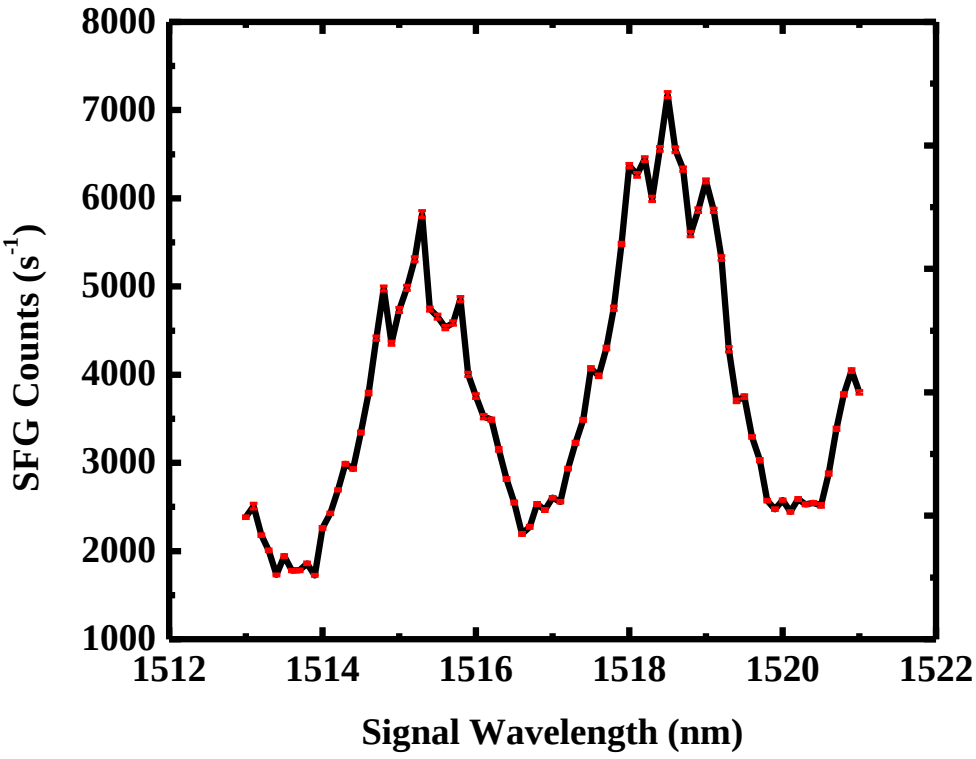

Fig. 2.19 Up-converted signal intensity vs. input signal wavelength.

To further improve the conversion efficiency for the upconversion, we can exploit TIR-QPM [44]. Generally speaking, the sum frequency generation for total internal reflection assisted quasi-phase matching is governed by the following equation:

$$I_3 = \frac{8\pi^2 d_{eff}^2}{n_1 n_2 n_3 \lambda_1 \lambda_2 c \varepsilon_0} I_1 I_2 L^2 [\frac{\sin(\Delta kL/2)}{\Delta kL/2}]^2 [\frac{\sin(N\varepsilon/2)}{\sin(\varepsilon/2)}]^2 \quad (2.29)$$

To maximize the above equation, we need to maximize the product of the last two brackets:

$$[\frac{\sin(\Delta kL/2)}{\Delta k/2}]^2[\frac{\sin(N\varepsilon/2)}{\varepsilon/2}]^2 \tag{2.30}$$

where $\varepsilon = \Delta kL + \Delta\phi + \phi_s - 2\pi M$. $\Delta\phi = \phi_3 - \phi_2 - \phi_1$. ϕ_s is either 0 or π, depending on the incident waves geometry and combination, e.g. pps or sss.

In isotropic crystals like GaP, it is not generally possible to make Δk =0 where the first bracket reaches its maximum for a given set of wavelengths. However we can make $\sin(\Delta kL/2) = 1$. This requires $\Delta kL = (2N+1)\pi$. The second term reaches its maximum at $\varepsilon = 0$ and this time, we can achieve the goal with the help of phase shift upon total internal reflection.

For TE wave: (s wave or σ wave), it's phase shift upon TIR as regard to TIR angle is shown below:

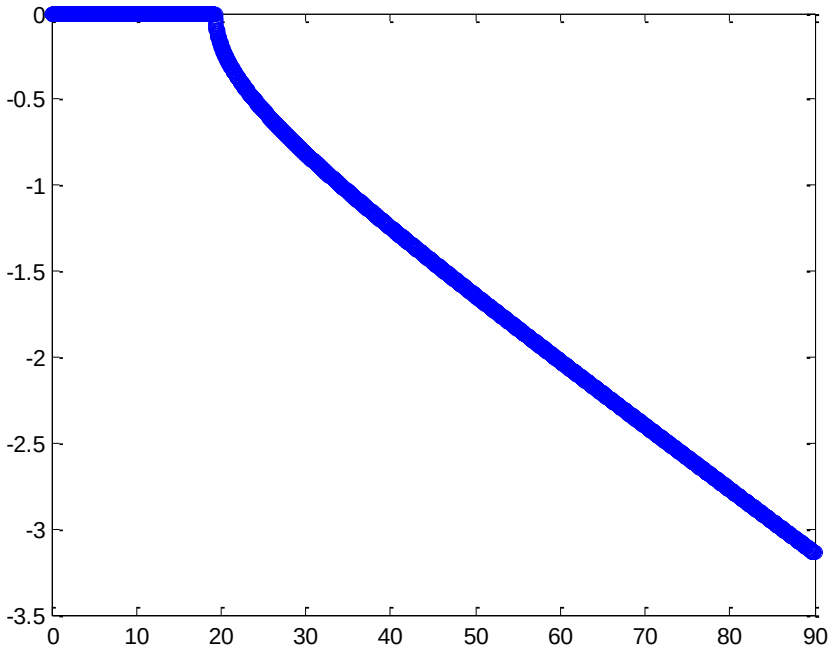

Fig. 2.20 Phase shift for TE-wave with respect to incident angle

And for TM wave (p wave, π wave):

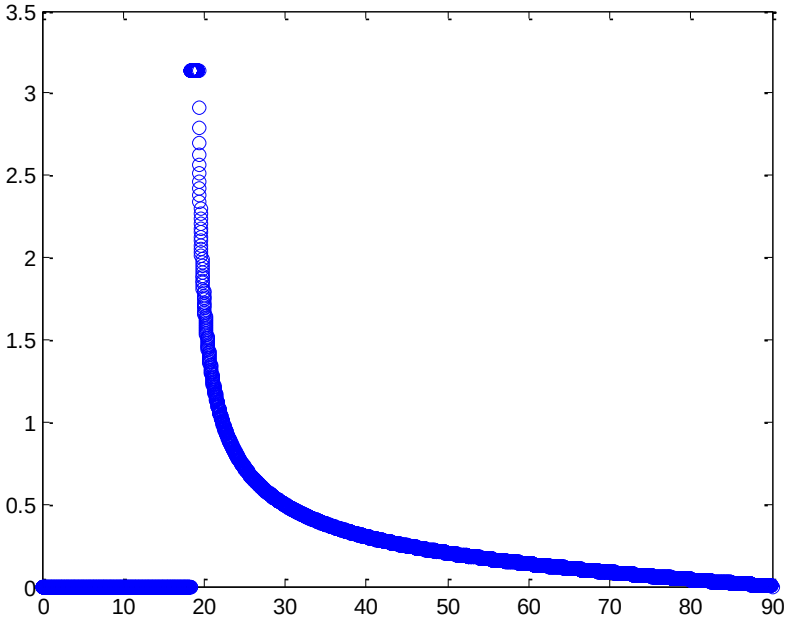

Fig. 2.21 Phase-shift for TM-wave with respect to incident angle

The expressions for the phase shift are:

$$TE\begin{cases} 0 & \theta < \theta_c \\ -2\tan^{-1}\left(\dfrac{\sqrt{n^2\sin^2\theta_i - 1}}{n\cos\theta_i}\right) & \theta > \theta_c \end{cases} \tag{2.31}$$

$$TM\begin{cases} 0 & \theta < \theta_B \\ \pi & \theta_B < \theta < \theta_c \\ \pi - 2\tan^{-1}\left(\dfrac{\sqrt{n^2\sin^2\theta_i - 1}}{\cos\theta_i}\right) & \theta > \theta_c \end{cases} \tag{2.32}$$

A summary for ϕ_s with regard to combinations of beam polarization is shown below:

sss	ssp	sps	spp	pss	psp	pps	ppp
0	π	π	0	π	0	0	π

sss	ssp	sps	spp	pss	psp	pps	Ppp
π	0	0	π	0	π	π	0

Table 2.2 Phase-shift with respect to different beam polarization combination

Therefore, to fulfill $\varepsilon = 0$, $\Delta\phi$ will need to satisfy the following conditions (note that $\Delta kL = (2N+1)\pi$):

By plotting $\Delta\phi$ against incident total reflection angles, we found that only pps combination resulted in a valid incident angle:

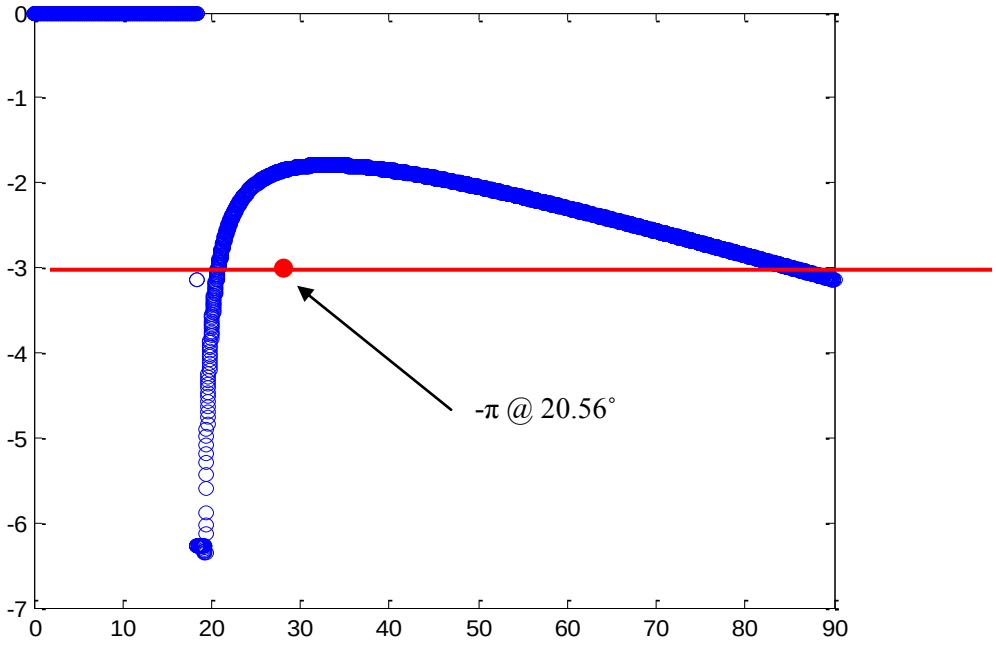

Fig. 2.22 Incident angle that maximize Eq. 2(.30)

From Fig. 2.22 we see that at internal incident angle of 20.56˚, the phase shift reaches –π and compensates the phase mismatch caused by normal dispersion.

From above calculation, we see that when each leg of the zigzag path in the crystal plate is an odd integer multiple of the coherent length, the net phase shift on each TIR bounce can result in the accumulative growth of the generated field [44], thus enhancing the up-converted signal intensity. At the input signal wavelength of 1550 nm, we have calculated the incident angle to be θ = 20.56°. The required plate thickness t can be determined from $t/\cos\theta = (2N+1)L_c$, where N is an integer and L_c is the coherence length. GaP-based devices have potential to be utilized in single photon detection as an alternative to lithium niobate based devices.

2.7 Conclusion for Chapter 2

Commercially available detectors at IR wavelengths suffer from several drawbacks. InGaAs/InP avalanche photodiodes (APDs) are commonly used. They have high dark counts up to 10^5/s, as well as low quantum detection efficiencies, usually with values between 10% and 15%. Their long dead-time will cap the detection rate to no more than 400 kHz. In contrast, single-photon counting in near-IR (600-800nm) can be performed efficiently with silicon APDs. Single photon counting modules with dark counts lower than 25/s and detection efficiency in the range 50% to 70% are commercially available. We can take advantage of silicon APDs if efficient conversion from C-band to near-IR can be realized. In our experiment, we have implemented single photon detection in periodically poled lithium niobate waveguide with 980nm pump, with negligible noise photon counts. We then theoretically investigated the generation of noise counts by considering both perfect and imperfect grating structures for lithium niobate. The key is that for a given grating period, the gain peak for spontaneous parametric down-conversion process and the gain peak for designed up-conversion process usually do not overlap, resulting in intrinsic low noise photon generation. The simulation agreed well with our experimental results. At last, we explored GaP as an alternative second-order nonlinear material to implement single photon detection. Experimental results have been demonstrated and we investigated total-internal-reflection assisted phase-matching in GaP plate, where by other means perfect phase match cannot be achieved.

Chapter 3

Evaluation of domain quality in periodically poled structure with non-destructive method

3.1 Historical review

Periodically-poled lithium niobate (PPLN) waveguide is an efficient nonlinear structure for generation of tunable coherent radiation based on optical parametric oscillators [20] and single-photon detection based on frequency up-conversion [33]. In order to achieve efficient conversion, quasi-phase-matching (QPM) must be satisfied. However, imperfections of periodic domains due to fabrication errors such as *linear taper* of domain period, *duty cycle* error, and *randomness* of domain period [35] significantly affect the performance of the PPLN waveguide. When a bulk PPLN crystal under an electric field was illuminated with a laser, domain quality [47] and duty cycle randomness [48,49] were studied by analyzing far-field diffraction patterns. However, these optical techniques suffer from poor spatial resolutions on the order of 10 μm. For reaching a higher resolution, surface treatment techniques must be employed. However, these techniques are destructive. There is no effective technique for evaluating domains within PPLN waveguides.

Here, we demonstrate that surface-emitting second-harmonic generation is indeed an effective technique for evaluating the domain quality of a PPLN waveguide.

3.2 Experimental setup and results

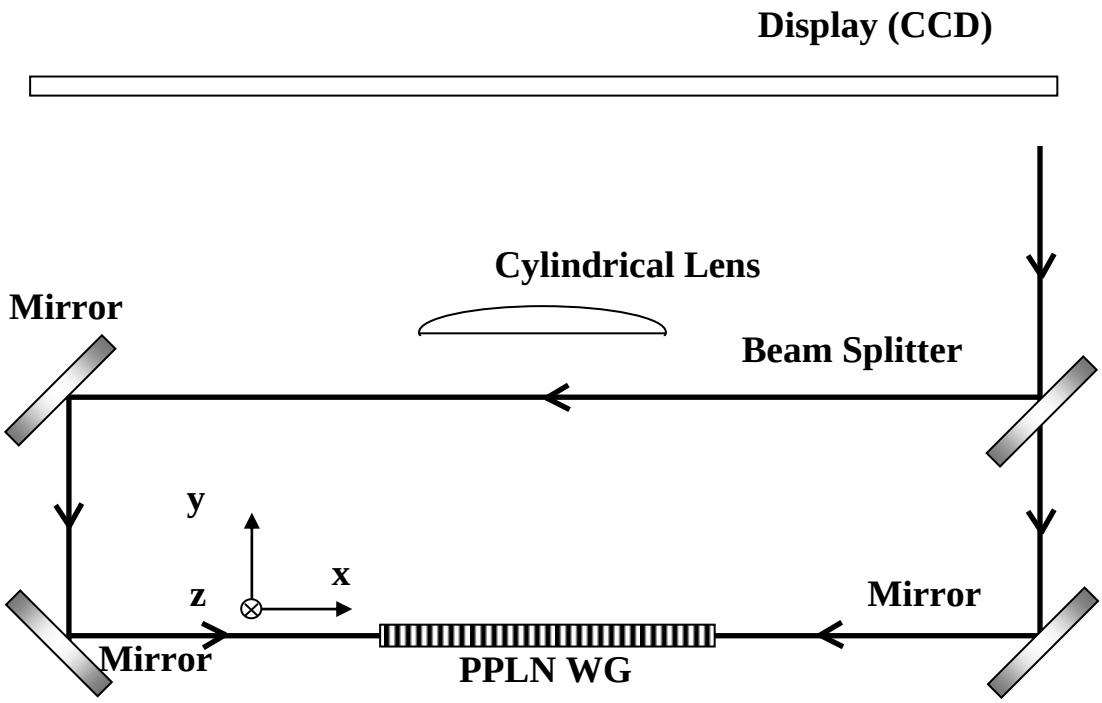

Fig. 3.1 Experimental setup for measuring far-field SH pattern

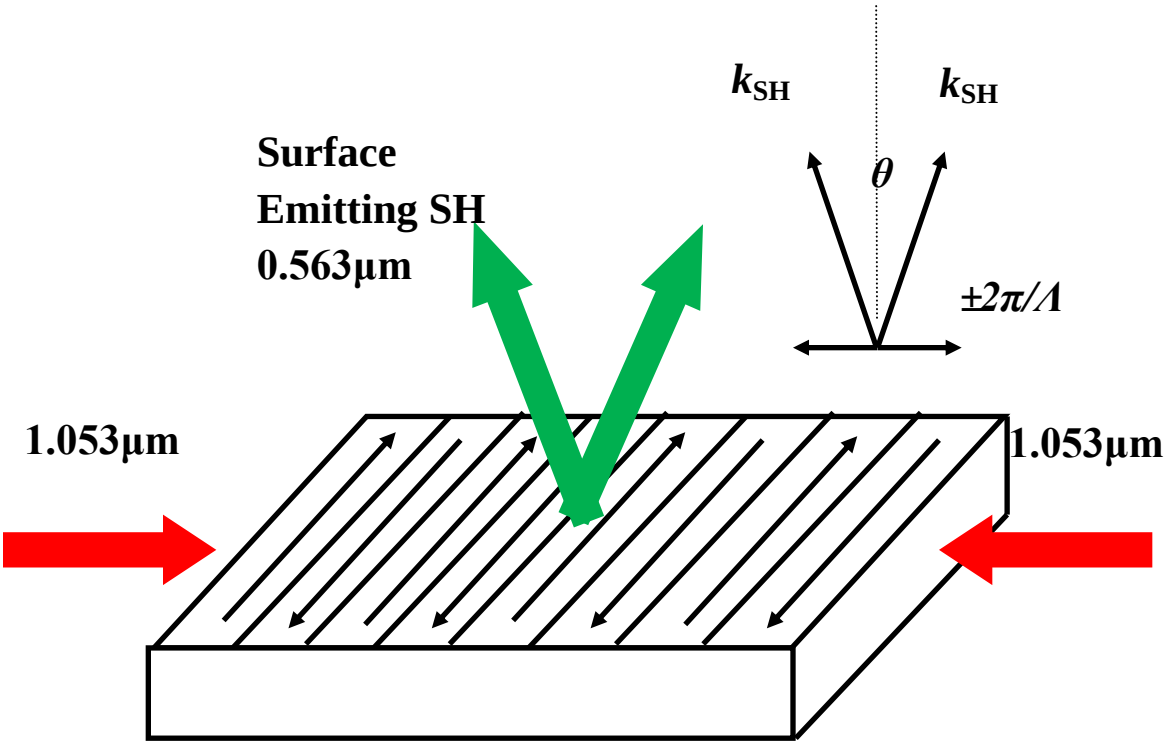

Fig. 3.2 Surface-emitting second harmonic generation satisfying condition of k_{SH} $\sin\theta = \pm 2\pi/\Lambda$

In our experiment, a compact and portable Nd:YLF laser was used as a pump beam for investigating the surface-emitting second-harmonic generation (SHG), see Fig. 1(a). The pump spectrum centered at 1.053 μm had a linewidth of 0.5 nm (135 GHz). An acoustic-optic *Q*-switch was used to modulate the pump beam at the repetition rate of 5 kHz. The pulse width of the laser was 10 ns. The beam was split by a 50/50 beam splitter and coupled into the PPLN waveguide using aspheric lenses. The *y*-propagating surface-emitting SH beam was focused along z direction by a cylindrical lens to avoid divergence due to a 6-μm-wide waveguide. The final spatial profile of the SH beam was observed directly on a white screen being placed at a distance of 1 m away from the waveguide. It was also imaged by a CCD beam profiler.

3.3 Theory

Under an ideal condition, the counter-propagating pump beams having exactly the same wave vector generate uniform surface-emitting SH beams [50] with their wave-vector component along x direction being equal to $\pm 2\pi/\Lambda$, where Λ is the domain period of the QPM grating. The SH beam emitting from the waveguide surface is refracted by $LiNbO_3$, resulting in a relation given by $\sin\theta=\lambda/\Lambda$, where θ is the emitting angle of the SH beam (Fig. 3.2) and λ is the SH wavelength. The 1-D spatial profile, $F_z(x)$, is given by

$$F_z(x) = \left| f_z(x) \right|^2 = \left| \frac{\exp(ikz)}{\sqrt{i\lambda z}} \exp(i\frac{kx^2}{2z}) \int_{-\infty}^{+\infty} f_0(x_0) \exp(i\frac{kx_0^{\,2}}{2z}) \exp(-i\frac{kxx_0}{\lambda z}) dx_0 \right|^2 \qquad (3.1)$$

where k is the wave vector of the SH, z is the distance from waveguide chip to the projection screen, λ is the SH wavelength, x_0 is the coordinates on the waveguide, and $f_0(x_0)$ is the waveguide pupil function whose value alternating between 1/2 and -1/2 at the opposite domains. In the actual experiment, the distance z=1.06m, which was far more less than the critical distance $z_{critical}=z^2/\lambda$=1711m. Therefore, the term $\exp(ikx_0^{\,2}/2z)$ cannot be neglected. Thus the projected spatial profile was not simply the Fourier transfer of the pupil function $f_0(x_0)$. In other words, it was not *Fraunhofer* diffraction. As can be seen from Eq. (3.1), the SH spatial profile projected on the screen depend heavily on the QPM grating pupil function $f_0(x_0)$, i.e. the SH spatial profile contains direct information of the grating shape. By substituting different $f_0(x_0)$ into Eq. (3.1), we are able to obtain corresponding SH far-field spatial profile. We then analyze our experimental results and

compare with theoretical values to unveil the actual waveguide pupil function.

The expression for $F_z(x)$ can be readily extended to 2-D case by integrating the y_0 coordinate. However, since the SH intensity remained constant along y_0 direction, the integral would simply be a constant and would impose no impact on the lateral spatial profile projected on the screen plane. Therefore, in the following sections we will only consider 1-D cases.

3.3.1 Perfect QPM grating

We first consider the ideal case, i.e. the domain width $w=\Lambda_0/2$ and keeps a constant. The optical axis polarization in adjacent domains alternate accordingly. We number the central two domains of the waveguide with integer m=0 and mark them as benchmark. We then number those domains left to the benchmark with negative integers (m=-1, -2…) and those right to the benchmark with positive integers (m=1, 2…), as illustrated in Fig. 2. We assume that the whole waveguide has $2N+1$ domain periods. For the actual waveguide we were using, N=1500.

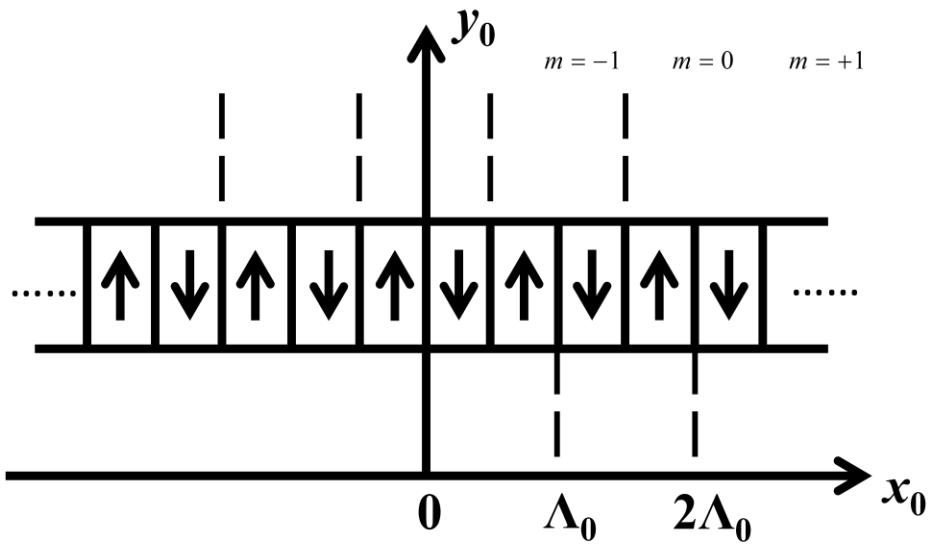

Fig 3.3 Perfect domain in periodically poled structure

Following notations defined above, the waveguide pupil function, $f_0(x_0)$, at the mth period, can be expressed explicitly as:

$$f_{0,m}(x_0)=\begin{cases}\dfrac{1}{2}, & m\Lambda_0 \le x_0 \le m\Lambda_0+\dfrac{1}{2}\Lambda_0\\ -\dfrac{1}{2}, & m\Lambda_0-\dfrac{1}{2}\Lambda_0 < x_0 < m\Lambda_0\end{cases} \tag{3.2}$$

Substituting the expression of $f_{0,m}(x_0)$ into Eq. (1), we obtain the far-field integral for mth domain:

$$f_{z,m}(x)=\frac{\exp(ikz)}{\sqrt{i\lambda z}}\exp(i\frac{kx^2}{2z})\{\int_{m\Lambda_0}^{m\Lambda_0+\frac{\Lambda_0}{2}}(\frac{1}{2})\exp(i\frac{kx_0^2}{2z})\exp(-i2\pi\frac{x}{\lambda z}x_0)dx_0+\int_{m\Lambda_0-\frac{\Lambda_0}{2}}^{m\Lambda_0}(\frac{-1}{2})\exp(i\frac{kx_0^2}{2z})\exp(-i2\pi\frac{x}{\lambda z}x_0)dx_0\}$$

$$=\frac{\exp(ikz)}{\sqrt{i\lambda z}}(-\frac{i\sqrt{\pi}}{2\sqrt{\frac{ik}{2z}}})\{\frac{1}{2}erfz[\sqrt{\frac{i^3k}{2z}}(m\Lambda_0+\frac{\Lambda_0}{2}-x)]-erfz[\sqrt{\frac{i^3k}{2z}}(m\Lambda_0-x)]+\frac{1}{2}erfz[\sqrt{\frac{i^3k}{2z}}(m\Lambda_0-\frac{\Lambda_0}{2}-x)]\}$$

(3.3)

Here, x_0 is the coordinate on the waveguide surface, and x is the coordinate on the projection plane. *erfz*(x) is known as the *error function* with complex arguments, which is usually discussed in scaled form as the *Faddeeva function* [51].

The total far-field integral can now be obtained by summarizing domain period number m from $-N$ to N:

$$f_z(x)=A\bullet\{\frac{1}{2}g(N+\frac{1}{2})+\frac{1}{2}g(-N-\frac{1}{2})+\sum_{p=-N}^{N}g(p+\frac{1}{2})-\sum_{p=-N}^{N}g(p)\} \tag{3.4}$$

where

$$A = -\frac{i\sqrt{\pi}}{2\sqrt{\frac{ik}{2z}}}\frac{\exp(ikz)}{\sqrt{i\lambda z}}, \qquad g(m) = erfz[\sqrt{\frac{i^3 k}{2z}}(m\Lambda_0 - x)] \tag{3.5}$$

Finally, the 1-D spatial profile is given by:

$$F_z(x) = \left| f_z(x) \right|^2 \tag{3.6}$$

and is numerically calculated. The simulation curve is shown in Fig. 3.4, for N=1500.

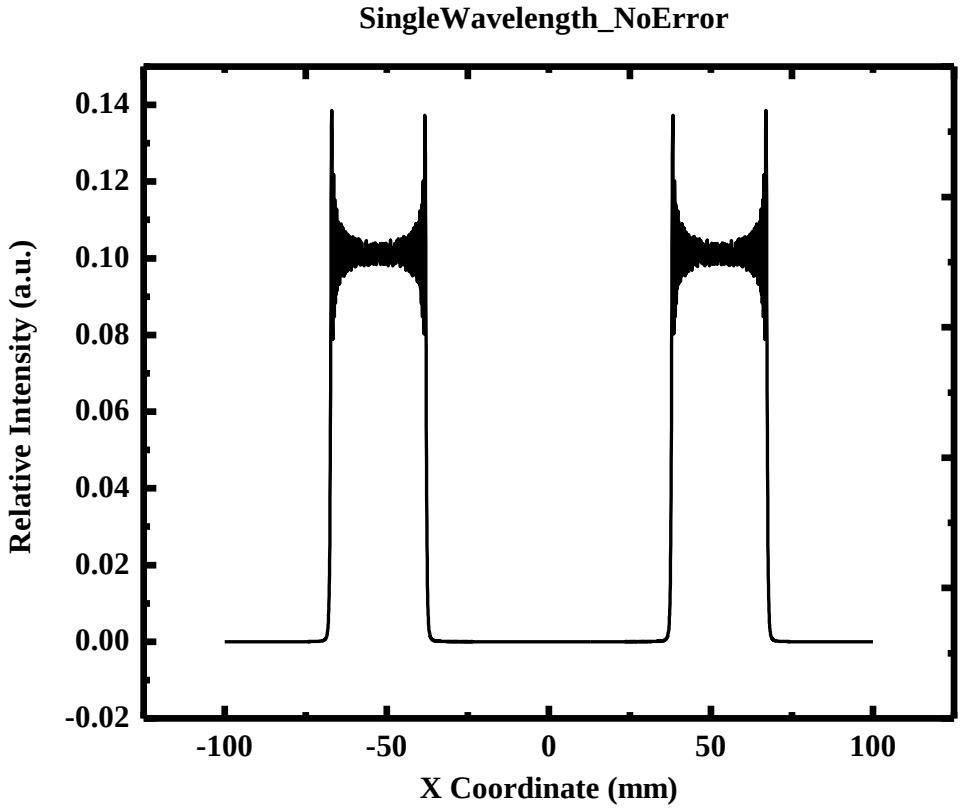

Fig. 3.4 1-D Simulation with no domain error

As illustrated in the figures, there existed two peaks centered at ±53.95mm, which agreed with the theoretically predicted value at $x_{1,2}=\pm\lambda z/\Lambda_0$. The width of each peak was 29.6mm, very close to the actual waveguide length.

3.3.2 QPM grating with linear taper

In the growth of a periodically poled lithium niobate crystal, a drift in the poling period would occur along the length of a sample due to drift in the crystal pull rate or in the modulation frequency of the boundary positions. [35]. We can then define a linear taper coefficient $c_t=(l_N-l_1)/2N$, where l_N and l_1 are the domain widths of the last and first period, and N is the period number, see Fig. 3.5.

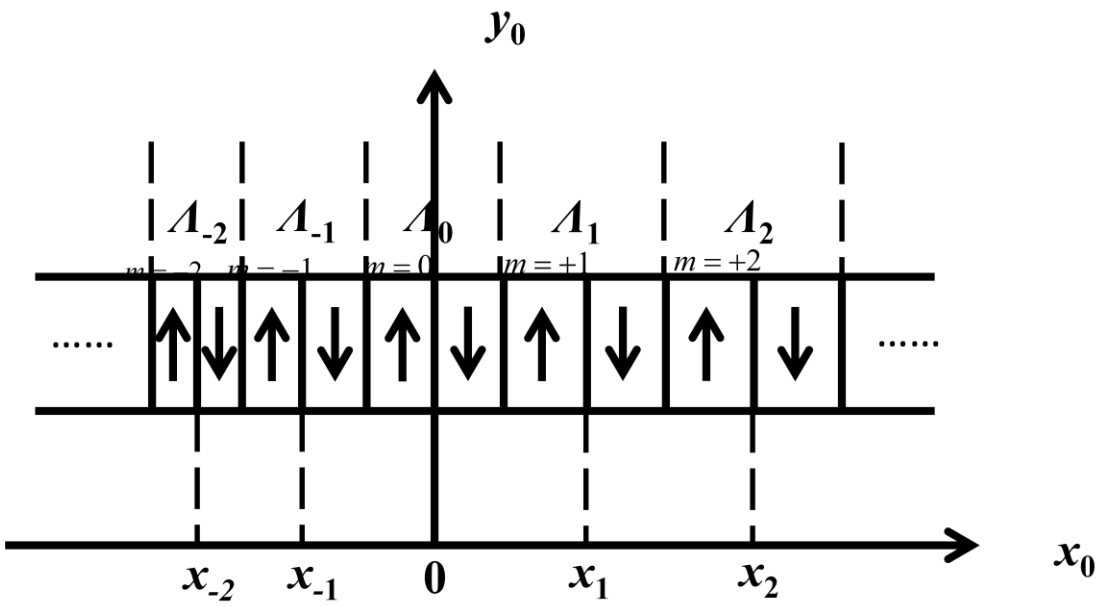

Fig. 3.5 Domain period with linear taper

We still assume that the waveguide has $2N+1$ periods, from $m=-N$ to $m=N$. Since each domain period length varies, we now assume the period with notation number m=0 has the "correct" length, Λ_0. We may now write domain length for the mth period:

$$\Lambda_m = \Lambda_0 + mc_t \tag{3.7}$$

And the central coordinate for each period is given by:

$$x_m = m\Lambda_0 + \frac{m^2}{2} c_t \tag{3.8}$$

Following notations defined above, the waveguide pupil function, $f_0(x_0)$, at the mth period, can be expressed explicitly as:

$$f_{0,m}(x_0) = \begin{cases} \frac{1}{2}, & (x_m \le x_0 \le x_m + \frac{1}{2}\Lambda_m) \\ -\frac{1}{2}, & (x_m - \frac{1}{2}\Lambda_m < x_0 < x_m) \end{cases} \tag{3.9}$$

Similar integration to Eq. (3) was performed:

$$f_{z,m}(x) = \frac{\exp(ikz)}{\sqrt{i\lambda z}}\left(-\frac{i\sqrt{\pi}}{2\sqrt{\frac{ik}{2z}}}\right)\left\{\frac{1}{2} erfz\left[\sqrt{\frac{i^3 k}{2z}}\left(x_m + \frac{\Lambda_m}{2} - x\right)\right] - erfz\left[\sqrt{\frac{i^3 k}{2z}}(x_m - x)\right] + \frac{1}{2} erfz\left[\sqrt{\frac{i^3 k}{2z}}\left(x_m - \frac{\Lambda_m}{2} - x\right)\right]\right\}$$

(3.10)

The final 1-D spatial far-field profile can now be obtained as:

$$F_z(x) = |A|^2 \bullet \left| \left\{\frac{1}{2} erfz\left[\sqrt{\frac{i^3 k}{2z}}\left(x_N + \frac{\Lambda_N}{2} - x\right)\right] + \frac{1}{2} erfz\left[\sqrt{\frac{i^3 k}{2z}}\left(x_{-N} - \frac{\Lambda_{-N}}{2} - x\right)\right] + \sum_{m=-N}^{N} erfz\left[\sqrt{\frac{i^3 k}{2z}}\left(x_m + \frac{\Lambda_m}{2} - x\right)\right] - \sum_{m=-N}^{N} erfz\left[\sqrt{\frac{i^3 k}{2z}}(x_m - x)\right]\right\} \right|^2$$

(3.11)

The corresponding simulation curves are demonstrated in Fig. 3.6, for N=1500 against various linear taper coefficient values from c_t=1Å/period to c_t=9Å/period.

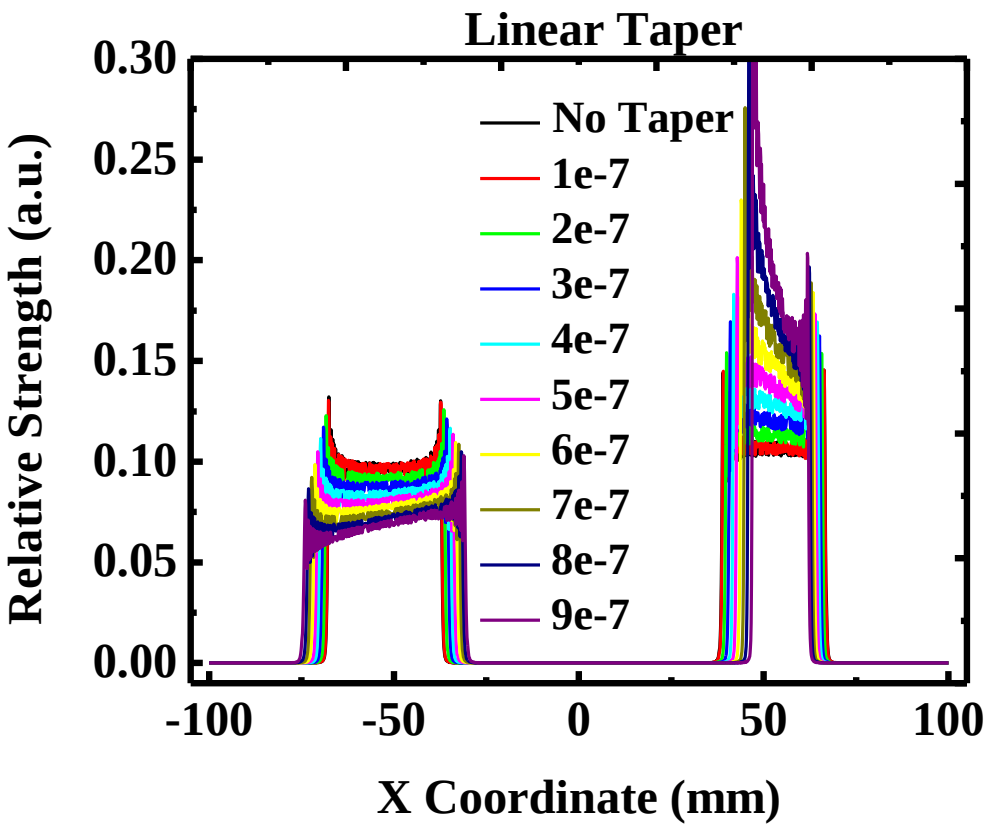

Fig. 3.6 Simulated far-field SHG patterns for domain period with linear taper error

As it can be seen from Fig. 3.6, the larger the linear taper coefficient, the larger the pattern distortion, and the wider of widths of the two legs.

3.3.3 QPM grating with periodic errors in boundary position

Due to oscillation in the positions of the freezing boundary during growth of a periodically poled crystal, a periodic domain drift in the position of the boundaries would occur [35]. Such domain period defect can be modeled with the following equation:

$$x_m = m\Lambda_0 + \eta\Lambda_0 \sin(\Omega m\Lambda_0) \tag{3.12}$$

In Eq. (3.12), we notice that the first term, $m\Lambda_0$, is considered as the equivalent position for each domain boundaries. The second term can be viewed as a perturbation imposed on the "ideal" situation. η is the relative amplitude of the perturbation, and Ω is the oscillation frequency. Since it is obvious that:

$$x_m - x_{m-1} = (\Lambda_m + \Lambda_{m-1})/2 \tag{3.13}$$

We can deduce the expression for Λ_m:

$$\Lambda_m = \begin{cases} \Lambda_0 + 2\eta\Lambda_0[\sin(m\Omega\Lambda_0) + 2\sum_{p=1}^{m-1}(-1)^{m-p}\sin(p\Omega\Lambda_0)] & (m \geq 2) \\ \Lambda_0 + 2\eta\Lambda_0 \sin(\Omega\Lambda_0) & (m = 1) \\ \Lambda_0 & (m = 0) \\ \Lambda_{-m} & (m \leq -1) \end{cases} \tag{3.14}$$

We plug the expression for x_m and Λ_m into Eq. (3.11) and get the following simulation curve for this case:

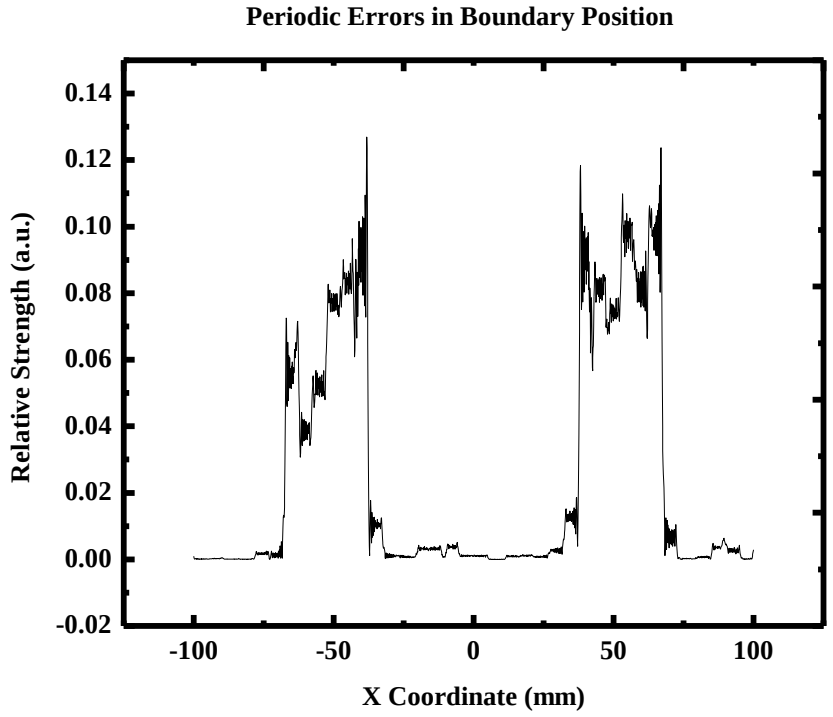

Fig. 3.7 Simulation for domain boundaries with periodical errors, $\eta=0.15$, $\Omega=2\pi/(10\Lambda_0)$

3.3.4 Duty cycle error

In an ideal periodically poled crystal, the direction of optical axis in one complete period is pointing upward for exactly half of the period and downward for the other half of the period. If we consider a rectangular wave of period Λ_0 taking values of $\pm 1/2$, with the positive section of l corresponding to the part of crystal whose optical axis is pointing upward, we can then define *duty cycle* as $a=l/\Lambda_0$. Therefore, the duty cycle for an ideal periodically poled crystal is 0.5. However, in an actual poling process, due to the poling electric field distribution on the crystal, or the mask itself, the duty cycle would deviate from 0.5 and lead to some new features on the far-field spatial profile.

The waveguide pupil function is now modified to:

$$f_{0,m}(x_0)=\begin{cases}\dfrac{1}{2}, & (m\Lambda_0 \le x_0 \le m\Lambda_0+(1-a)\Lambda_m)\\ -\dfrac{1}{2}, & (m\Lambda_0-a\Lambda_0 < x_0 < m\Lambda_0)\end{cases} \tag{3.15}$$

When a=0.5, it reduces to the ideal case.

The far-field integral for the mth period is:

$$f_{z,m}(x)=\frac{\exp(ikz)}{\sqrt{i\lambda z}}\left(-\frac{i\sqrt{\pi}}{2\sqrt{\frac{ik}{2z}}}\right)\left\{\frac{1}{2}erfz\left[\sqrt{\frac{i^3k}{2z}}(m\Lambda_0+(1-a)\Lambda_0-x)\right]-erfz\left[\sqrt{\frac{i^3k}{2z}}(m\Lambda_0-x)\right]+\frac{1}{2}erfz\left[\sqrt{\frac{i^3k}{2z}}(m\Lambda_0-a\Lambda_0-x)\right]\right\}$$

(3.16)

By summing up m from $-N$ to N *(N=50)*, we are able to achieve the simulation curve for duty cycle error:

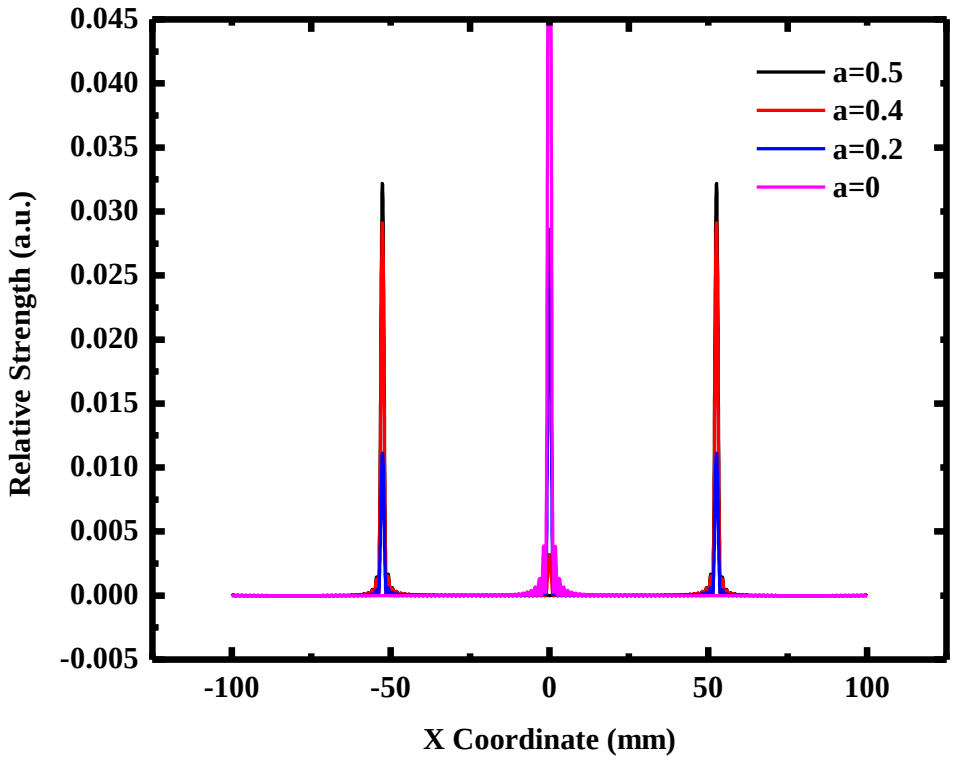

Fig. 3.8 Simulation for domain boundaries with duty cycle errors

When *a*=0, i.e. no periodically poled structure, we would observe only ONE peak at the center. As *a* goes from 0 to 0.5, the side peaks gradually enhance while the center one is suppressed.

3.3.5 QPM grating with random poling period

We now consider a periodically poled structure with random domain period. We assume that the domain periods statistically follow normal distribution, with mean Λ_0 and standard deviation σ, i.e. $\Lambda \sim N(\Lambda_0, \sigma)$. Under such assumption, we can calculate expected values of the spatial profile.

The normalized probability density function for variable Λ (period) can be expressed as:

$$h(\Lambda) = \frac{1}{\sigma\sqrt{2\pi}} \exp[-\frac{(\Lambda - \Lambda_0)^2}{2\sigma^2}] \tag{3.17}$$

It can be observed that $\int_{-\infty}^{+\infty} h(\Lambda) d\Lambda = 1$. The spatial profile function as regard to variable Λ can be written as:

$$F_z(\Lambda) = |A|^2 \bullet \left| \{\frac{1}{2} g(N + \frac{1}{2}) + \frac{1}{2} g(-N - \frac{1}{2}) + \sum_{p=-N}^{N} g(p + \frac{1}{2}) - \sum_{p=-N}^{N} g(p)\} \right|^2 \tag{3.18}$$

where $h(m)$ is defined as:

$$g(m) = erfz[\sqrt{\frac{i^3 k}{2z}} (m\Lambda - x)] \tag{3.19}$$

Finally, the expected 1-D spatial profile is calculated to be:

$$E[F_z(x)] = \int_{-\infty}^{+\infty} h(\Lambda) F_z(\Lambda) d\Lambda \tag{3.20}$$

The results are shown in Fig. 3.9.

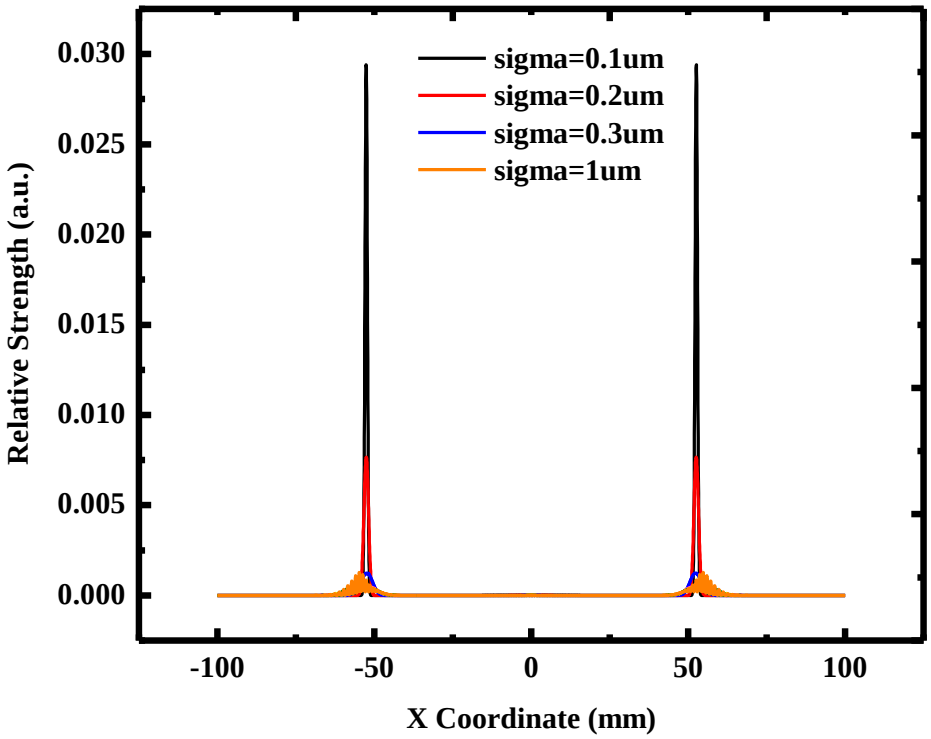

Fig. 3.9 Simulation of domain period with random errors

As the standard deviation varies from 0.1 μm to 1 μm, the strength of the far-field pattern decreases drastically.

3.3.6 Partially poled waveguide

In the fabrication of proton-exchange periodically poled lithium niobate waveguide, the waveguide is made, followed by the periodic poling by applying alternate strong electric field across the chip. In such cases, the periodically poled part may not fill the whole volume of the waveguide, which will lead to some interesting changes in the far-field pattern for surface-emitting second-harmonics. See Fig. 3.10.

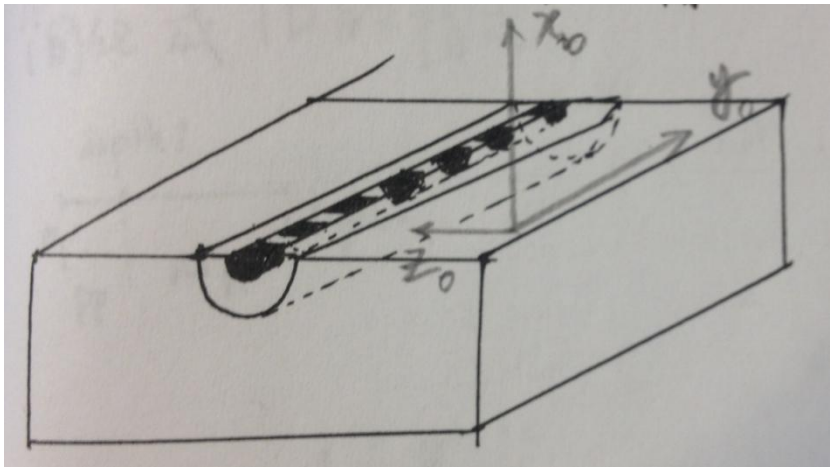

Fig. 3.10 Illustration of partially poled waveguide

We start by considering the 1-D case with perfect QPM grating structure. Assuming that depth of the total waveguide is d_2, and that of the periodically poled portion is d_1, $d_2 > d_1$. The far-field pattern integral is given by:

$$f_z(x) = \int_0^{d_1} A' \bullet [\frac{1}{2} g'(N+\frac{1}{2}) + \frac{1}{2} g'(-N-\frac{1}{2}) + \sum_{p=-N}^{N} g'(p+\frac{1}{2}) - \sum_{p=-N}^{N} g'(p)] dx_0 + \int_{d_1}^{d_2} A' \bullet \{erfz[\sqrt{\frac{i^3 k}{2(z+x_0)}}(\frac{L}{2}-x)] - erfz[\sqrt{\frac{i^3 k}{2(z+x_0)}}(-\frac{L}{2}-x)]\} dx_0$$

(3.21)

where

$$A' = -\frac{i\sqrt{\pi}}{2\sqrt{\frac{ik}{2(z+x_0)}}}\frac{\exp[ik(z+x_0)]}{\sqrt{i\lambda(z+x_0)}}, \quad g'(m) = erfz[\sqrt{\frac{i^3k}{2(z+x_0)}}(m\Lambda_0 - x)] \tag{3.22}$$

It is not difficult to apply the results to the 3-D case for a real waveguide. Applying the Cartesian coordinate in Fig. 3.6.1 (a), the far-field integral is given by:

$$f_z(x,y) = \exp[ik(z+z_0)]\iint_{yz}\frac{dy_0dz_0}{\lambda(z+z_0)}\int_{-L/2}^{L/2} f_0(x_0)\exp[i\frac{k(x_0^2+y_0^2)}{2(z+z_0)}]\exp[-i\frac{2\pi(xx_0+yy_0)}{\lambda(z+z_0)}]dx_0$$

$$= \exp[ik(z+z_0)]\iint_{pp\ part}\frac{A'dy_0dz_0}{\lambda(z+z_0)}[\frac{1}{2}g'(N+\frac{1}{2})+\frac{1}{2}g'(-N-\frac{1}{2})+\sum_{p=-N}^{N}g'(p+\frac{1}{2})-\sum_{p=-N}^{N}g'(p)]\bullet Q(y_0,z_0,y)$$

$$+\exp[ik(z+z_0)]\iint_{non-pp}\frac{A'dy_0dz_0}{\lambda(z+z_0)}\{erfz[\sqrt{\frac{i^3k}{2(z+x_0)}}(\frac{L}{2}-x)]-erfz[\sqrt{\frac{i^3k}{2(z+x_0)}}(-\frac{L}{2}-x)]\}\bullet Q(y_0,z_0,y)$$

(3.23)

where

$$Q(y_0,z_0,y) = \exp[i\frac{ky_0^2}{2(z+z_0)}]\exp[-i\frac{2\pi yy_0}{\lambda(z+z_0)}] \tag{3.24}$$

As a matter of fact, Eq. (3.23) is the general expression for all cases as long as we substitute the pupil function $f_0(x_0)$ with desired domain distribution. The simulation curves for the simplified 1-D version are shown in Fig. 3.10.

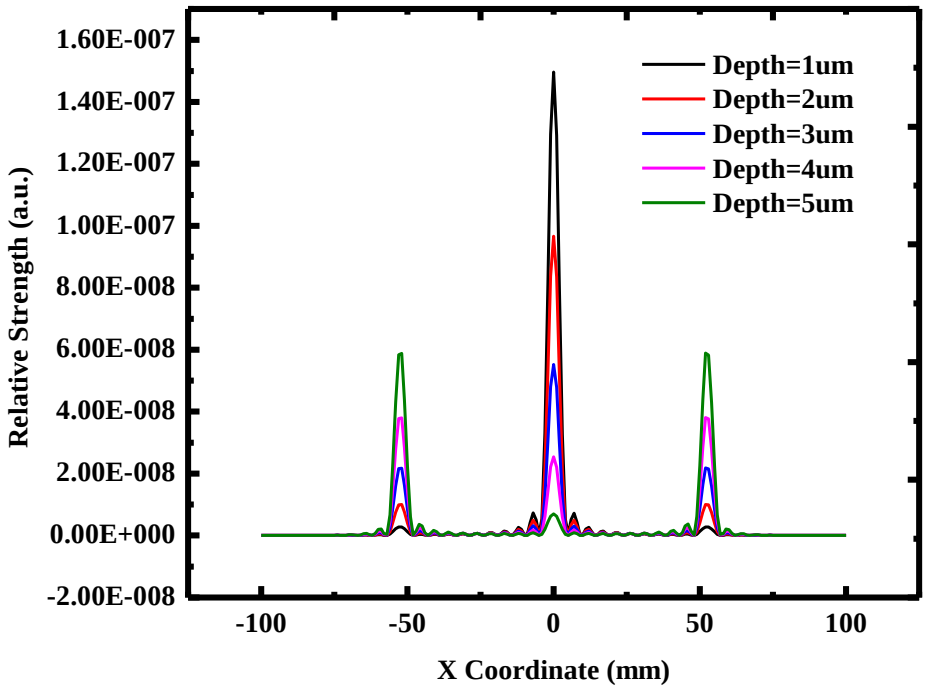

Fig. 3.11 Simulation for 1-D partially poled waveguide

The regions without periodically poled structure is equivalent to the case where a=0 in section 3.3.5. Therefore, the more volume of un-poled region exists in the waveguide, the more prominent of the center peak it is.

3.4 Analysis on experimental results

By measuring the distances among the centers of these three beams, we have determined $\sin\theta$ and found that the experimental values agree well with the calculated values.

Using Eq. (3.1), the simulated results are illustrated in Fig. 3.4. As one can see, there are only two peaks instead of the three peaks observed in our experiment. The third peak in the middle is due to the fact that the depth of periodic poling is less than the depth of the waveguide, as shown in Fig. 3.11. The SH beam generated by monodomain, i.e. the region which was not periodically poled makes up the center beam (see Fig. 3.10. with the different poling depths). Thus, we can determine the ratio of the poling depth and the waveguide depth by measuring the powers within three distinct beams (poling depth ratio). Fig. 3.12 confirms the linear power dependence on the pump power from one of the counter-propagating beams. We have determined the linear taper coefficient, defined as $c=(l_N-l_1)/N$, Indeed, according to Fig. 3.6, the left and right SH beams may exhibit an unsymmetrical power distribution when linear taper exists.

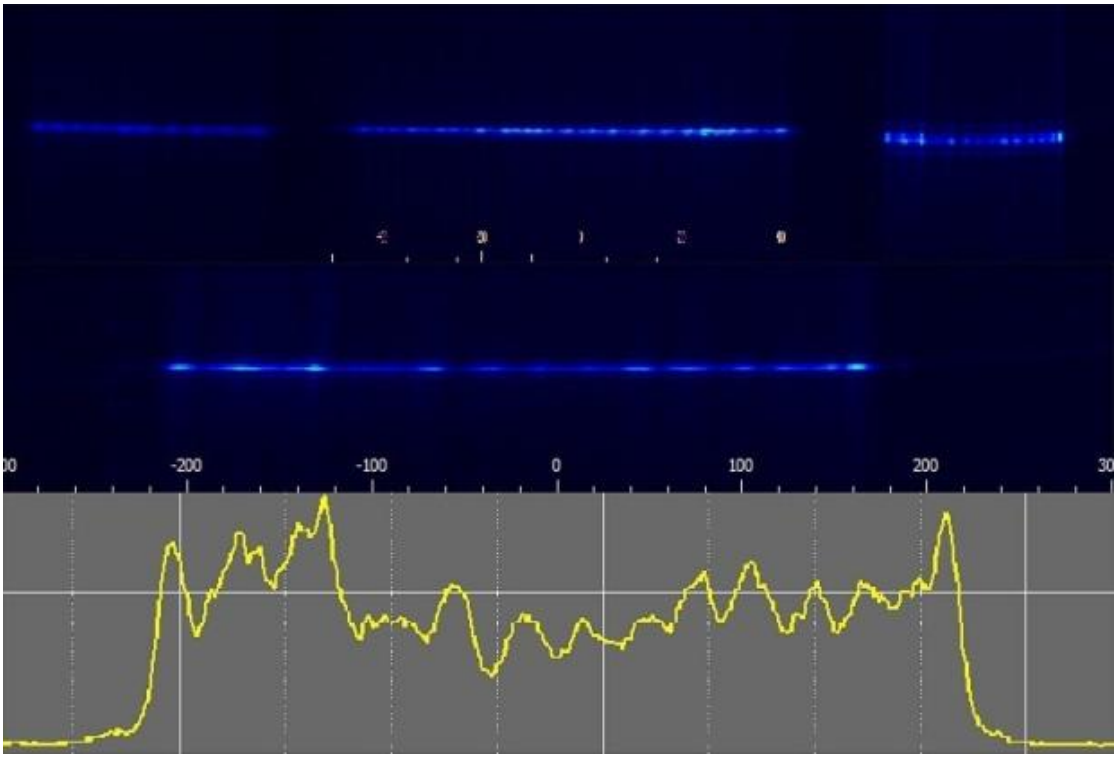

Fig. 3.11. (Top) Total Diffraction Pattern on CCD (Middle) Right portion (Bottom) Right portion spatial intensity distribution against lateral distance

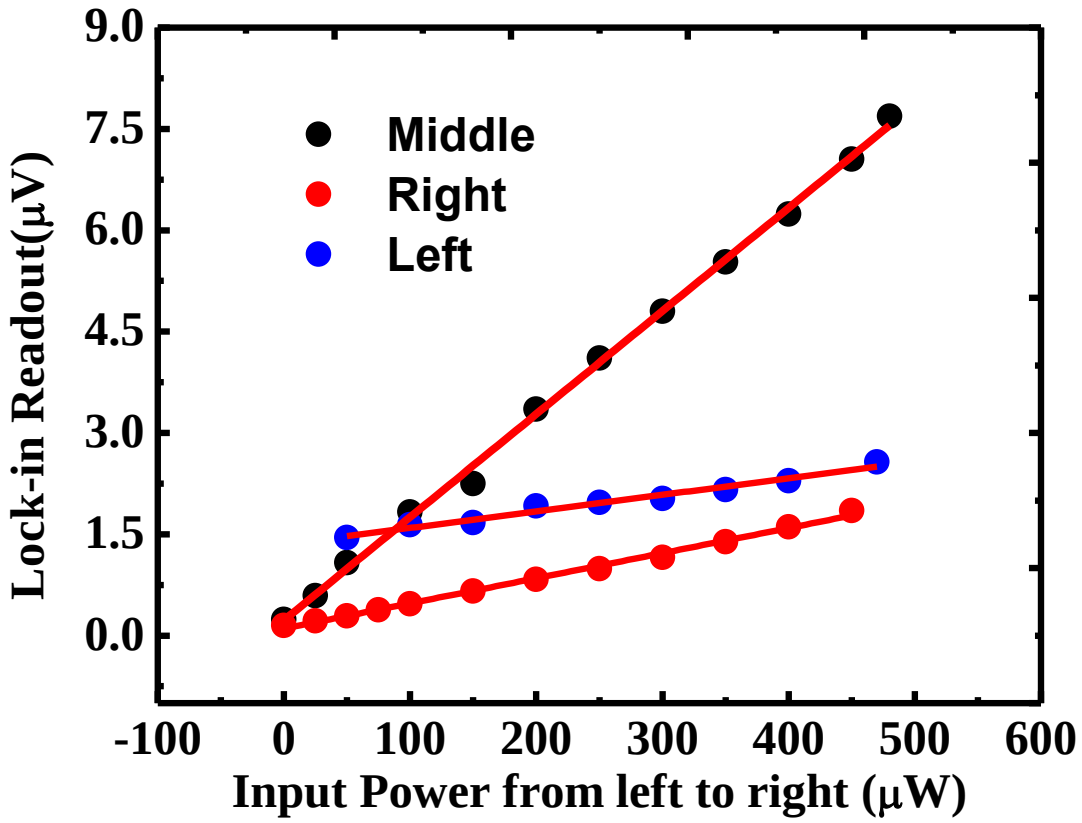

Fig. 3.12 Power Dependence for each fraction

For our experiment, the poling depth ratio is deduced to be 40%±3%. The linear taper coefficient is determined to be $(5.5\pm0.2)\times10^{-7}$mm. This indicates that on an average the adjacent domain period difference is around 0.5 nm, which reaches a nanoscale level. Many other domain quantities can be determined by giving a perturbation to the QPM grating and investigating the resulting spatial pattern. It is worth noting that our 1-D model can be readily extended to a 3-D model to evaluate characteristics of bulk and 2-D periodically-poled domains.

3.5 Conclusion for Chapter 3

In summary, we have developed an effective nondestructive technique to evaluate the quality of periodically-poled ferroelectric domains in a waveguide. Using such a technique, we have determined average poling period, degree of linear tapering, and poling depth ratio. We also calculated the far-field pattern under other possible domain imperfections. Our results show that such a technique has reached a nanoscale resolution for evaluating domain period.

Chapter 4

Enhancement of forward and backward Anti-stokes Raman signals in lithium niobate waveguides

4.1 Historical Overview

Anti-Stokes Raman is an effective technique to investigate phonon dynamics [52]. In addition, combining with Stokes Raman, anti-Stokes Raman can be used to investigate the hot phonon effects [53]. However, anti-Stokes signals are much weaker than Stokes signals due to inherently-low phonon occupation numbers. Therefore, in the past, relatively high pump powers were required to probe anti-Stokes signals. Indeed, the pump power of around 100 mW was used to generate measurable anti-stokes and stokes photons [54,55]. As a result, there could be a strong heating effect. Such an effect induces Raman frequency shifts and modifies phonon decay rates, resulting in broadening of Raman peaks [55]. Since the elevated temperatures are unknown, such an effect causes large errors in determining phonon decay rates and phonon temperatures. Therefore, it is important for us to improve the signal strength of anti-Stokes Raman.

Here, we present our new result on the forward and backward anti-Stokes Raman scattering. For the first time, we identified five and three propagating anti-Stokes peaks from the waveguide for the forward and backward configurations, respectively. These two different sets of the peaks are unique for the two configurations. Moreover, we have not only observed an enhancement factor of 30 for the waveguide but also reduced the pump power by *five orders of magnitude* compared with the previous value [54,55].

4.2 Theory

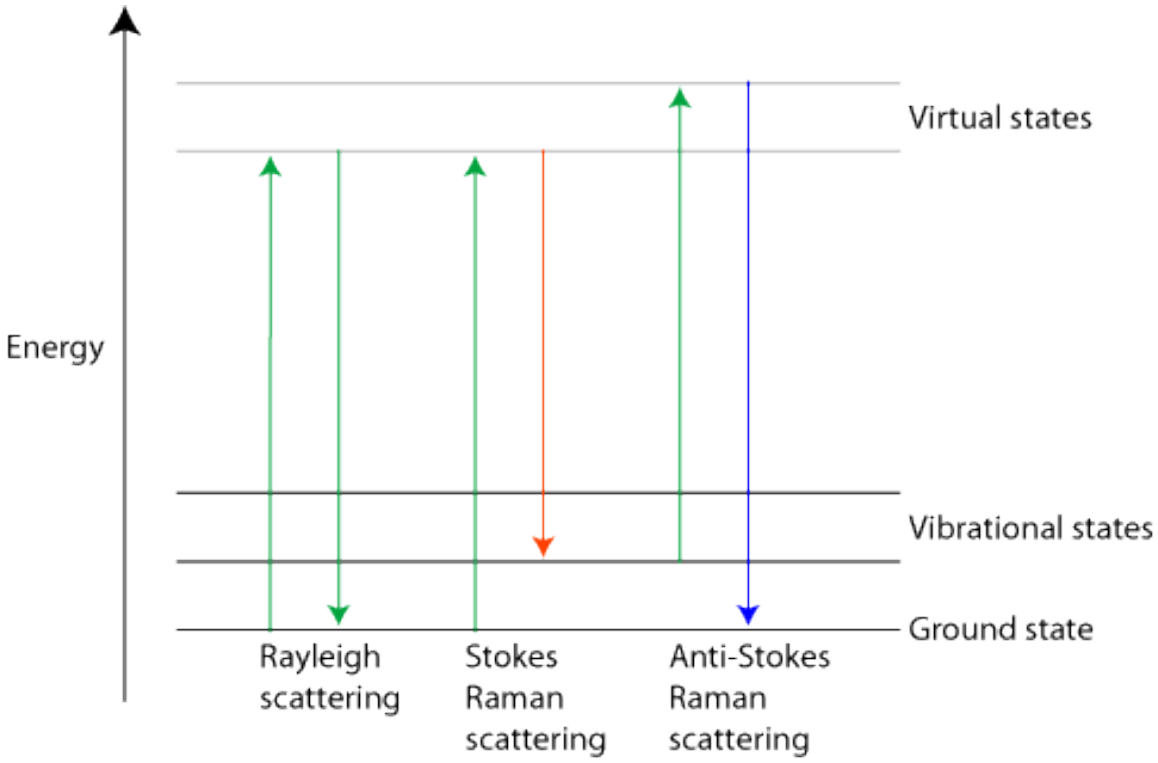

Fig. 4.1 Illustration of Stokes and Anti-Stokes Raman Scattering [56]

The spontaneous Raman Effect was discovered by C. V. Raman in 1928. A beam of light with certain frequency (ω_p) illuminates on a material sample and the scattered light is measured with spectrometer. The incident light (called pump here) interacts with optical photons (with frequency ω_s) in the material and could result in scattered photons with altered frequency, i.e. ω_p-ω_s (Stokes) and ω_p+ω_s (Anti-stokes), see Fig. 4.1. Typically, the strength of Anti-stokes lines will be much weaker than Stokes lines, as in thermal equilibrium, the population of the ground level is greater than that of the vibrational states, or in other words, the optical photon level [2].

4.3 Experimental Setup

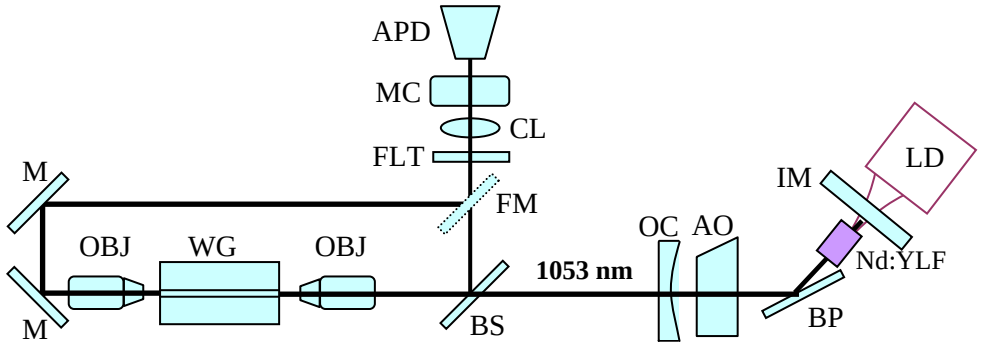

Fig. 4.2. Experimental setup for forward- and backward- Anti-stokes signal measurement. LD - laser diode at 808 nm, IM - input mirror, OC - output coupler, BP - Brewster plate, AO - acousto-optic Q-switch, BS - Beam Splitter, OBJ – objective, WG – waveguide, FLT - filter, CL-convex lens, MC –

In our experiment, a compact and portable Nd:YLF laser was used as a pump source for the generation of the anti-Stokes Raman signals. As shown in Fig. 1, a $4\times4\times10$ mm^3 Nd:YLF crystal was pumped by a 808-nm diode laser in a plano-concave laser cavity. Such a laser generated two orthogonally-polarized output beams at 1053 nm and 1047 nm, respectively. In the laser cavity, a Brewster plate was served as a wavelength selector whereby the 1053-nm wave was oscillating whereas the 1047-nm beam was transparent and will not return to the laser cavity. The reflectivity for 1053-nm wave is 99.5%. An acousto-optic *Q*-switch was used to modulate the laser output at 5 kHz. The pulse width of the laser was 10 ns. A flip mirror was placed in front of the photon collection system to measure the forward-propagating photons or backward-propagating photons. A 95% beam splitter was placed in the optical path to collect the backward-propagating anti-stokes photons generated by the $LiNbO_3$ waveguide. The photon collecting system consisted of an edge filter to cut off the pump beam, a convex lens, and a monochromator.

The photons were then measured by a Si APD with dark count rates of $< 25\ s^{-1}$.

4.4 Results and Discussion

4.4.1 Backward-propagating Anti-stokes signals

Our first sample, which was used to study the properties of backward-propagating anti-Stokes signal, was an x-cut $LiNbO_3$ chip with six Ti-diffused waveguides of lateral widths from 5 μm to 10 μm with an increment of 1 μm. The coupling efficiencies were measured to be 47.1% (10 μm), 38.9% (9 μm), 24.5% (8 μm), 10.0% (7 μm), 3.6% (6 μm), and 2.7% (5 μm), respectively. The polarization of 1053 nm beam was along the optical *z* axis of the $LiNbO_3$ waveguide.

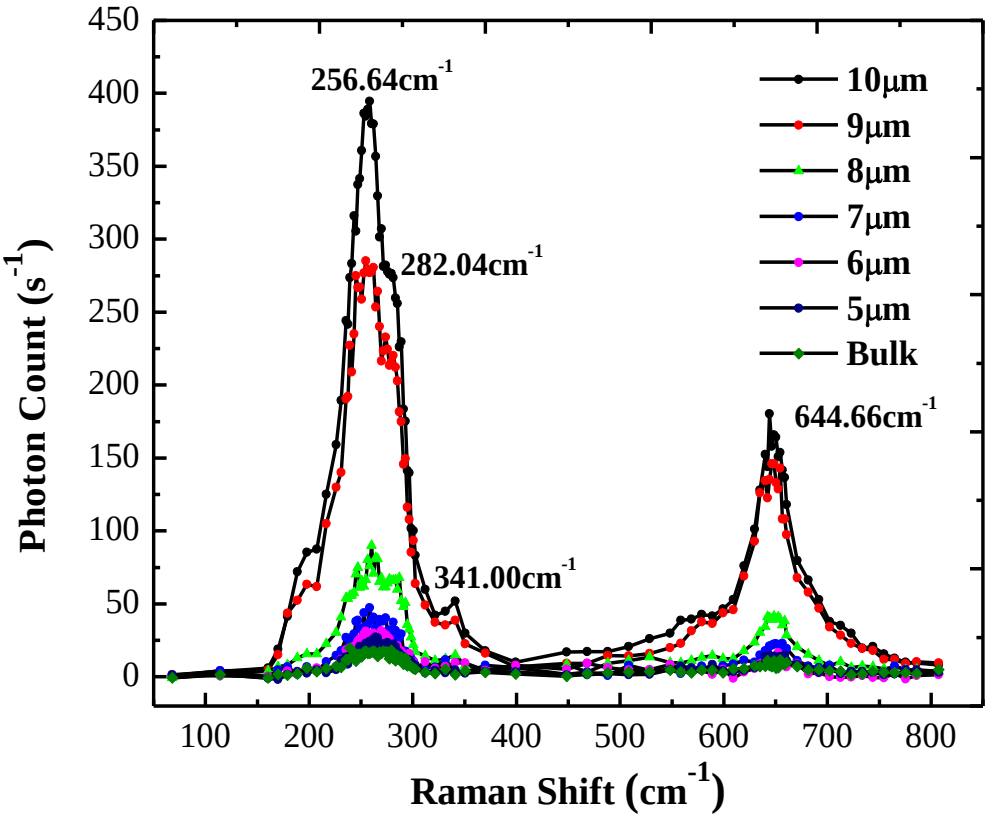

Fig. 4.3 Backward Anti-Stokes photon count vs. Raman shift Experimental at different waveguide widths.

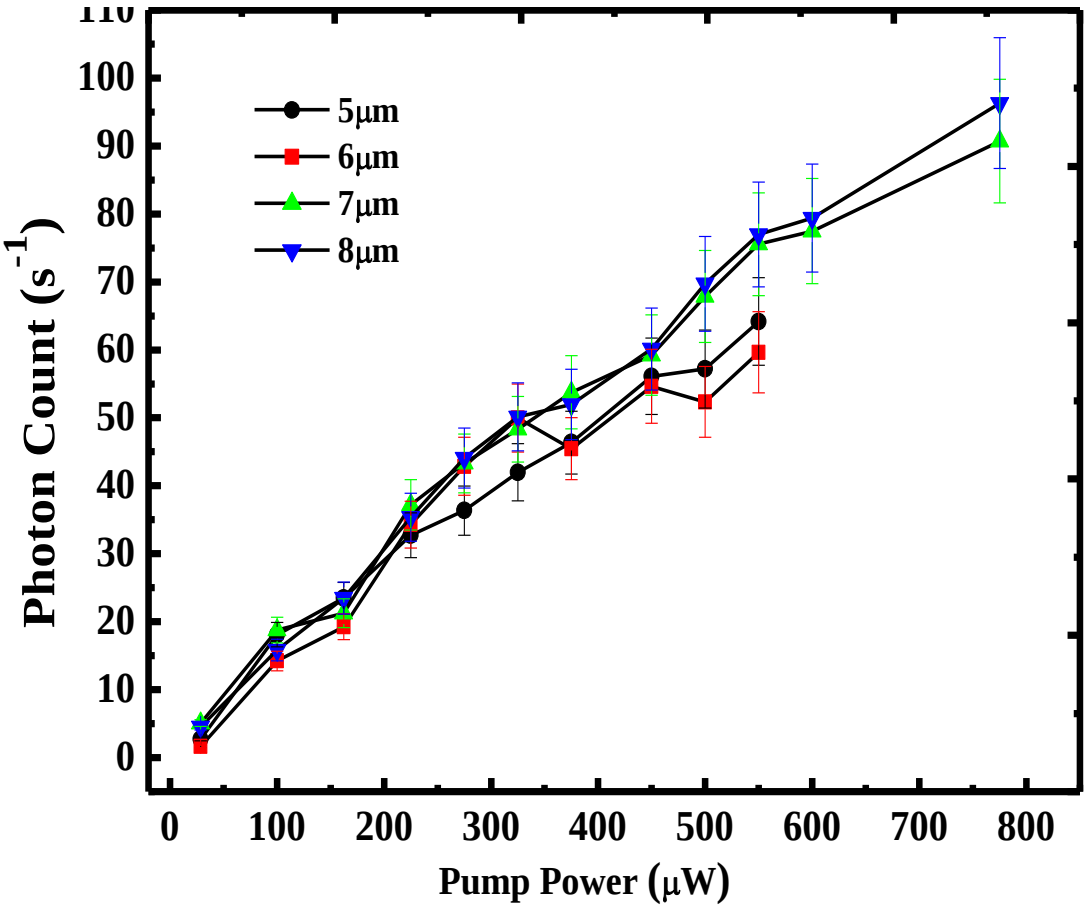

Fig. 4.4 Photon count vs. pump power coupled into waveguide at different widths

According the Raman spectra measured by us, see Fig. 4.3, four Raman shift peaks at 256.64 cm^{-1}, 282.04 cm^{-1}, 341.00 cm^{-1}, and 644.66 cm^{-1} were identified. In $LiNbO_3$, phonon branches are labeled by $5A_1$, $5A_2$ and $10E$ at a nearly zero wave vector. Out of these phonon branches, the five A_2 fundamentals and $4A_1$ and $9E$ optical branches are Raman active [59]. The four peaks are then identified as E(TO3) mode, E(TO3)+E(LO3) combination mode, E(LO4) mode, and A_1(TO) mode [57], respectively. The positions of the Raman peaks indicate that the orientation of the crystal during measurement should be notated by $Y(Z,Z)\bar{Y}$ based on Porto notation [60], based on the crystal orientation, propagation and polarization of the pump beam and Raman scattering signal.

In order to efficiently generate anti-Stokes signals, the following equations must be satisfied:

$$\begin{aligned} \hbar\omega_p &= \hbar\omega_{as} - \hbar\omega_q \\ k_p &= \pm(k_{as} - q) \end{aligned} \tag{4.1}$$

where ω_p denotes the angular frequency of pump, ω_{as} the angular frequency of anti-Stokes signals, ω_q the angular frequency of phonon, k_p the wave vector of the pump, k_{as} the wave vector of anti-Stokes signals, and q the wave vector of phonon. The plus/minus sign denotes forward/backward propagating configuration. The fact that the value of q, which can literally take any number between 0 and $2\pi/c$ (Brillouin zone boundary), where c is the crystal constant and is usually several Ångström (Å), is more than enough to satisfy the momentum conservation requirement. Therefore, we can always pick a (ω_q, q) pair to fulfill a given Raman scattering configuration, or in other words, the process is always phase-matched if spatial overlap of pump and anti-Stokes signal is guaranteed. In the case of waveguide, both the pump and Raman beams propagate in the waveguide. As a result, the presence of the waveguide allows the spatial accumulation of the Raman

signals, resulting in the large enhancements over that from the bulk crystal. In our experiment, the highest enhancement factor obtained by us is 30. In such a case, the pump power of as low as 230 nW is sufficiently for probing the anti-Stokes Raman signal. Therefore, our observation can be considered as the first step for developing a compact and portable anti-Stokes Raman probe.

We also measured the backward anti-stokes photon count by using the APD, generated by each waveguide having a different width, as a function of the pump power, see Fig. 4.4. One can see that the dependence was linear under relatively low powers. However, at relatively high pump powers the data deviated from the linear dependence. This was probably caused by the local heating effect [58]. This result illustrates the importance of using low pump powers.

4.4.2 Forward-propagating Anti-stokes signals

In order to investigate the difference between backward and forward propagating anti-Stokes signals, we alternated the sample to a reverse proton exchanged x-cut $LiNbO_3$ waveguide chip, which has higher photorefractive effect damage threshold and polarization restriction that allows only beams polarized along optical z direction to have the maximum transmission. We chose the 10-μm-wide waveguide to conduct the experiment. We measured the forward-propagating and backward-propagating anti-Stokes photons generated by the waveguide and the bulk $LiNbO_3$ crystal, see Fig. 4.5, which correspond to $Y(Z,Z)Y$ and $Y(Z,Z)\bar{Y}$ as denoted by Porto notation, respectively. According to Fig. 4.5, we identified five anti-stokes peaks for the forward configuration at the Raman shifts of 200.96 cm^{-1}, 258.68 cm^{-1}, 292.64 cm^{-1}, 348.61 cm^{-1} and 565.90 cm^{-1}, respectively. Based on Fig. 4.6, the count rates in the waveguide are obviously much higher than those in the bulk crystal. We assigned 200.96 cm^{-1}, 258.68 cm^{-1}, 292.64 cm^{-1}, 348.61 cm^{-1}, and 565.90 cm^{-1}, the Raman scattering from the phonon modes of E(LO1), E(TO3), E(LO3), E(LO4), and E(TO8) [57], respectively. It is worth noting that for the forward-propagating configuration the Raman peak is located at 565.90 cm^{-1} whereas the peak for the backward-propagation configuration is blue-shifted to 654.19 cm^{-1}. This is due to the differences of the phonon wave vectors required to satisfy the phase-matching condition for the Raman scattering explained earlier in the paper. Indeed, for the backward-propagating configuration the wave vector required to satisfy the phase-matching condition is much larger. Due to the phonon dispersion, the Raman frequency shift for the backward configuration is significantly different from that for the forward configuration.

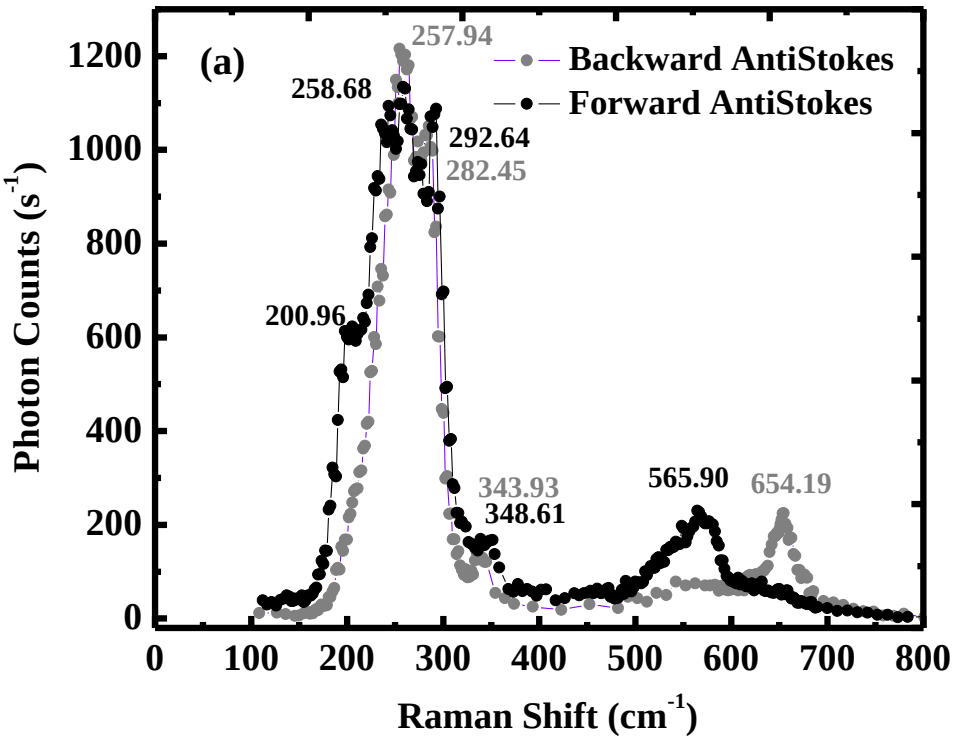

Fig. 4.5 Forward and backward anti-Stokes Raman spectra in $LiNbO_3$ waveguide

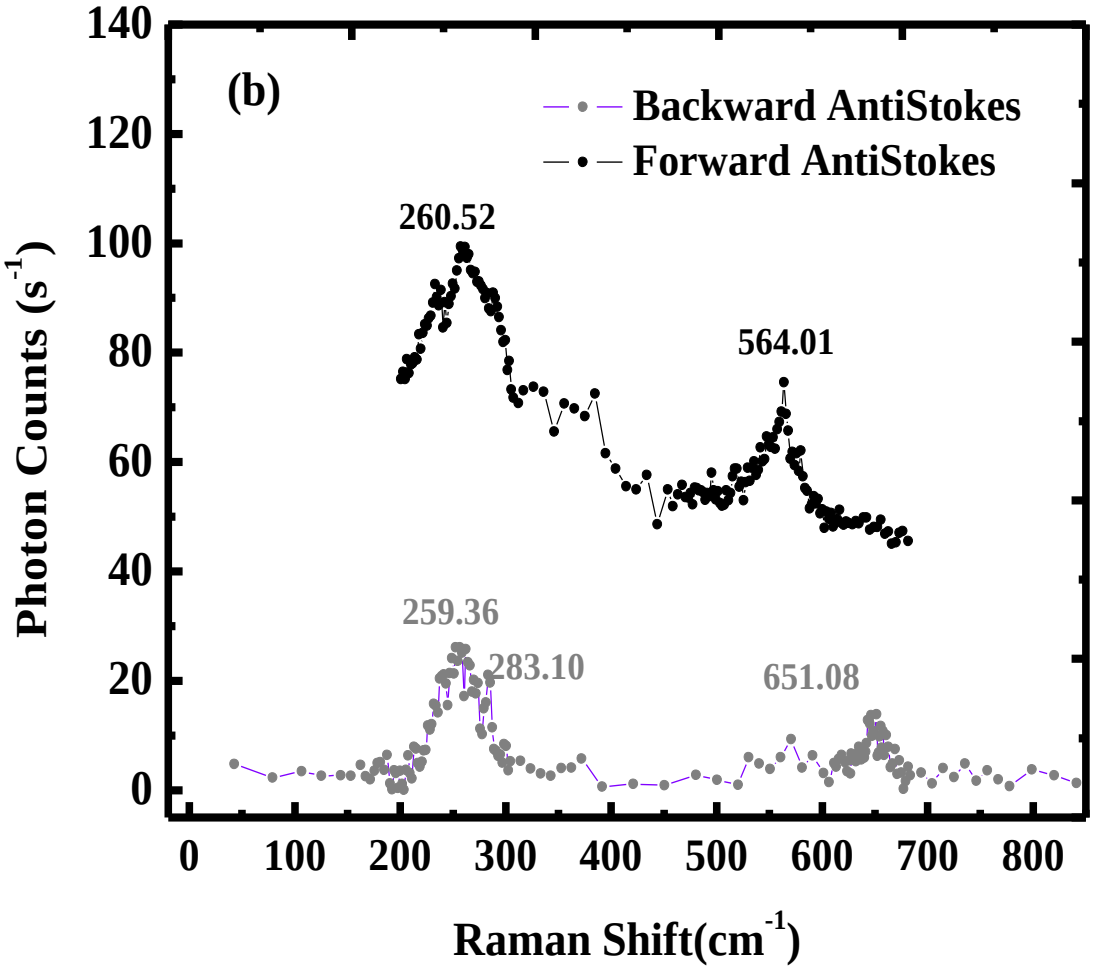

Fig. 4.6 Forward and backward anti-Stokes Raman spectra in $LiNbO_3$ bulk crystal. The spectrum for forward configuration in bulk crystal is vertically up-shifted due to presence of strong laser radiation in the range.

4.5 Conclusion for Chapter 4

In this chapter, we have demonstrated that a compact and portable Raman probe device is achievable by employing sending pump beam into a waveguide structure, which has more than 30 times enhancement compared to signals in bulk material. By detecting using Si-based single photon detector, we can readily reduce the pump power to a few microwatts, which is capable of greatly relieving the local heating effect. We have also discovered that the forward and backward propagating anti-stokes signals have exhibited significant difference in spectral features due to the fact that the phonon wave vectors required to satisfy these two configurations are different. Backward propagating anti-Stokes has application in correction of phase-distorted images through phase conjugation.

Chapter 5

Terahertz generation based on parametric conversion in Gallium Phosphide plates

5.1 Overview

Terahertz (THz) wave refers to electromagnetic waves with wavelengths from 30 μm to 3000 μm [61]. In the frequency domain, it lies between microwave and infrared wave. Terahertz wave has promising utilities in security screening and therefore, extensive study towards the generation of terahertz wave has been performed. Quantum cascade lasers are capable of emitting THz via the proper design of multiple quantum wells. However, such emitters will need cryogenic temperatures for operation [62]. Broadband THz pulses can be generated from electro-optic crystals pumped by picoseconds laser pulses based on optical rectification [63], photocurrent surge [64], and Cherenkov radiation [65]. Applications in chemical sensing and detections of biological and chemical agents would prefer a tunable THz source, which can be implemented by difference frequency generation (DFG) of two close-wavelength infrared beams in Gallium Phosphide (GaP) plates. Compared with other ways of generating THz waves, DFG approach benefits from room temperature operation, various choices of IR sources,

and wide tunability. In this Chapter, we investigated THz generation in alternatively stacked GaP plates and as a result, we achieved maximum photon conversion efficiency of 40% and observed back parametric conversion [41].

5.2 Experimental Setup

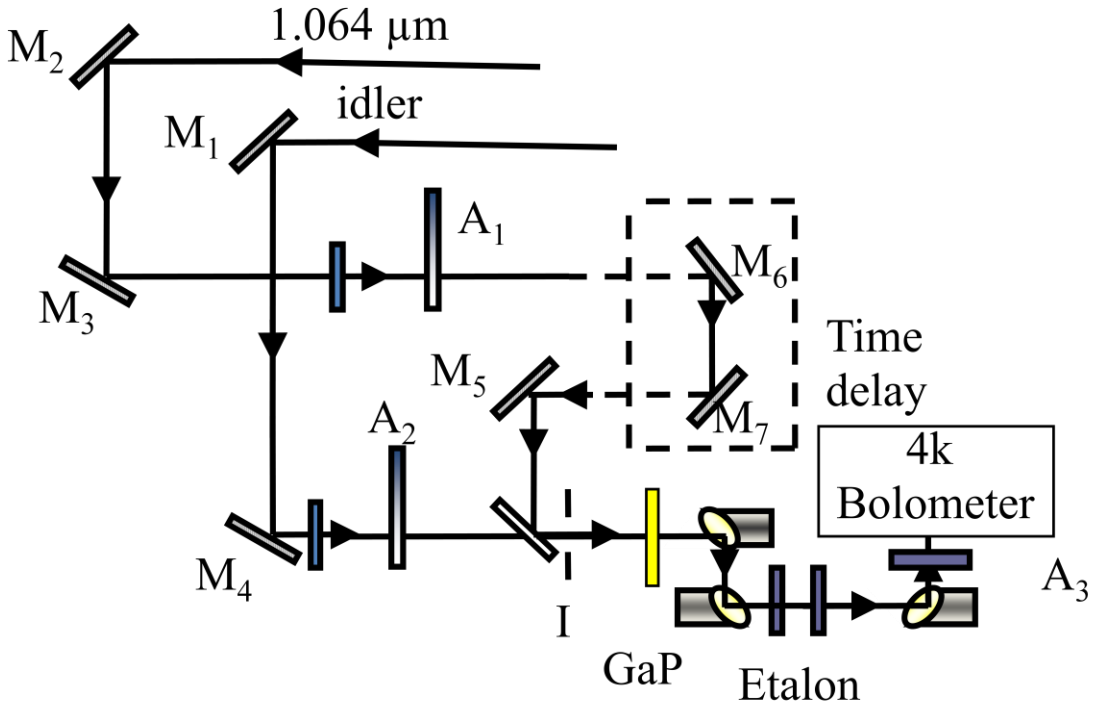

Fig. 5.1 Experimental setup for THz generation in GaP stacks

We investigated the THz generation from two stacking configurations of the GaP plates. Each plate has a diameter of 48.5 mm and a thickness of 663 μm. In the reversely-stacked geometry, every the other plate was rotated around z axis of the crystal by 180 °. As a result, effective second-order nonlinear coefficient changes its sign from one plate to the next, and therefore, such a configuration can be used to achieve quasi-phase matching (QPM) for the THz generation based on DFG at each designated set of the mixing and THz output wavelengths. On the other hand, in the forwardly-stacked geometry, all the plates were stacked in the way that each second-order nonlinear coefficient has the same sign from one plate to the next.

Two coherent beams used for DFG were generated by a Nd:YAG laser at 1.064 μm (≤ 15.0 mJ, 10 ns) and a β-BaB_2O_4-based master oscillator/power oscillator (≤ 20.4 mJ, 5 ns). The beam radius for both of the mixing beams was 1.0 mm upon entering the stacked GaP plates. These coherent beams collinearly propagated in a direction opposite to the surface normal of the stacked GaP plates, with their polarizations being parallel to the [1-10] and [001] directions, respectively. Therefore, we can access the large effective second-order nonlinear coefficient of each GaP plate through the QPMed DFG [66]. The THz output beam was then generated by DFG.

5.3 Results and discussion

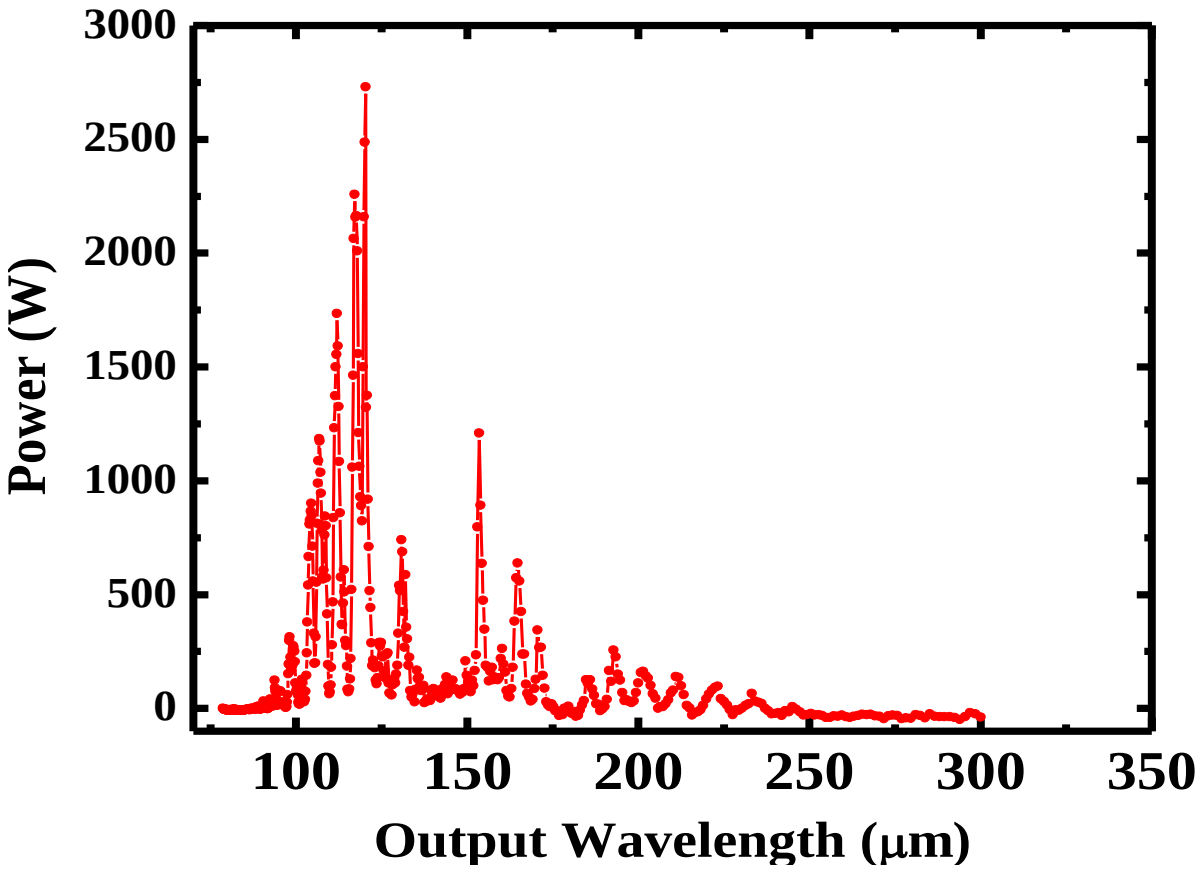

Fig. 5.2 Spectrum of THz radiation generated by reversely-stacked four GaP plates, covering tuning range of 78-300 μm [41];

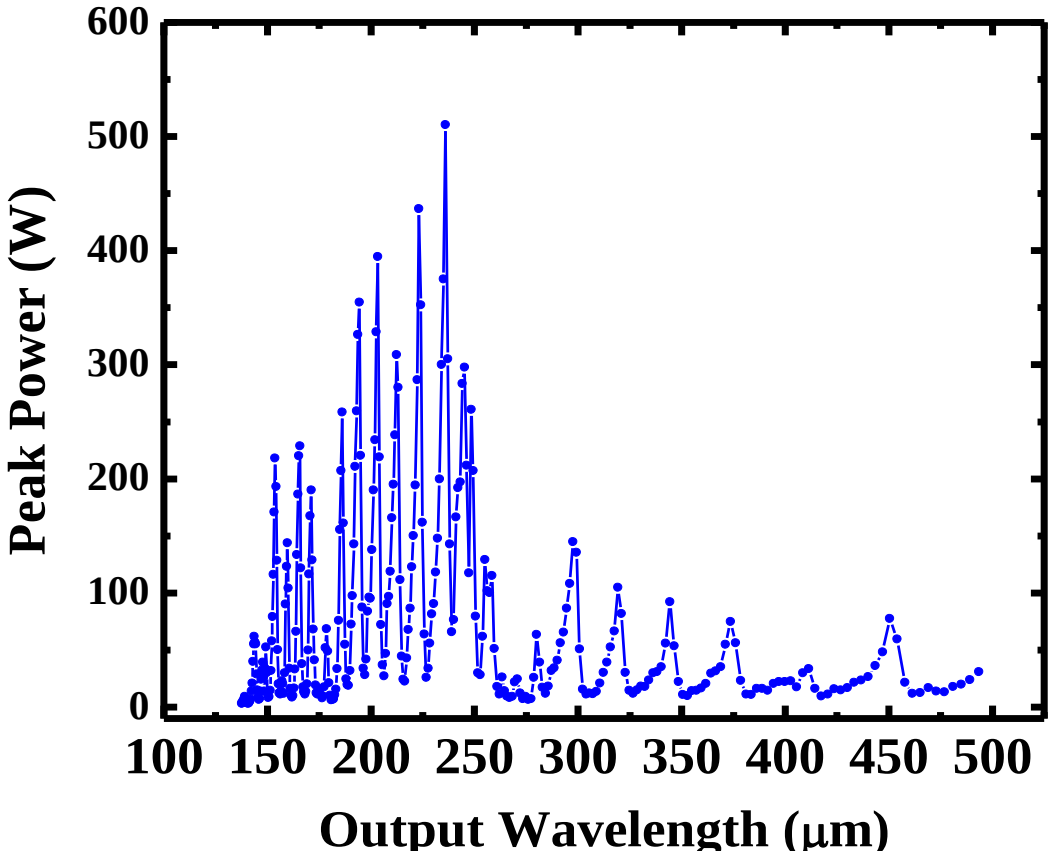

Fig. 5.3 Spectrum of THz radiation generated by forwardly-stacked four GaP wafers, covering tuning range of 135-500 μm [41].

We first measured the spectra of the THz radiation generated by the reversely-stacked four GaP plates (the total thickness of 2.65 mm), see Fig. 5.2. According to Fig. 5.2, the output wavelength of the THz radiation was tuned continuously from 78 μm to 300 μm. At the output wavelength of 120.3 μm, DFG was QPMed. Therefore, the output power at this wavelength was dramatically increased by reversely stacking the four GaP plates. The highest output peak power was measured to be 2.73 kW. This is the highest peak power reported so far for the nanosecond THz pulses generated by DFG. At such a power, the input powers for the two mixing beams were measured to be 1.5 MW and 4.1 MW, respectively. The corresponding conversion efficiency, defined in terms of the peak powers is determined to be 0.18%. Taking into consideration the Fresnel reflection losses at the input and at the output facets, the internal photon conversion efficiency is 39.6%. To the best of our knowledge, this is the highest photon conversion efficiency which has ever been achieved for the THz generation based on DFG. As shown in Fig. 5.4, the generated THz is approaching saturation. The individual peaks in the spectrum with the same frequency separation were caused by the Fabry-Pérot interference effect inside the GaP plates. As the number of the GaP plates was increased from 4 to 5, the output power and conversion efficiency were reduced, see Fig. 5.5. This is likely due to the back parametric conversion of the THz wave inside the GaP plates.

We also measured the spectrum of the THz radiation from the forwardly-stacked four GaP plates (the thickness of 2.65 mm), see Fig. 5.3. Based on Fig. 5.3, the output wavelength of the THz radiation was from 135 μm to 500 μm. The maximum output peak power reached 510 W at the wavelength of 236 μm, corresponding to a power

conversion efficiency of 0.034%. The internal photon conversion efficiency is 14.6%, which is significantly lower than that under the reversely-stacked geometry.

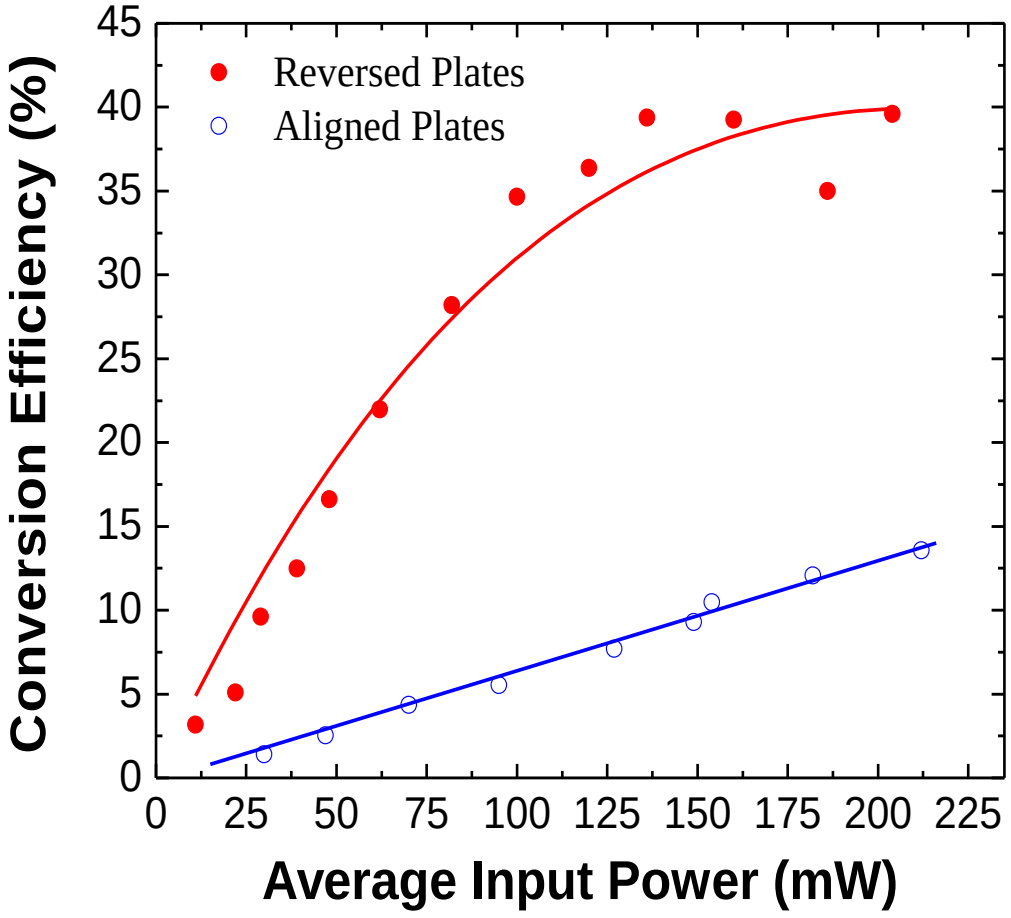

Fig. 5.4 Photon conversion efficiency vs. input power at 1.0737 μm and 1.0690 μm for reversely-stacked and forwardly-stacked GaP plates, respectively. For both of the geometries, input power at 1.0642 μm was set to 150 mW. Solid line – nonlinear least square fit to data points using Eq. (1). Dashed line – linear fit to data points [41].

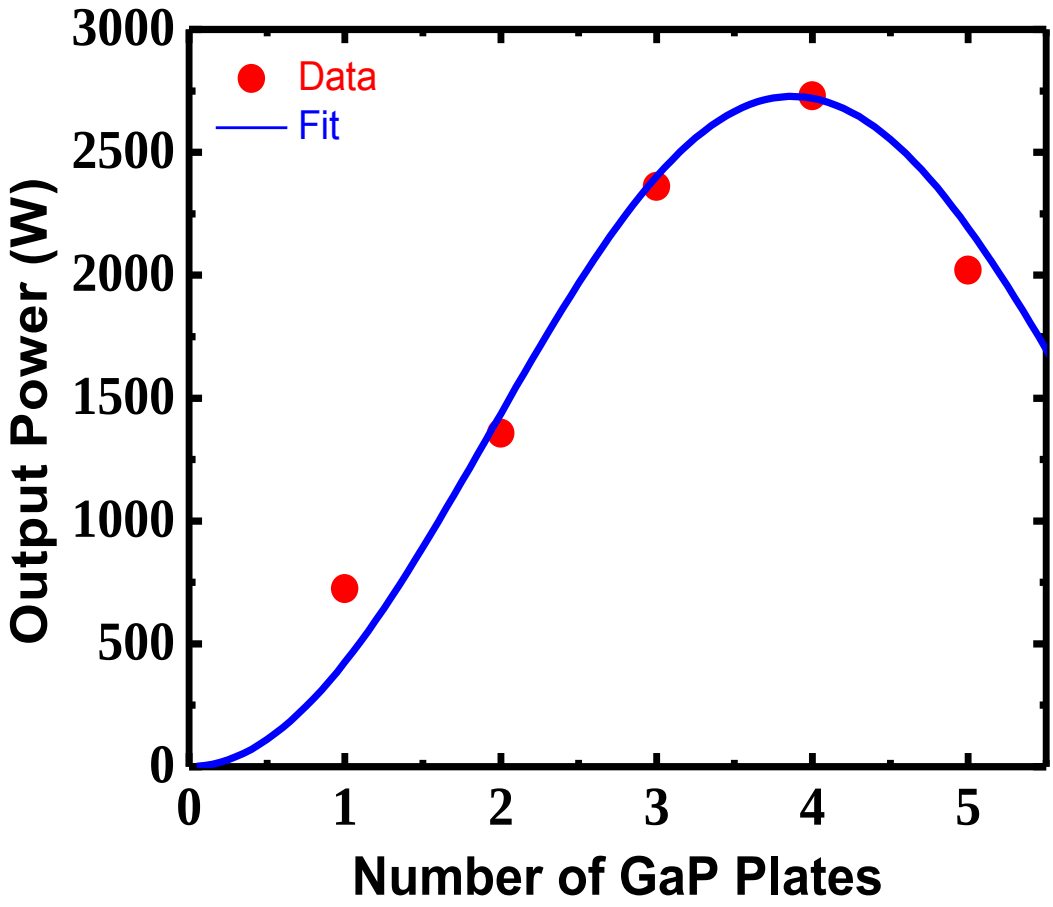

Fig. 5.5 Highest THz output power generated by reverse GaP plates versus the number of plates. Blue curve represents nonlinear least square fit to data points using Eq. (5.1) [41]

Fig. 5.4 illustrates the dependence of the internal photon conversion efficiency on the average input power. Under the reversely-stacked geometry, the conversion efficiency increases linearly below the input power of 50 mW. However, as the input power is increased further, the saturation of the conversion efficiency becomes stronger and stronger. When the input power approaches 200 mW, the conversion efficiency reaches a plateau. The highest conversion efficiency achieved in our experiment is 39.6% at the input power of 204 mW (130 MW/cm^2). To the best of our knowledge, this is the first report on the strong saturation in the conversion efficiency for the THz pulses generated by DFG. According to Ref. [67], the photon conversion efficiency can be written in the following form:

$$\eta_p = \eta_{\max} \sin^2[(\pi/2)\sqrt{P_i / P_{opt}}] \tag{5.1}$$

where $\eta_{\max}$ is the maximum conversion efficiency, P_i and P_{opt} are the input and optimal powers, respectively. Following the nonlinear least square fitting to the data points by using Eq. (5.1) above, we have obtained $\eta_{\max} \approx 40.0\%$ and $P_{opt} \approx 209$ mW. Therefore, we have indeed achieved the maximum photon conversion efficiency from our experiment. In comparison, for the forwardly-stacked GaP plates no obvious saturation was observed, see Fig. 5.5. The highest conversion efficiency is 14.6%. Such a comparison illustrates the importance of QPM for the THz generation.

5.4 Conclusion for Chapter 5

In this chapter, we investigated THz generation in reverse and forward stacked GaP plates, and have reached maximum conversion efficiency for THz generation in reversely stacked GaP plates. The highest output power generated inside the GaP plates reached 3.77kW at the wavelength of 120 μm in correspondence of the Quasi-phase matching condition. The internal photon conversion efficiency reached 39.6%. When we added one more GaP plate in the stacks from 4 to 5, we saw the output power decrease and that was evidence that back parametric conversion has taken place.

Chapter 6

Conclusion

6.1 Conclusion of Contribution

In this dissertation, we investigated several intriguing and novel applications in second-order nonlinear medium via optical multiple wave interactions, specially focusing on periodically poled lithium niobate waveguide, for its high second-order nonlinear coefficient (d_{33}=27 pm/V) and the waveguide feature to allow tight confinement of transverse modes for all interacting beams along the entire crystal length. Sum-frequency generation can be implemented in such a crystal to convert photons at communication band to visible band, which can be efficiently detected by Silicon based avalanche photodiode. We achieved noise-free detection and greatly enhanced the sensitivity of such a frequency up-conversion detector. Also, we proposed theoretical analysis to identify the noise photon numbers and it agreed well with our experimental results. Waveguide imperfection was analyzed to better support the data.

In the following, we summarize the contributions presented in this dissertation.

In Chapter 2, we demonstrated a single photon detector based on frequency upconversion in periodically poled lithium niobate waveguide. Since commercially available detectors at IR wavelengths, such as InGaAs/InP avalanche photodiodes (APDs)

suffer from drawbacks of high dark counts up to 10^5/s, as well as low quantum detection efficiencies, usually with values between 10% and 15%, they are not suitable for single photon detection operating at CW mode. In contrast, single-photon counting in near-IR (600-800nm) can be performed efficiently with silicon APDs. Single photon counting modules with dark counts lower than 25/s and detection efficiency in the range 50% to 70% are commercially available. Obviously, we can take advantage of silicon APDs by efficiently converting C-band photons to near-IR or visible photons. In our experiment, we have implemented single photon detection in periodically poled lithium niobate waveguide with 980nm pump, with negligible noise photon counts. The internal quantum efficiency has reached 62%, and the minimum incident number of photons we can detect is measured to be as low as 81 counts per second. We then theoretically investigated the generation of noise counts by considering both perfect and imperfect grating structures for lithium niobate. The key is that for a given grating period, the gain peak for spontaneous parametric down-conversion process and the gain peak for designed up-conversion process usually do not overlap, resulting in intrinsic low noise photon generation. The simulation gives noise photon generation rate of 77 counts per second, and it agreed well with our experimental results. At last, we explored GaP plates as an alternative second-order nonlinear material to implement single photon detection. Experimental results have been demonstrated and we investigated total-internal-reflection assisted phase-matching in GaP plate, where by other means perfect phase match cannot be achieved.

In Chapter 3, we have developed an effective nondestructive technique to evaluate the

quality of periodically-poled ferroelectric domains in a waveguide, by measuring the far-field pattern of second harmonics generated by two identical counter propagating IR beams in the waveguide. The diffraction angle is linked to the poling period with a simple expression. Using such a technique, we have determined average poling period, degree of linear tapering, and poling depth ratio. We also simulated the far-field pattern under other possible domain imperfections. We then compared our experimental results with the simulation to determine the imperfection parameters. Our results show that such a technique has reached a nanoscale resolution (0.5 nm) for evaluating domain period linear taper.

In Chapter 4, we have demonstrated that a compact and portable Raman probe device is achievable by employing sending pump beam into a waveguide structure, which has more than 30 times enhancement compared to signals in bulk material. By detecting using Si-based single photon detector, we can readily reduce the pump power to a few microwatts, which is capable of greatly relieving the local heating effect. We have also discovered that the forward and backward propagating anti-stokes signals have exhibited significant difference in spectral features due to the fact that the phonon wave vectors required to satisfy these two configurations are different. Backward propagating anti-Stokes has application in correction of phase-distorted images through phase conjugation.

In Chapter 5, we investigated THz generation in reverse and forward stacked GaP plates, and have reached maximum conversion efficiency for THz generation in reversely stacked GaP plates. The highest output power generated inside the GaP plates reached 3.77kW at the wavelength of 120 μm in correspondence of the Quasi-phase matching

condition. The internal photon conversion efficiency reached 39.6%. When we added one more GaP plate in the stacks from 4 to 5, we saw the output power decrease and that was evidence that back parametric conversion has taken place.

6.2 Outlook and future work

Single photon detectors based on frequency up-conversion have extensive use in gas detection and quantum communications. It is of great interest to develop this single photon detector to a gas concentration detection system. As we know, gases have their unique absorption lines suitable for detection, for example, 1.27 μm for O_2, 1.57 μm for CO_2, and 1.651 μm for CH_4. Same pump wavelength can be used as long as the poling period is designed to match the specific up-conversion process. The multiple waveguides with different poling period can even be fabricated on the same lithium niobate chip. By using reference gas cell and measuring the photon counts difference between reference gas cell and sample gas cell, the concentration of a specific gas can be precisely determined at a extremely low level (less than ppb) since the noise counts are almost zero. This gas detector can be useful to monitor the CO_2 gas concentration change in the atmosphere for climate purposes, or to monitor the CH_4 gas concentration change at natural gas production sites.

Bibliography

[1] P. A. Franken, A. E. Hill, C. W. Peters, and G. Weinreich, "Generation of optical harmonics",

Phys. Rev. Lett, **7**, 118 (1961)

[2] Robert W. Boyd (3rd Ed.) (2007) Nonlinear Optics, Rochester, NY, Academic Press, Elsevier

[3] M. D. Eisaman, J. Fan, A. Migdall, and S. V. Polyakov, "Invited review article: single-photon sources and detectors," Rev. Sci. Instrum., **82**, 071101/1-25 (2011).

[4] J. C. Howell, P. M. Anisimov, J. P. Dowling, and R. W. Boyd, "Single and biphoton imaging and high dimensional quantum communication," Quantum Information Processing, **11**(4), 925-948, (2012).

[5] M. Patel, J. B. Altepeter, M. A. Hall, M. Medic, and P. Kumar, "Experimental characterization of a telecom-based quantum controlled-NOT gate," J. Sel. Top. Quantum Electron, **15**(6), 1685-1693, (2009).

[6] M. Vasilyev and P. Kumar, "Frequency upconversion of quantum images," *Opt. Express*, **20**(6), (2012).

[7] J. H. Shapiro and R. W. Boyd, "The physics of ghost imaging," Quantum Information Processing, **11**(4), 949-993 (2012).

[8] http://decadal.gsfc.nasa.gov/ASCENDS.html

[9] F. Marsili, V. B. Verma, J. A. Stern, S. Harrington, A. E. Lita, T. Gerrits, I. Vayshenker, B. Baek, M. D. Shaw, R. P. Mirin, and S. W. Nam, "Detecting single infrared photons with 93% system efficiency," *Nature Photon*, **7**, 210-213 (2013).

[10] X. Yang, H. Li, W. Zhang, L. You, L. Zhang, X. Liu, Z. Wang, W. Peng, X. Xie, and M. Jiang, "Superconducting nanowire single photon detector with on-chip bandpass filter," *Opt. Express*, **22**(13), 16267-16272 (2014).

[11] R. V. Roussev, C. Langrock, J. R. Kurz, and M. M. Fejer, "Periodically poled lithium niobate waveguide sum frequency generator for efficient single-photon detection at communication wavelengths," *Opt. Lett.*, **29**(13), 1518–1520 (2004).

[12] M. A. Albota and F. N. C. Wong, "Efficient single-photon counting at 1.55 μm by means of frequency upconversion," *Opt. Lett*. **29**(13) 1449–1451 (2004).

[13] A. P. VanDevender and P. G. Kwiat, "High efficiency single photon detection via frequency up-conversion," *J. Mod. Opt*. **51**(9-10), 1433–1445 (2004).

[14] C. Langrock, E. Diamanti, R. V. Roussev, Y. Yamamoto, and M. M. Fejer, "Highly efficient single-photon detection at communication wavelengths by use of upconversion in reverse-proton-exchanged periodically poled LiNbO3 waveguides," *Opt. Lett*. **30**(13), 1725-1727 (2005).

[15] H. Kamada, M. Asobe, T. Honjo, H. Takesue, Y. Tokura, Y. Nishida, O. Tadanaga, and H. Miyazawa, "Efficient and low-noise single-photon detection in 1550nm communication band by frequency upconversion in periodically poled LiNbO3 waveguides," *Opt. Lett*, **33**(7), 639-641 (2008).

[16] L. Ma, O. Slattery, and X. Tang, "Experimental study of high sensitivity infrared spectrometer with waveguide-based up-conversion detector," *Opt. Express,* **17**(16), 14395-14404 (2009).

[17] J. Huang and P. Kumar, "Observation of quantum frequency conversion," *Phys. Rev. Lett.*, **68**(14), 2153-2156, (1992).

[18] E. Diamanti, H. Takesue, T. Honjo, K. Inoue, and Y. Yamamoto, "Performance of various quantum-key-distribution systems using 1.55-μm up-conversion single-photon detectors," *Phys. Rev. A.* **72**, 052311 (2005).

[19] J. S. Pelc, Q. Zhang, C. R. Phillips, L. Yu, Y. Yamamoto and M. M. Fejer, "Cascaded frequency upconversion for high-speed single-photon detection at 1550nm," *Opt. Lett*. **37**(4), 476-478 (2012).

[20] J. S. Pelc, L. Ma, C. R. Phillips, Q. Zhang, C. Langrock, O. Slattery, X. Tang and M. M. Fejer, "Long-wavelength-pumped upconversion single-photon detector at 1550nm: performance and noise analysis," *Opt. Express*, **19**(22), 21445-21456, (2011).

[21] P. S. Kuo, J. S. Pelc, O. Slattery, Y. Kim, M. M. Fejer and X. Tang, "Reducing noise in single-photon-level frequency conversion," *Opt. Lett*. **38**(8), 1310-1312 (2013).

[22] G. Shentu, J. S. Pelc, X. Wang, Q. Sun, M. Zheng, M. M. Fejer, Q. Zhang, and J. Pan, "Ultralow noise up-conversion detector and spectrometer for the telecom band," *Opt. Express*, **21**(12), 13986 (2013)

[23] R. S. Weis and T. K. Gaylord, "Lithium niobate: Summary of property and Crystal Structure", *Appl. Phys. A*, **37**, 191 (1985)

[24] http://en.wikipedia.org/wiki/Lithium_niobate

[25] http://www.hcphotonics.com/products2.asp?area=1670&cat=1750&sn=910

[26] Van Devender and Aaron Pace, Ph. D. Dissertation, (2007)

[27] J. E. Midwinter and J. Warner, "The effects of phase matching and of uniaxial crystal symmetry on the polar distribution of second-order non-linear optical polarization", *Brit. J. Appl. Phys*, **16**, 1135 (1965)

[28] H.Y. Shen, H. Xu, Z.D.Zeng, W.X.Lin, R.F.Wu, and G.F.Xu, *Appl. Opt*, **31**, 6695(1992)

[29] YAO Jian-Quan, YU Yi-Zhong, WANG Peng, WANG Tao, ZHANG Bai-Gang, DING Xin, CHEN Jin, H.J. Peng, H. S. Kwok, *Chin. Phys. Lett*, **18**, 1214(2001)

[30] David E. Zelmon, David L. Small, and Dieter Jundt, *J. Opt. Soc. Am. B*, **14**, 3319(1997)

[31] O. Paul, A. Quosig, T. Bauer, M. Nittmann, J. Bartschke, G. Anstett and J.A. L'Huillier, *Appl. Phys. B*, **86**, 111(2007)

[32] Dieter H. Jundt, *Opt. Lett*, **22**, 1553(1997)

[33] D. Li, Y. Jiang, Y. J. Ding, I. B. Zotova and N. S. Prasad, "Approaching single-photon detection in near-infrared region," *Appl. Phys. Lett*. **101**, 141126 (2012).

[34] D. Li, G. Sun, Y. Ding, and N. Prasad, "Long-wavelength-pumped single-photon detector based on frequency up-conversion in MgO-doped periodically-poled LiNbO3 waveguide reaching ultralow dark count rates", CLEO 2013, CM4D

[35] M. M. Fejer, G.A. Magel, D. H. Jundt and R. L. Byer, *IEEE J. Quantum Electron*, **28**, 2631 (1992)

[36] J. S. Pelc, "Frequency conversion of single photons: physics, devices, and applications", Ph.D. dissertation

[37] R. L. Byer and S. E. Harris, "Power and bandwidth spontaneous parametric emission," *Phys. Rev.* **168**(3), 1064-1068 (1968).

[38] T. G. Giallorenzi and C. L. Tang, "Quantum theory of spontaneous parametric scattering of intense light," *Phys. Rev.*, **166**(2), 225-233 (1968).

[39] J. E. Pearson, U. Ganiel, and A. Yariv, "Observation of parametric fluorescence and oscillation in the infrared," *Appl. Opt.* **12**(6), 1165-1171 (1973).

[40] A. Yariv, *Quamtum Electronics*, 3rd edition, John Wiley & Sons, Inc. p. 387.

[41] Y. Jiang, D. Li, Y. J. Ding, and I. B. Zotova, Opt. Lett. **36**, 1608 (2011).

[42] Minoru Taya, Matthew C. Bashaw, and M. M. Fejer, *Opt. Lett.* **21**, p. 857 (1996).

[43] K. Rivoire, Z. Lin, F. Hatami, and J. Vučković, *Appl. Phys. Lett*, **97**, 043103 (2010).

[44] H. Komine, W. H. Long, Jr. J. W. Tully, and E. A. Stappaerts, *Opt. Lett*, **23**, 661 (1998).

[45] M. Raybaut, A. Godard, A. Toulouse, C. Lubin, and E. Rosencher, *Opt. Express*, **16**, 18457 (2008).

[46] W. Shi and Y. J. Ding, Opt. Commun. **207**, 273 (2002).

[47] M. Müller, E. Soergel, K. Buse, C. Langrock, and M. M. Fejer, *J. Appl. Phys*, **97**, 044102 (2005).

[48] K. Pandiyan, Y. S. Kang, H. H. Lim, B. J. Kim, and M. Cha, *Opt. Express*, **17**, 17862 (2009).

[49] P. P. Dwivedi, H. J. Choi, B. J. Kim, and M. Cha, *Opt. Express*, **21**, 30221 (2013).

[50] Y. J. Ding, S. J. Lee, and J. B. Khurgin, *Phys. Rev. Lett.* **75**, 429 (1995).

[51] http://en.wikipedia.org/wiki/Faddeeva_function

[52] K. T. Tsen, D. K. Ferry, A. Botchkarev, B. Sverdlov, A. Salvador, and H. Morkoç *Appl. Phys. Lett*. **71**, 1852-1854 (1997).

[53] Y. J. Ding and J. B. Khurgin, Laser *Photon. Rev*. **6**, 660-677 (2012).

[54] Y. Repelin, E. Husson, F. Bennani, and C. Proust, *J. Phys. Chem. Solids*, **60**, 819-825 (1999).

[55] R. F. Schuaufele and M. J. Weber, *Phys. Rev*. **152**, 705-708 (1966).

[56] http://www.doitpoms.ac.uk/tlplib/raman/raman_scattering.php

[57] P. Hermet, M. Veithen, and Ph. Ghosez, *J. Phy. Condens. Matter*, **19**, 456202 (2007).

[58] S. Koutva-Arguirova, Tz. Arguirov, D. Wolfframm and J. Reif, "Influence of local heating on micro-Raman spectroscopy of silicon," *J. Appl. Phys*. **94**, 4946/1-4 (2003).

[59] R. F. Schuaufele and M. J. Weber, "Raman scattering by lithium niobate," *Phys. Rev*. **152**, 705-708 (1966).

[60] T. C. Damen, S. P. S. Porto, and B. Tell, "Raman effect in zinc oxide," Phys. Rev. **142**, 570-574 (1966).

[61] P. Zhao, "Compact Terahertz sources based on Difference Frequency Generation", graduation dissertation, http://preserve.lehigh.edu/cgi/viewcontent.cgi?article=2148&context=etd

[62] S. Kumar, “Recent Progress in Terahertz Quantum Cascade Lasers”, IEEE J. Sel. Top. Quantum Electron. **17**, 38 (2011).

[63] L. Xu, X.-C. Zhang, and D. H. Auston, Appl. Phys. Lett. **61**, 1784 (1992).

[64] D. H. Auston, K. P. Cheung, and P. R. Smith, Appl. Phys. Lett. **45**, 284 (1984).

[65] D. H. Auston, K. P. Cheung, J. A. Valdmanis, and D. A. Kleinman, Phys. Rev. Lett. **53**, 1555 (1984).

[66] Y. J. Ding and W. Shi, “Efficient THz generation and frequency upconversion in GaP crystals,” Sol. State Electron. **50**, 1128-1136 (2006).

[67] Y. Jiang, Y. J. Ding and I. B. Zotova, “Efficient frequency upconversion of coherent radiation from 10.26 μm to 1.187 μm in a GaSe crystal,” Opt. Commun. **282**, 4136-4140 (2009).

Journal and Conference Publications list

Journal Papers:

1. ***Da Li***, Yi Jiang, Yujie J. Ding, Ioulia B. Zotova, and Narasimha S. Prasad, "Approaching single-photon detection in near-infrared region", Appl. Phys. Lett. 101, 141126 (2012)

2. Yi Jiang, ***Da Li***, Yujie J. Ding, and Ioulia. B. Zotova, "Terahertz generation based on parametric conversion: from saturation of conversion efficiency to back conversion", Optics Letters, Vol.36, No.9, May (2011)

3. Yujie J. Ding, Pu Zhao, Srinivasa Ragam, ***Da Li***, and Ioulia B. Zotova, "Recent progress on terahertz generation based on difference frequency generation: from power scaling to compact and portable sources", Chinese Optics Letters, Vol. 9, Issue 11, pp. 110004- (2011)

4. Yujie Ding, Pu Zhao, Srinivasa Ragam, ***Da Li*** and Ioulia. B. Zotova, "Review on parametric generation of Terahertz wave: From maximum conversion efficiency to new route to compact and portable sources", *J. Nonlinear Optic. Phys. Mat.* **20**, 249 (2011)

Conference Papers:

1. ***Da Li***; Ran Wang; Zhaojun Liu; Lei Wang; Yujie J. Ding, "Surface-Emitting Second-Harmonic Generation: Effective Technique for Evaluating Periodically-Poled Lithium Niobate Waveguide Domains with Nanoscale Resolution", JTu4A.111, CLEO 2014

2. ***Da Li***; Pengda Hong; Zhaojun Liu; Yujie J. Ding; Lei Wang, "Enhanced Forward and Backward Anti-Stokes Raman Signals in Lithium Niobate Waveguides", JW2A.103, CLEO 2014

3. ***Da Li***; Xingquan Zou; Yujie J. Ding, "Approaching Single-Photon Detection Level in Communication Band via Frequency Upconversion in GaP", FTh3D.4, CLEO 2014

4. Xinquan Zou; Pengda Hong; ***Da Li***; Yujie J. Ding, "Power Enhancement, Noise Reduction, and Linewidth Narrowing of THz Output by Mixing Beams from Coupled Oscillators", JTh2A.105, CLEO 2014

5. Guan Sun; ***Da Li***; Roulin Chen; Yujie J. Ding; "Generation of Coherent Ultraviolet Radiation by Efficient Frequency Conversion Based on Nitride Heterostructures", JTh2A. 104, CLEO2014

6. ***Da Li***, Guan Sun and Yujie Ding, "Long-wavelength-pumped single-photon detector based on frequency up-conversion in MgO-doped periodically-poled $LiNbO_3$ waveguide reaching ultralow dark count rates", CM4D, CLEO 2013

7. ***Da Li***, Zhaojun Liu, Pengda Hong, Yujie J. Ding, Lei Wang, Ping-Ran Hua and De-Long Zhang, "Enhancement of backward propagating Anti-Stokes Raman Scattering from Ti-diffused lithium niobate waveguides", QF1D, CLEO 2013

8. Yujie J. Ding; Pu Zhao; ***Da Li***; "Recent Progress on Compact and Portable Terahertz Source Based on Parametric Conversion from Dual-Frequency Solid-State Laser Pulses", Journal of Physics: Conference Series 414 (1), 012003

9. ***Da Li*** and Yujie J. Ding, "Efficient conversion between counter-propagating fundamental and high-order modes in optical fiber with tilted gratings being incorporated for applications in nonlinear optics", IPC 2012

10. ***Da Li***, Yujie J. Ding, Ioulia B. Zotova, and Narasimha S. Prasad, "Single-photon detector based on frequency up-conversion in MgO-doped periodically-poled LiNbO3 waveguide: record-low dark counts and detectable photons", JTh3K, CLEO 2012

11. Yujie J. Ding; Pu Zhao; ***Da Li***; "Compact and portable terahertz source based on frequency mixing using dual-frequency solid-state laser", SPIE OPTO, 82600K-82600K-15

12. ***Da Li***, Yi Jiang and Yujie J. Ding, "Investigation of Slow, Stop and Fast Light Based on Polariton Resonances in Boron Nitride", JThB53, CLEO 2011

13. ***Da Li***, Yi Jiang, Yujie J. Ding, Boon S. Ooi, Ioulia B. Zotova and Narasimha S. Prasad, "Single-photon detection in Near-Infrared Region Based on Frequency Upconversion in MgO-Doped Periodically Poled Lithium Niobate Waveguide", CMC3, CLEO 2011

14. Yi Jiang, ***Da Li***, Yujie J. Ding and Ioulia B. Zotova, "Broadband Phase-Matched Backward Difference-Frequency Generation: A Novel Scheme for Spectral Optical Phase Conjugation", JThB92, CLEO 2011

15. Yi Jiang, ***Da Li***, Xiaomu Lin, Yujie J. Ding, Ioulia B. Zotova, Lei Wang and Narasimha S. Prasad, "Enhancement on Surface-Emitting Second-Harmonic Generation by Counter-Propagating Fundamental Beams in $LiNbO_3$ Channel Waveguide by Seven Orders of Magnitude", CMC6, CLEO 2011

16. Yi Jiang, ***Da Li***, Yujie J. Ding and Ioulia B. Zotova, "Reaching Maximum Conversion Efficiency for Terahertz Generation in Reversely Stacked GaP Plates", CMW1, CLEO 2011

Vita

Da Li is a Ph.D. student under the supervision of Prof. Yujie Ding. He is an active member of Optical Society of America. His research interests include novel applications by exploiting second-order nonlinear media, especially single photon detection, THz generation, image correction, and probing of nanostructures. During the last several years, Mr. Li has investigated single photon detection in lithium-niobate waveguide within the communication band. As a result, he has achieved the world-record results. Single photon detection in the communication band has variety of applications such as quantum information and computing and sensing of CO_2. InGaAs/InP-based detectors suffer from several drawbacks such as high dark count rates and low detection efficiencies, preventing them from reaching single-photon levels. In comparison, frequency upconversion devices are capable of reaching ultralow dark counts and high detection efficiencies, and therefore, making the single-photon detection a reality. In his research, Mr. Li has designed a waveguide consisting of periodically-poled lithium niobate as a second-order nonlinear medium. Using such a waveguide as a frequency-upconversion detector, Mr. Li has reached the single-photon detection level within the communication band. Due to his unique design, Mr. Li has completely eliminated the noise photon counts

induced by the pump beam by taking advantage of a free-space coupler for collecting the photons. In his most recent work, for the first time, to the best of his knowledge, Mr. Li has established a theoretical model based on a clear concept for noise generation processes to support his experimental findings.

In addition to single photon detection, Mr. Li has made contributions to the research projects such as generation of THz waves in reversely-stacked Gallium Phosphide (GaP) wafers. These THz waves have applications in chemical sensing and detection of biological and chemical agents. He has also developed a nondestructive technique to probe the periodically-poled ferroelectric structures by studying far-field pattern based on sum-frequency generation from two counter-propagating beams. Mr. Li has demonstrated that such a technique is capable of reaching the nanoscale resolution.

Mr. Li has published articles in some of the top journals in his area, such as Applied Physics Letters and Optics Letters. He has presented his key findings in Conference on Laser and Electro-Optics (CLEO) annually since 2010. He is an active reviewer for Optics Express and IEEE JSTQE.

Mr. Li earned his B.S. degree in Materials Science from Fudan University, Shanghai, China, where he was awarded People's Scholarship and Exxon Mobil Scholarship for his excellent academic performances. He has devoted himself to conduct scientific research when pursuing his Ph.D. degree at Lehigh University. He is the recipient of Packard Fellowship and RCEAS Emeritus Fellowship in 2012 and 2009, respectively.